Computational Study of Lattice Models

By

ALEKSANDER ZUJEV

DISSERTATION

Submitted in partial satisfaction of the requirements for the degree of

DOCTOR OF PHILOSOPHY

in

PHYSICS

in the

OFFICE OF GRADUATE STUDIES

of the

UNIVERSITY OF CALIFORNIA

DAVIS

Approved:

_____

_____

_____

Committee in Charge

2010

For my high school Mathematics teacher Vera Nikitichna
and Physics teacher Pyotr Vasilievich.

Abstract

This dissertation is composed of the descriptions of a few projects undertook to complete my doctorate at the University of California, Davis. Different as they are, the common feature of them is that they all deal with simulations of lattice models, and physics which results from interparticle interactions. As an example, both the Feynman-Kikuchi model (Chapter 3) and Bose-Fermi mixture (Chapter 4) deal with the conditions under which superfluid transitions occur.

The dissertation is divided into two parts. Part I (Chapters 1-2) is theoretical. It describes the systems we study - superfluidity and particularly superfluid helium, and optical lattices. The numerical methods of working with them are described. The use of Monte Carlo methods is another unifying theme of the different projects in this thesis.

Part II (Chapters 3-6) deals with applications. It consists of 4 chapters describing different projects. Two of them, Feynman-Kikuchi model, and Bose-Fermi mixture are finished and published. The work done on $t - J$ model, described in Chapter 5, is more preliminary, and the project is far from complete. A preliminary report on it was given on 2009 APS March meeting. The Isentropic project, described in the last chapter, is finished. A report on it was given on 2010 APS March meeting, and a paper is in preparation.

The quantum simulation program used for Bose-Fermi mixture project was written by our collaborators Valery Rousseau and Peter Denteneer. I had written my own code for the other projects.

Acknowledgments

First I thank my advisor, Professor Richard T. Scalettar, for his help, for doing much of the job for me, for being patient with me, and being generally better to me than I deserved.

Thanks to the other members of the Committee. Professor Zieve helped me to better understand the behavior of superfluids. Professor Singh suggested a plan for improving my oral and communications skills, which I'm trying to follow.

I thank Dr. Simone Chiesa for his help, especially when I was stuck in the isentropic project, and he found the solution.

I thank my collaborators in Bose-Fermi mixture project - Andrew Baldwin, Valy G. Rousseau, Peter J. Denteneer, and Marcos Rigol.

Particular thanks to Professor Warren E. Pickett. He reintroduced me to Physics after a long break, when I attended his class on QM in 2002-2003 while preparing to enroll in graduate school. Throughout my years at the UC Davis, he was always helpful and encouraging.

Thanks to my schoolteacher friend Delaine, who encouraged me to go back to school, and helping me through difficult times - when I was down with a cold, when I was hit by a truck, and at many other times.

For absent friends: Thanks to Naum Phleger, who was Professor Pickett's TA when I was taking his class in QM, and who was encouraging my efforts greatly.

And thanks to everybody I forgot to mention.

Contents

List of Figures

.

Introduction

This dissertation consists of two parts, part I being the theory, and part II discusses applications. First in chapter 1 are described the systems which we study, and models used: superfluidity, trapped quantum gases, and the tight-binded Hamiltonians which are used to determine their properties. Chapter 2 describes numerical techniques we use: classical Monte Carlo, quantum Monte Carlo, and mean field theory.

Part II describes applications of the methods. Chapter 3 discusses the Feynman-Kikuchi model, chapter 4 concerns Bose-Fermi mixtures, chapter 5 is an application to the t-J model, and, finally, chapter 6 addresses the Hubbard model in mean field theory.

Part I

Theory

Chapter 1

Studied Systems and Models

1.1 Superfluidity

1.1.1 Experiments

Superfluidity [1, 2, 3] is a phase of matter characterized by the complete lack of viscosity. A superfluid, placed in a closed loop, can flow endlessly without friction. The transition point from normal liquid to superfluid is called the λ-point. Liquid ^4He undergoes a transition to superfluid at 2.17 K. At this point, ^4He shows dramatic changes not only in its viscosity, but also its specific heat and thermal conductivity.

Figure 1.1 (left) shows the phase diagram of liquid Helium as a function of temperature and pressure. At atmospheric pressure, Helium is a liquid all the way down to T=0. The lack of solidification is a consequence of large quantum fluctuations (low mass) and the closed shell atomic structure of noble gases which minimizes their interactions. Helium does, however, undergo a transition to a superfluid state as T is lowered.

The specific heat of ^4He (Fig. 1.1 right) undergoes an anomaly close to T_λ. In fact, the shape of the specific heat plot led to the name λ transition. The empirical formula for the specific heat, according to Buckingham and Fairbank [4] is,

$$c_v = 4.55 - 3.00 \log_{10} |T - T_\lambda| - 5.20\Delta \quad (J/(g \cdot K)) \tag{1.1}$$

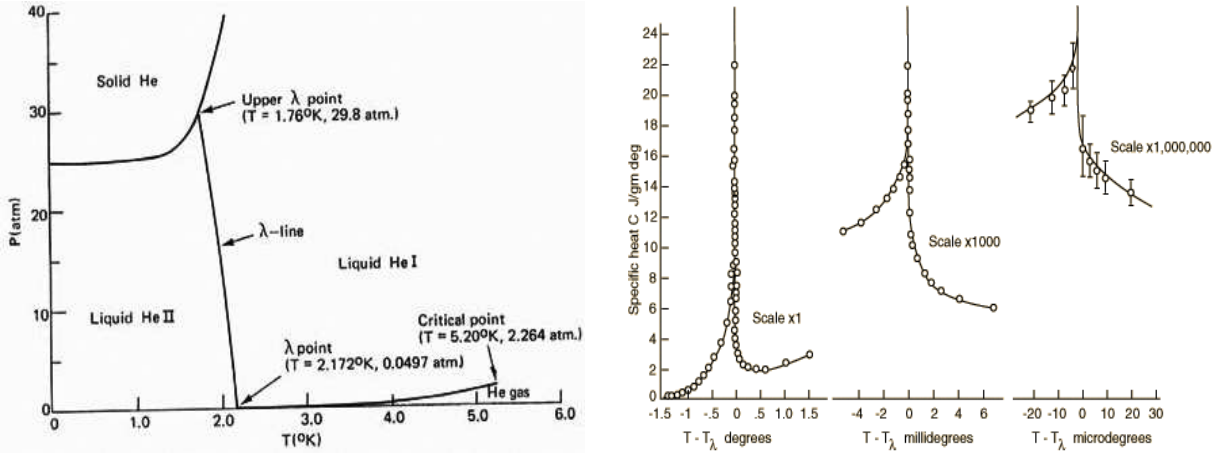

Figure 1.1: Left: Phase diagram of ^4He.
Right: Specific heat of ^4He, by Buckingham and Fairbank [4].

$(\Delta = 0, \;\; T < T_\lambda; \quad \Delta = 1, \;\; T > T_\lambda)$

Superfluid helium doesn't boil in a normal way. This behaviour suggests infinite heat conductivity. Suppose we reduce the pressure of ^4He, so that it is boiling. Above T_λ, it is normal boiling, with formation of bubbles of vapour in the bulk of liquid. Below T_λ, no bubbles are formed. The liquid is still. The explanation is that evaporation is still going on, but it occurs only on the surface. Heat transfer is very easy, due to superfluidity, between the surface and the bulk of liquid, so there are no local inhomogeneities and bubbles in the bulk. Thus the abnormal nature of boiling suggests infinite heat conductivity.

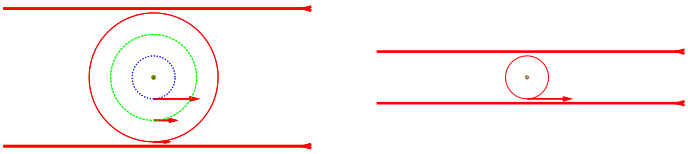

Figure 1.2: Vortex in a channel. Arrows: velocity of superfluid around a vortex: $v_s = \frac{\hbar}{mr}$,
r = distance from the axis of a vortex.
In a wide channel the wall is far from the vortex axis, and hence v_s is small. In a narrow channel, the wall is close to the vortex axis and v_s is large. Since $v_{cr} \simeq v_s$ at the wall, $v_{cr} \simeq \frac{\hbar}{md}$ where d is the diameter.

The flow of superfluid helium is easier through a pipe of smaller diameter than one of larger diameter (Fig. 1.2 left). At first glance it may seem counterintuitive that the

critical velocity (velocity above which the flow is not frictionless anymore) is increasing with decreasing of the diameter d of the pipe: $v_{cr} \simeq \frac{\hbar}{md}$. This results from the creation of quantum vortices. The derivation of the movement of the liquid in a quantum vortex is similar to the semiclassical derivation of the movement of an electron in hydrogen atom. If the momentum of a helium atom in its movement around the axis of the vortex is $p = mv$, and the circumference of its path around the vortex is $2\pi r$, where r is the distance from the axis of a vortex, where m is mass of ^4He atom, v is the velocity of superfluid around a vortex, then we must have a quantization $p(2\pi r) = nh$, or $v = \frac{n\hbar}{mr}$. The vortices form at the wall of the tube, and their velocity at the opposite wall must be $v = \frac{\hbar}{md}$ (using minimal $n = 1$). It means that vortices can only form when the velocity of the flow in the tube must be $v \geq \frac{n\hbar}{mr}$. Once the vortices begin to form, they can exchange energy with the superflow, effectively ending it. [5, 6]

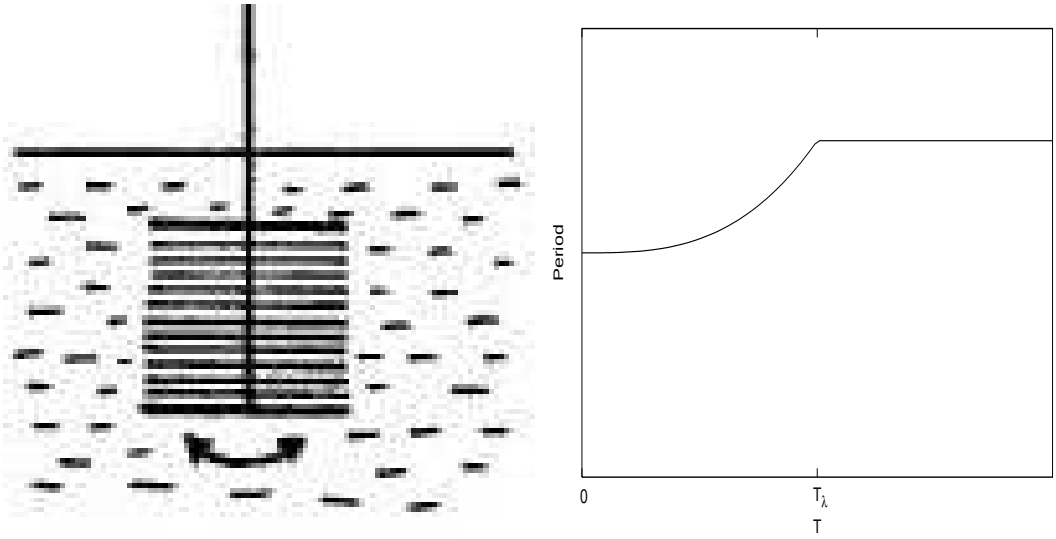

Figure 1.3: A torsional oscillator consists of a set of a closely spaced disks immersed in liquid helium and supported by a thin wire (left). A qualitative plot of dependence of the period of torsional oscillator in liquid helium on temperature (right).

Torsional oscillator experiments provide one of the most simple illustrations of the lack of viscosity in a superfluid. A torsional oscillator (Fig. 1.3 left) consists of closely spaced disks, immersed in liquid. For small angles, the torque is $\tau = \kappa\theta$, and the period of

the torsional oscillator is $T = 2\pi\sqrt{\frac{I}{\kappa}}$ where I is its moment of inertia. This is true in the absence of friction. Due to friction, in a liquid the period of torsional oscillator is increased compared to a free oscillator. If the spacing between the disks is sufficiently small, we can approximately assume that the fluid between the disks makes a single rigid body, together with the disks. Knowing the geometry of the space between disks, and density of the fluid, we can determine the combined moment of inertia of the oscillator, and its period. In liquid helium the oscillator behaves strangely: below T_λ its period starts to decrease, and reaches a minimum at $T = 0$ (Fig 1.3 right). The period drops because the SF no longer couples to the disks, and the moment of inertia is reduced. The fact that the period drops not at once as a step-function, but gradually, suggests that the part of He which is superfluid is a continuous function of temperature. Andronikashvili [7] determined the superfluid fraction of He. If we know the period of an oscillator, we can determine the density of the fluid. Andronikashvili got an empirical formula for the superfluid part

$$\frac{\rho_s}{\rho} \;=\; 1 - \left(\frac{T}{T_\lambda}\right)^{5.6} \tag{1.2}$$

1.1.2 Superfluid and Bose-Einstein condensate

Superfluidity is closely related to Bose-Einstein condensate, but not identical to it. If we have a 3-D gas of non-interacting bosons, and we cool it down, then it will undergo a phase transition to a state in which a macroscopic fraction of particles occupies the ground state energy level. The critical temperature is

$$T_c = \frac{2\pi\hbar^2}{m k_B}\left(\frac{n}{\zeta(3/2)}\right)^{2/3}. \tag{1.3}$$

If we substitute into this formula data for helium: $m = 4$ amu, $n = 145\ \mathrm{kg/m^3}/(4\ \mathrm{amu})$, then we get $T_c = 3.15K$, which is pretty close to the $T_\lambda = 2.17K$. However, a superfluid is not simply a Bose-Einstein condensate: while a superfluid has much in common with a BEC, there are some differences. Later in this thesis we will make very precise definitions

of BEC and superfluidity, and describe how the fraction of condensate n_0 and ρ_s are measured in simulations. For now, we simply note that, in words, n_0 is given by the $r \to \infty$ value of the amplitude for inserting a particle in the system at the origin and removing it a distance r away, or, equivalently, the number of particles in the $k = 0$ state. In a BEC, the fraction of condensate is $n_0 = 1 - \left(\frac{T}{T_c}\right)^{3/2}$. At zero temperature n_0=1: all particles of the condensate are in ground state. In contrast, ρ_s is given by the response of the system to a twist in the boundary conditions. In a superfluid helium, only about 10% of particles go into ground state at zero temperature. Superfluid consists not only of ground-state particles. At zero temperature, all He is superfluid, though only part of it is in the ground-state. Such dramatic difference is due to the fact that in contrast to BEC, consisting of noninteracting particles, superfluid consists of strongly interacting particles[3].

This difference is emphasized by the fact that there is no BEC in 2D, but there is superfluidity. It can be shown that for BEC in 2D the transition point, the temperature below which a macroscopic part of particles is in the ground state is $T_c = 0$, i.e. there is no finite T BEC in 2D. Even though there is no BEC in 2D, superfluidity in 2D is possible, and indeed there are numerous experimental and theoretical papers on superfluid transitions in thin (2D) films[8, 9, 10].

1.1.3 Path Integral Picture and Exchange

Here we illustrate the path integral approach to superfluidity. We focus on this picture because of its connections to the numerical methods used in this thesis. Feynman considered the problem of how to compute the probability amplitude $\langle x_a|e^{-iH(t_b-t_a)/\hbar}|x_b\rangle$ for a quantum particle to go from point x_a at time t_a to point x_b at time t_b. He showed that this amplitude can be written as an integral over all possible paths $x(t)$ from x_a to x_b, where the integrand is $e^{iS_{cl}/\hbar}$ and S_{cl} is the classical action. This is illustrated in Figure 1.4. The classical path is an extremum of the action and hence paths around it contribute most to the sum, because the phase oscillations do not cause cancellations.

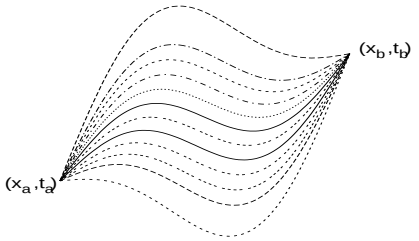

Figure 1.4: According to Feynman, the quantum probability amplitude can be computed by summing up the exponentials of the classical action over all possible paths between the initial and final points.

It turns out that this path integral way of thinking gives us a beautiful way to visualize superfluidity, especially in numerical simulations. First, we recognize that Feynman's path integral construction applies equally well to the quantity $e^{-\beta H}$ central to statistical mechanics. We merely replace $t = \beta/i$. Then the partition function for a single quantum particle $Z = Tre^{-\beta H}$ can be written as a sum of all the possible paths the particle can take in going from position x_a at "imaginary time" $\tau = 0$ to position x_b at "imaginary time" $\tau = \beta$.

If the temperature T is large, then $\beta = 1/T$ is small, and the quantum particle is unlikely to move very far: The action for moving a large distance in a small time is very big, and the associated weight $e^{-\beta S}$ is small. (Indeed it can be shown that the typical distance of propagation is just the de Broglie thermal wavelength $\lambda = \frac{h}{\sqrt{2\pi mkT}}$.) As T is lowered and β increases, however, the quantum particle can wander over larger distances. This difference is shown in Fig. 1.5.

Now consider a collection of (indistinguishable) quantum particles. They start out at some locations at $\tau = 0$ and propagate around. As T is lowered their wandering ultimately brings them into contact with each other. They undergo 'exchange'. It turns out that when the exchange becomes large, this signals the superfluid phase transition.

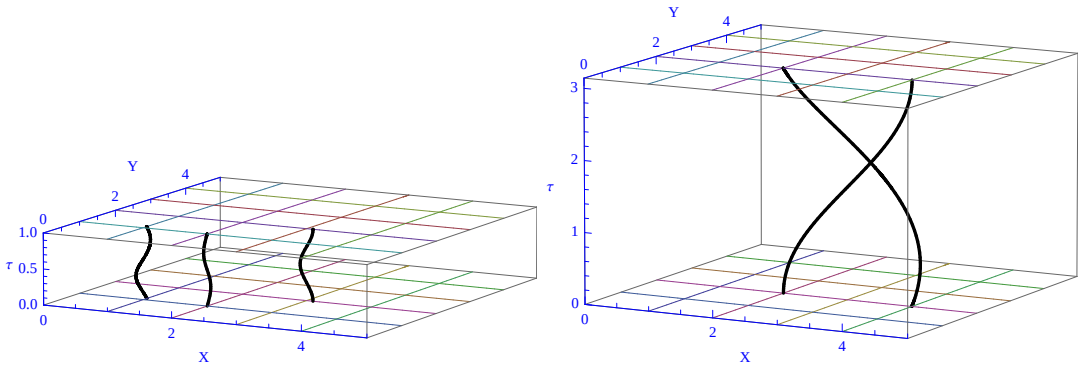

Figure 1.5: Left: For small β (high T), the particles stay in place; the paths of particles are essentially vertical lines. There is not enough (imaginary) time for a particle to satisfy the trace condition by having its final location at $\tau = \beta$ equal the starting point at $\tau = 0$ of another particle. Right: For large β (low T): particles may exchange. The paths can be winding lines.

This point is worth emphasizing, since it is the central physical picture adopted in numerical work on superfluidity: Superfluidity occurs when the Feynman paths of identical quantum particles become large enough that they touch each other and conglomerate into a single tangled mess: because the particles cannot be distinguished, when the paths meet, you cannot say which path belongs to which particle. The superfluid transition occurs when this process of larger exchange paths reaches the point where a single exchange path crosses the entire sample. Because the path encompasses the whole system, a twist to the boundaries has large effects, motivating our earlier comment that ρ_s is linked to the response to changes in the boundary conditions.

1.1.4 Feynman-Kikuchi model

Chapter 3 of this thesis is built upon a paper we wrote to understand the superfluid transition and its generalization. Here we discuss the special model studied in that work.

Using his path integral approach, Feynman[11] arrived at an expression for the partition function for the superfluid phase transition:

$$Z = \frac{K_\beta}{N!}\left(\frac{m'}{2\pi\beta\hbar^2}\right)^{3N/2}\int\sum_P \exp\left\{-\frac{m'}{2\beta\hbar^2}\sum_i (x_i - Px_i)^2\right\}\rho(x_1,...x_N)d^N x_i \qquad (1.4)$$

where m' is the effective mass, Px_i denotes permutations of the initial coordinates x_i. $\rho(x_1, ...x_N)$ is the density (weight) of a configuration: if atoms in the configuration overlap, then $\rho(x_1, ...x_N)$ is close to 0, and finite otherwise. We will ignore the factor K_β here. For details, see Feynman[11].

One might be surprised by the appearance of β in denominator of the exponential, since in statistical mechanics one usually has $e^{-\beta E}$. However, further thought shows that this might make sense: as β increases (i.e. T decreases), movement from site to site becomes easier, and easy movement means superfluidity. This qualitative calculation is of course, validated by the actual derivation of Eq. 1.4. The expression is further simplified if the atoms are allowed to occupy only particular lattice points:

$$Z = \sum_P \exp\left[-\frac{1}{2\beta}\sum_i (x_i - Px_i)^2\right] \tag{1.5}$$

(We set here $m' = \hbar = 1$ and omit the constant factor $\frac{K_\beta}{N!}\left(\frac{m'}{2\pi\beta\hbar^2}\right)^{3N/2}$.)

The path integral expression for $Z = \mathrm{Tr}[e^{-\beta H}]$ looks like for N particles moving in the continuum: The particles start out at imaginary time $\tau = 0$ at some set of locations $\{\vec{x}_n\}$ for $n = 1$ to N. They propagate to imaginary time $\tau = \beta$ and, because of the "Trace" in the definition of Z, their final spatial locations must be the exact same set $\{\vec{x}_n\}$. At high temperature T (small β) the only way this can happen is for each individual particle to end up where it started. At low T (large β) it is possible for the particles to exchange, so that, for example, particle 2 ends up where particle 1 started, etc.

The exact path integral representation of this problem is rather complex: it consists of the N continuous lines $\vec{x}_n(\tau)$ which describe how the N particles move from $\tau = 0$ to $\tau = \beta$. If, however, we think of whether or not the particles exchange as the crucial element of the problem, then we really might not care about the details of how the particles move. It might be a good approximation to focus only on their final locations and whether each one ended up in the same place as where it started or not. This suggested to Feynman and Kikuchi a much simplified way of modeling the superfluid transition.

To make the content of equation (1.5) clear, it is useful to work out an example. Consider a lattice $\mathbf{n}$ of sites (here the lattice is 4×4):

```
13  14  15  16
 9  10  11  12
 5   6   7   8
 1   2   3   4
```

and then a lattice $\mathbf{n}'$ consisting of a permutation of the same 16 integers:

```
13  11  15  16
 9  14  10  12
 5   6   3   8
 1   2   7   4
```

Comparing with the original lattice, this permuted arrangement is understood to mean the following: Since the numbers '1,2,5,6,8,9,12,13,15,16' occupy the same locations in $\mathbf{n}$ and $\mathbf{n}'$, these eleven particles propagated without exchanging, each ending up precisely where it started. On the other hand, particles 3 and 7 did a 'two-cycle' exchange in which particle 3 ended up where 7 started, and particle 7 ended up where 3 started. Finally, particles 10,11,14 were in a 'three-cycle'.

The final step is to assign a probability to a configuration $\mathbf{n}'$. Looking at the Equation 1.5 for Z, we see that in the continuum the probabilities fall like $e^{-d^2/(2\beta)}$ where d is the distance the particle has to travel in going from $\tau = 0$ to $\tau = \beta$. (Again, the strange appearance of β in the *denominator* comes from the mathematics in constructing the path integral, but has the simple physical interpretation of reflecting the fact the particles have more "imaginary time" to propagate the distance d as β increases.) This suggests we write

down

$$\begin{aligned} p(\mathbf{n}') &= Z^{-1} e^{-S/\beta} \\ Z &= \sum_{\mathbf{n}'} e^{-S/\beta} \\ S &= \frac{1}{2} \sum_{\mathbf{n}} |\mathbf{n}'(\mathbf{n}) - \mathbf{n}|^2 \end{aligned} \tag{1.6}$$

The geometry/dimensionality of our system enters in how precisely we define $\mathbf{n}$: whether it is a single integer (d=1) , a pair of integers (d=2) ..., and the distance function ||. In the example above eleven of the sixteen $\mathbf{n}$ in the sum have $\mathbf{n}'(\mathbf{n}) = \mathbf{n}$, so contribute zero to S. For the other five sites particles 3, 7, 10, 14 moved one site each, and particle 11 moved one site horizontally, and one site vertically, so they contribute correspondingly 1/2, 1/2, 1/2, 1/2, 1 to S. So $S = 3$ for this $\mathbf{n}'$.

Now I'll describe how we determine superfluidity, using this Feynman-Kikuchi approach. The onset of superfluidity means that the system starts to show a macroscopic amount of movement. To make a precise criterion, we define $w_x = \frac{1}{N} \sum_{\mathbf{n}} ((n'(\mathbf{n}))_x - \mathbf{n}_x)$ where n_x is the x coordinate of the site. w_y is defined similarly. The average $\langle w_x \rangle$ will be zero, due to symmetry: w_x will be sometimes positive, or negative, averaging to zero. But $\langle w_x^2 \rangle$ becomes nonzero at the onset of superfluidity. The use of square of winding $\langle w^2 \rangle = \langle w_x^2 \rangle + \langle w_y^2 \rangle$ to get superfluid density was introduced by Pollock and Ceperley[12]. Using path integral method, they derive formula for the periodic system of size L and dimension d

$$\frac{\rho_s}{\rho} = \frac{m}{\hbar^2} \frac{\langle w^2 \rangle L^{2-d}}{\rho d \beta}. \tag{1.7}$$

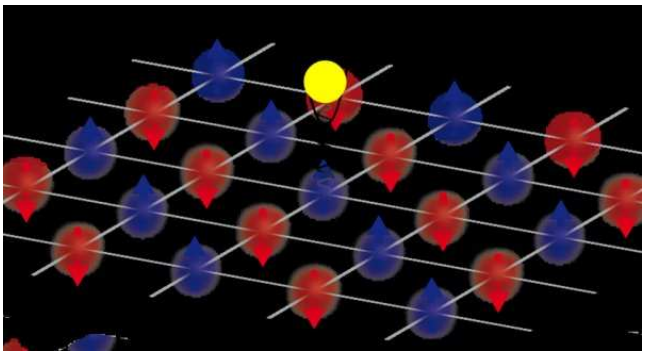

Figure 1.6: Schematic illustration of a two-dimensional optical lattice. The blue clouds and upwards pointing arrows represent atoms with moments in + direction. The red clouds and downwards pointing arrows represent atoms with moments in the − direction. The system is in antiferromagnetic state.

1.2 Atoms in Optical Lattice

Chapter 4 of this thesis is built upon a paper addressing the physics of a mixture of bosonic and fermionic atoms moving in an artificial lattice made from laser light and cooled to very low temperatures. Such an optical lattice[13, 14] (Figure 1.6) is created by a standing wave of laser beam. The electric field intensity in the standing wave is periodic in space. Placed in this field, an atom experiences a spatially periodic potential due to the ac Stark effect[13]. Depending on the laser frequency, an atom is attracted to the regions of maximum of the electric field, or to the regions of minimum of the electric field . As a result, an atom is pulled to anti-nodes or nodes of the standing wave. Using two or three pairs of counter-propagating laser beams, two-dimensional or three-dimensional optical lattices can be created. We'll consider a simple example of forming a one-dimensional lattice by two counter-propagating laser beams. We'll assume that the beams are propagating along the x axis, and that they are linearly polarized with E directed along the z axis. The electric field is

$$E = E_0 \cos(kx - \omega t) + E_0 \cos(-kx - \omega t) = 2E_0 \cos(kx) \cos(\omega t) \tag{1.8}$$

In the ac Stark effect, the potential is proportional to the time-averaged square of the electric field:

$$V \langle E^2 \rangle = \langle 4E_0^2 \cos^2(kx) \cos^2(\omega t) \rangle = 2E_0^2 \cos^2(kx) = E_0^2(\cos(2kx) + 1). \tag{1.9}$$

We can drop the constant, the potential is

$$V = V_0 \cos(2kx) = V_0 \cos\left(\frac{2\pi x}{(\lambda/2)}\right) \equiv V_0 \cos\left(\frac{2\pi x}{d}\right). \tag{1.10}$$

So the potential - and optical lattice - is periodic in space with period of half the laser wavelength.

The optical lattices are basically crystals, as matter crystals. The potential minima correspond to the nucleii in condensed matter, and trapped atoms to the electrons. This makes them very attractive to condensed matter physicists. By tuning lattice parameters, it is possible to make different states of matter - superfluid, Mott insulator, Bose-Einstein condensate. The main lattice parameters to tune are potential strength, and lattice periodicity. The potential strength is controlled by the laser beam intensity. To control the lattice periodicity is not that easy. Ideally it would be good to control laser wavelength, but lasers usually have a fixed wavelength. However, a simple way to control the lattice periodicity is to aim two beams not exactly counter-propagatory, but at an angle. This will increase the lattice periodicity.

1.3 Tight Binding Models

Tight-binding models provide a simplified description of the motion and interactions of electrons in a solid. First, we need to account for the fact that there is a regular array of nuclear positions in a solid, which for simplicity we consider to be fixed, i.e. we ignore lattice vibrations. This suggests that we begin with a lattice of atoms (sites) on which the electrons move. A single atom is already a very complex structure, with many different

energy levels. In the single band Hubbard Hamiltonian we make a big simplification by considering an "atom" with a single energy level. Then, the Pauli principle would tell us that at most two electrons (one with spin up and one with spin down) can sit on this 'atom'. To emphasize the simplification being made, henceforth we will refer to the "atoms" as "sites". Thus each site has a four dimensional Hilbert space, consisting of the states,

$$\langle\, 0 \,| \qquad \langle \downarrow | \qquad \langle \uparrow | \qquad \langle \uparrow\downarrow | \tag{1.11}$$

In a solid where electrons can move around, the electrons interact via a screened Coulomb interaction. The biggest interaction will be for two electrons on the same site. So the interactions are modeled by a term which is zero if the site is empty of electrons or has only a single electron on it, but has the value U if the site has two electrons. There is no interaction between electrons on different sites. The kinetic energy consists of an expression which allows electrons to move from one site to its neighbors. The energy scale t which governs this 'hopping' will be determined by the overlap of two wavefunctions on the pair of sites. Since wavefunctions die off exponentially, we can begin by allowing hopping only between the closest sites in our lattice.

1.3.1 Fermion Hubbard Hamiltonian

The Hubbard model [15, 16, 17, 18] was invented in 1963, but it is still interesting to study. The Hubbard model offers one of the most simple ways to get insight into how the interactions between electrons can give rise to insulating, magnetic, and perhaps even novel superconducting effects in a solid.

The Hubbard model is especially well suited for studying atomic gas in optical lattice - here the system is effectively tight-binding - no interaction, except on the same site, and hopping between sites. The optical lattices are in many ways better to study than solids: the parameters t, U can be tuned to any values within a wide range; they are cleaner - no

defects or phonons; and there really is single band, assuming the atoms are low enough in energy.

Now we put these words into a precise mathematical framework, using the language of second quantization. The Fermion Hubbard Hamiltonian is

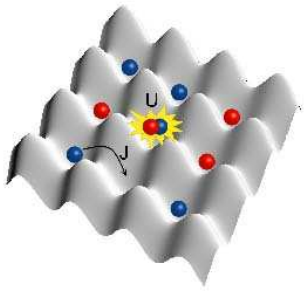

(J=t)

$$H = -t \sum_{\langle j,l\rangle\sigma} (c^{\dagger}_{j\sigma} c_{l\sigma} + c^{\dagger}_{l\sigma} c_{j\sigma}) + U \sum_{j} n_{j\uparrow} n_{j\downarrow} - \mu \sum_{j} (n_{j\uparrow} + n_{j\downarrow}). \qquad [19] \qquad (1.12)$$

The first term is the kinetic energy: It describes the destruction of an electron of spin σ on site l ($c_{l\sigma}$) and its creation on site j ($c^{\dagger}_{j\sigma}$) (or vice-versa). The symbol $\langle j, l\rangle$ emphasizes that hopping is allowed only between two sites which are adjacent. The second term is the interaction energy. It goes through all the sites and adds an energy U if it finds that the site is doubly occupied. The final term is a chemical potential which controls the filling. We refer to the situation where the filling is one electron per site as 'half-filling' since the lattice contains half as many electrons as the maximum number (two per site). Studies of the Hubbard model often focus on the half-filled case because it exhibits many interesting phenomena - Mott insulating behavior, anti-ferromagnetic order, etc. [18]

What is Mott insulating behavior and how does it arise? When U is very big, and the number of fermions equals the number of sites, the lowest energy state has every site with a single electron. The electrons cannot move since to do so would cause a double occupancy, and cost the very large energy U. It is plausible that as the hopping t increases, it might eventually win out over U, causing a transition into a metallic state. This is the "Mott transition", one of the central phenomena we will address in this thesis. Note that Mott behavior is inextricably linked to specific densities where the particle number ($\rho = 1$)

is commensurate with the number of lattice sites. If there is a vacancy ($\rho < 1$), fermions adjacent to the vacancy can move without an energy cost U. Likewise, a fermion on a pre-existing doubly occupied site ($\rho > 1$) can move without any additional energy cost.

The Hubbard Hamiltonian not only models metal-insulator transitions, but also spin ordering. The most simple qualitative way to understand how antiferromagnetism might arise in the half-filled Hubbard Hamiltonian is through second order perturbation theory in the hopping t. Consider two adjacent sites with parallel spin electrons, the state,

$$|\Psi_{\text{ferro}}\rangle = c^\dagger_{1\uparrow} c^\dagger_{2\uparrow} |\text{vac}\rangle = |\uparrow\ \uparrow\rangle \ . \tag{1.13}$$

The Pauli principle forbids any hopping from this state, i.e. when the kinetic energy operator acts on $|\Psi_{\text{ferro}}\rangle$ the result is zero,

$$-t(c^\dagger_{1\uparrow} c_{2\uparrow} + c^\dagger_{2\uparrow} c_{1\uparrow})|\Psi_{\text{ferro}}\rangle = 0 \ . \tag{1.14}$$

This means there can be no shift in the energy to any order in the hopping. Put another way, $|\Psi_{\text{ferro}}\rangle$ is an eigenstate of the (two site) Hubbard Hamiltonian and is not connected to any other state in the Hilbert space.

On the other hand, the "antiferromagnetic" state which has antiparallel spins,

$$|\Psi_{\text{antiferro}}\rangle = c^\dagger_{1\uparrow} c^\dagger_{2\downarrow} |\text{vac}\rangle = |\uparrow\ \downarrow\rangle \ , \tag{1.15}$$

is connected by the kinetic energy to states with double occupancy,

$$\langle \uparrow\downarrow \ \ 0 \ | - t(c^\dagger_{1\uparrow} c_{2\uparrow} + c^\dagger_{2\uparrow} c_{1\uparrow})|\Psi_{\text{antiferro}}\rangle = -t \ . \tag{1.16}$$

A second operation of the kinetic energy returns the doubly occupied state to $|\Psi_{\text{antiferro}}\rangle$, so that to second order in perturbation theory the energy of $|\Psi_{\text{antiferro}}\rangle$ is lowered by $J = 4t^2/U$. The energy denominator U is the energy of the intermediate doubly occupied

state. The factor of four comes from the two terms in the kinetic energy and the two possible choices for the intermediate doubly occupied state.

This very simple perturbation theory argument suggests that it is energetically favorable for neighboring sites to have antiparallel spins. That is, the ground state of the half-filled Hubbard model is likely to have antiferromagnetic correlations, at least locally.

The two site analysis can be made in a slightly different way which can be used to show that at very strong coupling and half-filling, the Hubbard Hamiltonian maps onto the spin-1/2 Heisenberg Hamiltonian,

$$H = J \sum_{\langle ij \rangle} \vec{S}_i \cdot \vec{S}_j \ . \tag{1.17}$$

Here $\vec{S}_i$ are the usual spin-1/2 operators, and $J = 4t^2/U$.

To see the connection between the Hubbard and Heisenberg Hamiltonians at half-filling, we write down the six occupation number states for two sites and two electrons:

$$\langle \uparrow \ \uparrow | \qquad \langle \downarrow \ \downarrow | \qquad \langle \uparrow\downarrow \ \ 0 | \qquad \langle 0 \ \ \uparrow\downarrow | \qquad \langle \uparrow \ \downarrow | \qquad \langle \downarrow \ \uparrow | \ . \tag{1.18}$$

As noted above the first two ferromagnetic states are eigenstates of the two site Hubbard Hamiltonian with energy 0. The next four states mix, but one can easily construct the 4x4 matrix for H and calculate the levels. The result is $0, U, \frac{1}{2}(U \pm \sqrt{U^2 + 16t^2})$. Expanding the square root, one gets the levels $0, U, U + 4t^2/U, -4t^2/U$. If we discard the two states with very high energy U, and consider also the two ferromagnetic states, we are left with four levels $0, 0, 0, -4t^2/U$. To within an energy shift, this is precisely the spectrum of the two site Heisenberg model, which consists of a triplet of degenerate states an energy J above a singlet state. This argument provides a quite formal basis for the connection between the Hubbard and Heisenberg models, and an alternate derivation of the relation $J = 4t^2/U$.

1.3.2 Bose-Fermi Mixtures

Experiments with ultracold atoms in optical lattices opened for physicists a new field with many new possibilities to investigate, to study - and engineer! - new kinds of matter. Bose-Fermi mixtures are one of these new possibilities. A mixture of bosons and fermions[20] in optical lattice is a new kind of matter, which leads to new interesting phenomena, and new and novel phases of matter.

The Bose-Fermi mixture Hamiltonian is constructed similarly to the Fermion Hubbard Hamiltonian. For 1-D it is:

$$\begin{aligned} \hat{H} = & - t_B \sum_l (b_{l+1}^\dagger b_l + b_l^\dagger b_{l+1}) \\ & - t_F \sum_l (f_{l+1}^\dagger f_l + f_l^\dagger f_{l+1}) \\ & + U_{BB} \sum_l \hat{n}_l^B (\hat{n}_l^B - 1) + U_{BF} \sum_l \hat{n}_l^B \hat{n}_l^F \end{aligned} \tag{1.19}$$

where $b_l^\dagger (b_l)$ are the boson creation (destruction) operators on site l of the one-dimensional lattice with L sites. Similarly, $f_l^\dagger (f_l)$ are the creation (destruction) operators on site l for spinless fermions on the same lattice. For these creation and destruction operators $\hat{n}_l^{B,F}$ are the associated number operators. The bosonic and fermionic hopping parameters are denoted by t_B and t_F respectively, and the on-site boson-boson and boson-fermion interactions by U_{BB} and U_{BF}.

The typical mixtures used in experiments are ^{87}Rb (boson), ^{40}K (fermion). Another possibility is ^{41}K (boson), ^{40}K (fermion). There are many other choices. Among experiments with Bose-Fermi mixtures are engineering and detecting superfluidity; tuning interactions by way of Feshbach resonance (more on this in chapter 4).

There are many new interesting developments in the area. For instance, Dutta and Lewenstein[21] examine two-dimensional Bose-Fermi mixture and predict unconventional superfluidity of fermions. The excitations in these superfluids are anyonic and obey non-Abelian statistics. Linder and Sudbø[22] investigate phase separation of Bose-Fermi mix-

ture and connect it to the critical superfluid velocity of the bosonic condensate.

1.3.3 t-J Hamiltonian

One might ask whether there is any strong coupling analog of the Heisenberg model, discussed in the previous subsection to which the fermion Hubbard model can be mapped in the 'doped' case when the density is less than half-filling. The answer is yes, and the Hamiltonian is known as the $t-J$ model [18],

$$\hat{H} = -t \sum_{\langle ij \rangle \sigma} (c^{\dagger}_{i\sigma} c_{j\sigma} + H.c.) + J \sum_{ij} \vec{S}_i \cdot \vec{S}_j \tag{1.20}$$

- and it is defined in the subspace with no doubly occupied sites.

We will not provide a formal derivation of the $t-J$ model from the Hubbard model here. The reader is referred to one of several discussions [23],[18]. However, it should be clear from the preceding section that the Heisenberg term naturally arises at strong coupling, and the kinetic energy term is present because away from half-filling there is still some motion of holes possible without double occupation occurring.

The $t-J$ model has a rich history, like the Hubbard model. It is easier to study the $t-J$ model by some numerical techniques like exact diagonalization and density matrix renormalization group, because the Hilbert space is smaller than Hubbard. But the lattice sizes which can be treated by diagonalization are very small, typically 10-20 sites. With such systems it is very difficult to assess finite size effects. One therefore turns to Monte Carlo methods to study larger lattices (up to 100-1000 sites). The Hubbard Hamiltonian has been extensively studied this way, in particular with the Determinant Quantum Monte Carlo (DQMC) method. Unfortunately, it is not known how to simulate the t-J model with DQMC. One of the projects described in this thesis (Chapter 5) is an attempt to develop a way to treat the $t-J$ model with the DQMC method.

1.4 Summary

After reviewing the systems and models studied in this thesis, we now will discuss the techniques used to solve them.

Chapter 2

Numerical Techniques

In this chapter we will review some of the most simple analytic approaches to quantum many body systems (weak and strong coupling analysis and mean field theory) as well as the basis of the numerical approaches (quantum monte carlo) we will be using in the remainder of this thesis.

2.1 Classical Monte Carlo

Monte Carlo methods are algorithms for solving computational problems by use of random numbers, in contrast to deterministic algorithms. Monte Carlo methods are widely used in computational physics, from quantum chromodynamics to cosmology. They are important in condensed matter physics, which deals with problems involving a large number of interacting particles, for which exact solutions are not possible, and analytic solutions use uncontrolled approximations.

2.1.1 History

Random methods were used in mathematics long before the 20th century. One of the interesting examples is Buffon's needle problem, named after the 18th century Comte de Buffon. The problem is the following:

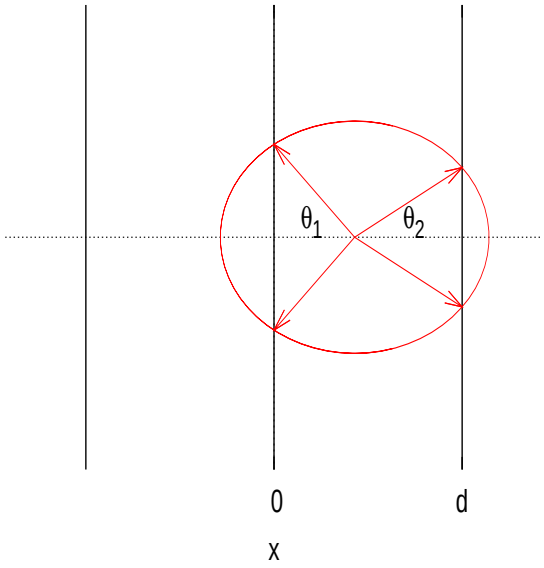

Figure 2.1: Buffon's needle.

A needle of length l is randomly thrown on a plane containing parallel lines separated by a distance d. (Fig. 2.1):

What is the probability that the needle will cross a line?

Suppose that one end of the needle landed at a distance x to the right of a line, and the needle makes an angle θ from the horizontal direction. (The lines run vertically.) Assume x is uniformly distributed from 0 to d, and θ is uniformly distributed from 0 to 2π, and assume that $l < d$ for simplicity, so that the needle can cross only one vertical line at most. Then

$$P(crossing) = \frac{1}{2\pi d} \int_{x=0}^{d} dx \left(\int_{\theta=-\theta_1}^{\theta_1} d\theta + \int_{\theta=-\theta_2}^{\theta_2} d\theta \right)$$

$$= \frac{1}{2\pi d} \int_{x=0}^{d} \left(2\theta(l-x)\cos^{-1}\frac{x}{l} + 2\theta(l+x-d)\cos^{-1}\frac{d-x}{l} \right) dx \;=\; \frac{2l}{\pi d} \qquad (2.1)$$

The θ-function makes sure that the expression under integral is always defined. So, by throwing a needle, we can calculate π: if we made N experiments, and in $N_{crossing}$ cases

the needle did cross a line, then

$$\pi \approx \frac{2l}{d}\frac{N}{N_{crossing}} \tag{2.2}$$

The "official" history of the Monte Carlo method starts in 1946 in Los Alamos, when Stanislaw Ulam had the first idea to use the method in difficult science/mathematics problems.[24] The name comes from the famous Monaco casino where people gamble, and thus use random numbers. The idea was much discussed between Ulam, von Neumann and Metropolis. The fact that they had at their disposal the first general purpose computer, ENIAC, was of particular importance - you need a computer to do any really intensive Monte Carlo calculations. Since then, much progress was made, and Monte Carlo methods are an integral part of science and technology now.

2.1.2 Integrals

It is good to be able to calculate integrals precisely, or to give an analytical formula for the answer. However, it is not always possible in many real life problems. We have to resort to numerical methods. Next I'll give a simple example of using Monte Carlo method for calculating an integral.

Monte Carlo Method Example: Calculating Area of a Circle

The area of a circle can be expressed as a 2-dimensional integral over area:

$$A = \int_S dxdy \tag{2.3}$$

Alternatively, integration may be done over larger area of enclosing square:

$$A = \int f(x,y)dxdy, \qquad f(x,y) \equiv \begin{cases} 1, & (x,y) \text{ inside circle} \\ 0, & \text{otherwise.} \end{cases} \tag{2.4}$$

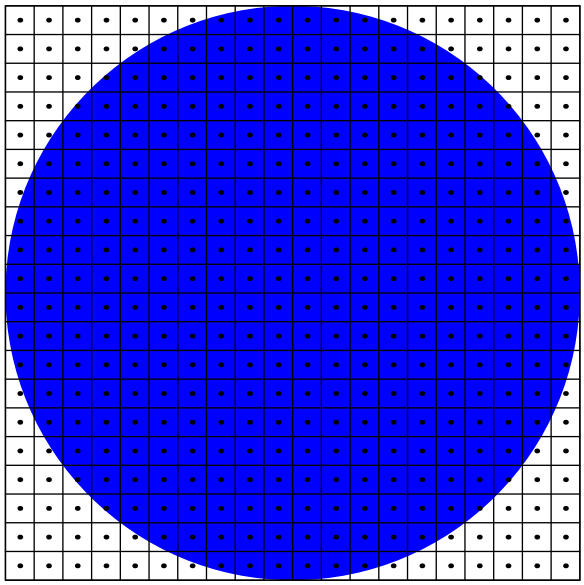

Figure 2.2: Calculating area of a circle with a grid of points.

We have a square of area $S(square)$, divided into n little squares of an area ΔS_i each. The integral sum is

$$A = \sum f(x_i, y_i)\Delta S_i, \tag{2.5}$$

where sum is taken over grid of points at equal spacing (Fig. 2.2):

$$A = \frac{S(square)}{n} \sum_{i=1}^{n} f(x_i, y_i) \tag{2.6}$$

Next we modify the method to Monte Carlo method:

The expression for the sum is the same, but now points (x_i, y_i) are chosen **randomly** (Fig. 2.3).

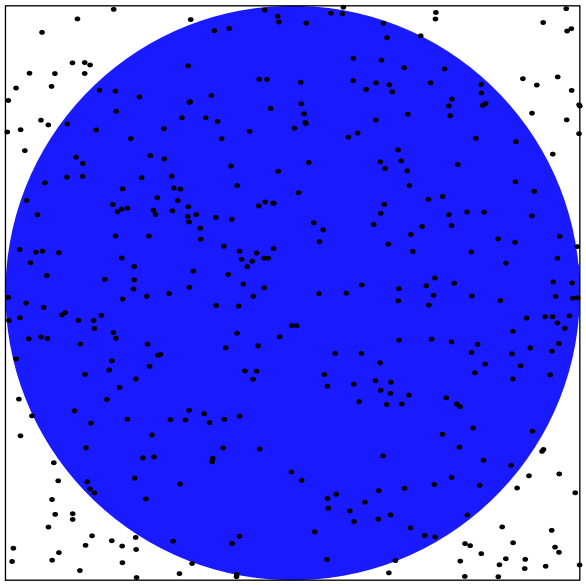

Figure 2.3: Calculating area of a circle with random points.

A simple program calculating π through the area of a circle $S(circle)$:

$$\pi = \frac{\pi r^2}{r^2} = \frac{4\ S(circle)}{S(square)} \tag{2.7}$$

```
#include <stdio.h>
#include <stdlib.h>
#include <math.h>

double pi=3.14159265358979323846;
int main()
{
 double x,y,pix;
 int n,nin=0;
 for(n=1;n<999999999;n++)
  {
   x=rand()/(double)RAND_MAX; /* Select random x,  0<x<1 */
   y=rand()/(double)RAND_MAX; /* Select random y,  0<y<1 */
   if((x*x+y*y)<1)nin++;      /* If (x,y) inside the circle => increase nin */
   pix=(double)4 * nin / n;   /* pi= 4 nin / n = 4 S(circle) / S(square) */
   if((n % 10000) == 0)
    {
     printf("*pix=%f** rel. error=%f** n=%d*\r",pix,(pix-pi)/pi, n);
    }
  }
 printf("\n");
}
```

Here are results of running the program for different values of n. The code was executed 100 times for each n to get error bars

n	π	
100	3.1516	± 0.0017
1000	3.1409	± 0.0005
10000	3.1412	± 0.00015
100000	3.1416	± 0.00003

This table illustrates an important feature of Monte Carlo. One can see that the error bars are going down roughly by a factor of 3 each time n increases by a factor of 10. Indeed, the error bars in monte carlo do go down as $1/\sqrt{n}$, assuming all the measurements are independent.

Above we illustrated how random numbers can be used to generate a value for π. Now we discuss how they can be used for integration. Integration arises in the most basic formula of quantum mechanics, the calculation of the average value of an observable A of a system with wave function ψ, given by:

$$\langle A \rangle = \langle \psi | A | \psi \rangle = \int \psi^*(\vec{x}) A(\vec{x}) \psi(\vec{x}) d^n x; \tag{2.8}$$

For many-particle systems, the dimension of the integral may be very high: $n = md$, where m is the number of particles and d is the physical dimension. While integration is a necessary technique in all areas of physics, in statistical mechanics / condensed matter it is particularly important, due to the large size and complexity of the studied systems. For numerical integration Monte Carlo methods are particularly suitable.

Numerical integration in one dimension is done by discretizing the integration domain (a, b) into N intervals of length $\epsilon = (b - a)/N$. If the trapezoidal rule is used, the error α goes as ϵ^2. Since the cpu time $T \propto N$ the time required to get a given accuracy is $T \propto N \propto \epsilon^{-1} \propto \alpha^{-1/2}$. Decreasing the error by a factor of four requires only a doubling

of the cpu time.

Now consider $d = 2$. Two variables must be discretized and the number of intervals N grows as ϵ^{-2}. Thus the cpu time $T \propto \alpha^{-1}$. In general, in d dimensions, it is easily seen that $T \propto \alpha^{-d/2}$. If $d = 10$, a very low dimensional integration in statistical mechanics, reducing the error by a factor of two requires a factor of 32 increase in cpu time.

Thus we see that traditional numerical integration through discretization of the variables is incredibly inefficient in high dimensions. We saw in our results for the calculation of π that in Monte Carlo the error α goes as $1/\sqrt{n}$ and hence $T \sim n \sim \alpha^{-2}$. $d = 4$ is the cross-over dimension where the cpu time scaling of Monte Carlo methods, $T \propto \alpha^{-2}$ has the same exponent as discretization. In any $d > 4$ monte carlo is more efficient. (The exact cross-over dimension depends on the integration sceme used. The remarks above are for the trapezoidal rule. But the same general idea applies for other methods like Simpson's rule as well.)

2.1.3 Central Limit Theorem

Here we argue that the error in Monte Carlo goes as $1/\sqrt{n}$. This central limit theorem is an important theoretical result, which provides justification for the wide use of Monte Carlo methods in very different circumstances and applied to very diverse systems.

Let $X_1, X_2, ...$ be independent random variables which are identically distributed (i.e. all have the same probability function in the discrete case, or density function in the continuous case) and have finite mean μ and variance σ^2. Then if $S_n = X_1 + X_2 + ... + X_n$,

$$\lim_{n\to\infty} P\left(a \leq \frac{S_n - n\mu}{\sigma\sqrt{n}} \leq b\right) = \frac{1}{\sqrt{2\pi}} \int_a^b e^{-u^2/2} du \tag{2.9}$$

I.e. the random variable $(S_n - n\mu)/\sigma\sqrt{n}$ is asymptotically normal.

If we use for each of X_i above values for some observable obtained in Monte Carlo

simulations, e.g. the mean value for Y:

$$X_i = \frac{1}{M}\sum_{j=1}^{M} Y_j^{(i)} \tag{2.10}$$

then if M is large enough, the distribution of X_i must be normal and we'll be able to estimate Y, and the error, with good precision if we make the simulation long enough. Importantly, the number of dimensions doesn't seem to matter. The precision of Monte Carlo simulation is roughly $\sim 1/\sqrt{M}$.

2.1.4 Transition Probabilities and Detailed Balance

Suppose our computer has stored in its memory a particular configuration i of a system. Our goal is to figure out a rule T_{ji} to evolve the configuration i into the configuration j which will generate configurations with a desired probability. More precisely, our process will not be deterministic, but will involve random changes, so T_{ji} will be the probability to generate j from i. Because probabilities are non-negative, and sum up to unity, the rule T_{ji} satisfies,

$$T_{ji} \geq 0 \tag{2.11}$$

$$\sum_j T_{ji} = 1. \tag{2.12}$$

A matrix obeying these two restrictions is called a stochastic matrix. Its eigenvalues obey $|\lambda| \leq 1$. Also, there is an eigenvector with eigenvalue $\lambda = 1$. These facts are simple to prove. Consider the eigenvector equation,

$$\sum_i T_{ji} v_i = \lambda v_j. \tag{2.13}$$

Take absolute values of both sides of the equation and use the fact that $T_{ji} \geq 0$ and the triangle inequality.

$$\sum_i T_{ji}|v_i| \geq |\lambda||v_j|. \tag{2.14}$$

Now sum both sides of the equation over j and use the fact that $\sum_j T_{ji} = 1$,

$$\sum_i |v_i| \geq |\lambda||v_j|. \tag{2.15}$$

We now see that $|\lambda| \leq 1$.

To show that a stochastic matrix has an eigenvalue of unity, consider the vector with all components the same, $v_j = 1$. Then, from the Eq. 2.12,

$$\sum_j v_j T_{ji} = v_i. \tag{2.16}$$

So the constant vector is a left eigenvector of T of eigenvalue 1. Remember that the eigenvalues of a matrix are the same whether one considers left or right eigenvectors, but the eigenvectors themselves can be quite different unless the matrix is symmetric. This is important to keep in mind, because we will be showing that the right eigenvector of T is not the trivial constant vector. In fact, the right eigenvector of T can be arranged to be any desired p_j, as shown below.

Because T is our rule for generating one configuration from the next, we can view the generation of a long sequence of configurations in the Monte Carlo process as the repeated application of the matrix T. We know that when we repeatedly apply a matrix to a vector, we project out the eigenvector of largest eigenvalue. As we have seen above, because T is stochastic, we will generate the eigenvector of eigenvalue 1.

So we can now make our goal a little bit more precise: We want to figure out T obeying Eq. 2.12 whose eigenvector of eigenvalue one is the vector of desired probabilities p_i. Then,

repeatedly applying T will give us p and we are done. It is easy to show that if we construct T to obey detailed balance,

$$T_{ji}p_i = T_{ij}p_j \tag{2.17}$$

then p_i is an eigenvector of T of eigenvalue 1:

$$\sum_i T_{ji}p_i = \sum_i T_{ij}p_j = p_j \sum_i T_{ij} = p_j. \tag{2.18}$$

It is also easy to formulate T to obey detailed balance. The most famous prescription is due to Metropolis. The Metropolis algorithm says that one suggests a move from i to j and then accepts the move with probability one if j is more likely than i, that is, if $p_j/p_i > 1$. If j is less likely than i, accept j with probability p_j/p_i. This obeys detailed balance because (assuming $p_j > p_i$) $T_{ji} = 1$ and $T_{ij} = p_i/p_j$.

2.1.5 Metropolis Algorithm

We now can give a summary of the algorithm:

- Randomly choose an initial position in a (configuration, Hilbert) space, $X_i = X_0$.
- MC loop
  - Suggest a "trial" configuration X_{trial}

by randomly changing one or more degrees of freedom.

  - Generate a random variable r uniformly distributed on $0 < r < 1$.

    If $r < P(X_{trial})/P(X_i)$, then accept step X_{trial} as a new position $X_{i+1} = X_{trial}$; otherwise retain X_i: $X_{i+1} = X_i$.

Observables are calculated as

$$\langle A \rangle = \frac{1}{N} \sum_{i=1}^{N} A(X_i) \tag{2.19}$$

Intuitively, it must be clear that thanks to the weighted steps, the algorithm will spend most of the time at points with relatively high probability. That is, if $P(X_{trial}) > P(X_i)$, then X_{trial} is always accepted, while if $P(X_{trial}) \ll P(X_i)$, then X_{trial} is mostly rejected. This is much more efficient than randomly selecting configurations as in the example of measuring π, especially if the probability space is infinite, or very large, but almost all of it has very low probability density.

2.1.6 Metropolis Algorithm for Statistical Mechanics

In classical statistical mechanics the probability of a configuration X_i is proportional to $e^{-\beta\epsilon(X_i)}$, where $\epsilon(X_i)$ is the energy of configuration and $\beta = 1/T$ where T =temperature. Straightforward substitution in the Metropolis algorithm gives:

- Choose initial configuration $X_i = X_0$.

- MC loop
  - Suggest trial configuration X_{trial}.
  - Generate a random variable r uniformly distributed on $0 < r < 1$.

    If $r < e^{\beta[\epsilon(X_i)-\epsilon(X_{trial})]}$, then accept step X_{trial} as a new configuration $X_{i+1} = X_{trial}$; otherwise retain X_i: $X_{i+1} = X_i$.

Note that if $\epsilon(X_{trial}) < \epsilon(X_i)$ then X_{trial} is always accepted. We always keep configurations that lower the energy.

Having reviewed classical Monte Carlo, we now turn to describing quantum Monte Carlo (DQMC). It will be seen that QMC reduces to a classical Monte Carlo problem in one higher dimension.

2.2 Determinant Quantum Monte Carlo

In this section we describe Determinant Quantum Monte Carlo method[25, 26] as applied to the Fermion Hubbard model. First we'll introduce the variation of Hubbard model Hamiltonian in particle-hole symmetric form[27]. We'll consider simpler cases of no hopping and no interaction. We then describe the Hubbard-Stratonovich transformation and how it applies to Hubbard model to make the full DQMC method. We then briefly describe some of the details, including approximation techniques and the ways of calculating the observables.

2.2.1 Hubbard Model Hamiltonian in particle-hole symmetric form

The Fermion Hubbard Hamiltonian in particle-hole symmetric form is

$$H = -t \sum_{\langle j,l\rangle\sigma} (c^{\dagger}_{j\sigma} c_{l\sigma} + c^{\dagger}_{l\sigma} c_{j\sigma}) + U \sum_{j} (n_{j\uparrow} - \frac{1}{2})(n_{j\downarrow} - \frac{1}{2}) - \mu \sum_{j} (n_{j\uparrow} + n_{j\downarrow}) \qquad (2.20)$$

Comparing 2.20 to Eqn. 1.12 in Chapter 1, we see that the formulas are equivalent, up to an adjustment of μ. The convenience of the formula 2.20 is that the interaction term is symmetric relative to the half-filling. In particular the density will be equal to one at $\mu = 0$ for any t, U, and temperature.

2.2.2 Case of No Hopping

In this case the Hamiltonian is a sum of N decoupled Hamiltonians, each of which represents one site. The one site Hamiltonian is

$$H = U(n_\uparrow - \frac{1}{2})(n_\downarrow - \frac{1}{2}) - \mu(n_\uparrow + n_\downarrow) \tag{2.21}$$

In the basis $\{\psi_i\}= |\cdot\rangle, |\uparrow\rangle, |\downarrow\rangle, |\uparrow\downarrow\rangle$ the Hamiltonian is diagonal:

$$H = \langle\psi_i|H|\psi_j\rangle = \begin{pmatrix} \frac{U}{4} & 0 & 0 & 0 \\ 0 & -\frac{U}{4} - \mu & 0 & 0 \\ 0 & 0 & -\frac{U}{4} - \mu & 0 \\ 0 & 0 & 0 & \frac{U}{4} - 2\mu \end{pmatrix} \tag{2.22}$$

The partition function

$$Z = Tr(e^{-\beta H}) = \sum_i \langle\psi_i|e^{-\beta H}|\psi_i\rangle = e^{-\frac{U}{4}\beta} + 2e^{(\frac{U}{4}+\mu)\beta} + e^{-(\frac{U}{4}-2\mu)\beta} \tag{2.23}$$

Expectation values of observables O are calculated as

$$\langle O\rangle = \frac{Tr(Oe^{-\beta H})}{Tr(e^{-\beta H})}. \tag{2.24}$$

For example, the density is

$$\langle n\rangle = \langle n_\uparrow + n_\downarrow\rangle = \frac{Tr((n_\uparrow + n_\downarrow)e^{-\beta H})}{Tr(e^{-\beta H})} = \frac{2e^{(\frac{U}{4}+\mu)\beta} + 2e^{-(\frac{U}{4}-2\mu)\beta}}{e^{-\frac{U}{4}\beta} + 2e^{(\frac{U}{4}+\mu)\beta} + e^{-(\frac{U}{4}-2\mu)\beta}} \tag{2.25}$$

As commented earlier, in the case of $\mu = 0$, $\langle n\rangle$=1, independent of U and β ("half-filling"). Fig. 2.4 shows a plot of density vs μ.

The energy is

$$\langle H\rangle = \frac{Tr(He^{-\beta H})}{Tr(e^{-\beta H})} = \frac{\frac{U}{4}e^{-\frac{U}{4}\beta} - 2(\frac{U}{4} + \mu)e^{(\frac{U}{4}+\mu)\beta} + (\frac{U}{4} - 2\mu)e^{-(\frac{U}{4}-2\mu)\beta}}{e^{-\frac{U}{4}\beta} + 2e^{(\frac{U}{4}+\mu)\beta} + e^{-(\frac{U}{4}-2\mu)\beta}} \tag{2.26}$$

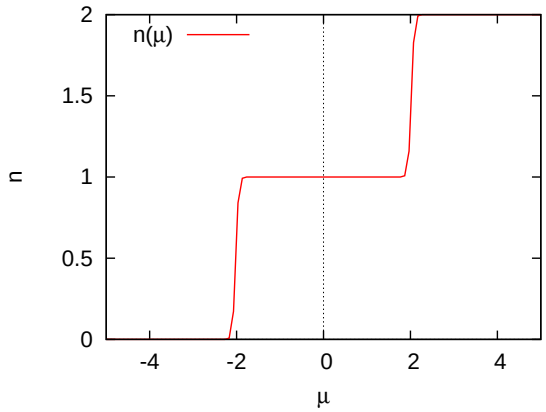

Figure 2.4: Case of no hopping ($t = 0$). Dependence of n vs μ at low temperature($\beta = 32$) and $U = 4$. $n(\mu)$ is almost a step-function, with 3 steps corresponding to 3 fillings: $n = 0$, $n = 1$ (Mott plateau at half filling), and $n = 2$.

2.2.3 Case of No Interaction

With no interaction ($U = 0$), the Hamiltonian is a sum of 2 decoupled Hamiltonians, each of which represents spin-up or spin-down. The one spin Hamiltonian is

$$H = -t \sum_{\langle j,l \rangle} c_j^\dagger c_l - \mu \sum_j n_j \tag{2.27}$$

The solution is achieved by a Fourier Transform into momentum space. In one dimension the Fourier Transform

$$c_l^\dagger = \frac{1}{\sqrt{N}} \sum_k e^{-ikl} c_k^\dagger, \tag{2.28}$$

where $k = k_n = 2\pi n/N$, $n = 0, 1, ..., N-1$. The Hamiltonian in momentum space becomes

$$H = -2t \sum_k (\cos k) n_k - \mu \sum_k n_k, \tag{2.29}$$

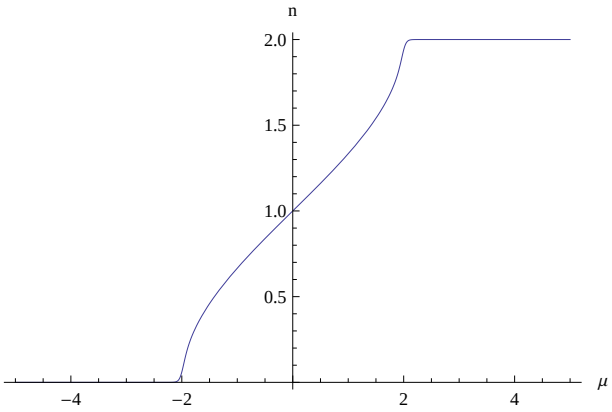

Figure 2.5: Case of no interaction ($U = 0$). Dependence of n vs μ at low temperature($\beta = 32$) and $t = 1$. Here the lattice is $d = 1$, so $-2t \leq E \leq 2t$.

where $n_k = c_k^\dagger c_k$, the number operator in momentum space. The Hamiltonian is diagonal, and the eigenvalues are

$$\epsilon_k = -2t \cos k - \mu \tag{2.30}$$

Fig. 2.5 shows a plot of density *vs* μ. The large slope of $dn/d\mu$ at $\mu = \pm 2$ is a consequence of the divergence of the density of states at the band edges.

Similarly, for the two dimensional square lattice Hubbard model, the eigenvalues are

$$\epsilon_{k_x,k_y} = -2t(\cos k_x + \cos k_y) - \mu \tag{2.31}$$

This dispersion relation has many interesting properties such as perfect nesting and a divergence of the density of states at half filling.

Quadratic Form and Determinant Quantum Monte Carlo

The essence of DQMC is in the following statement: If the Hamiltonian $\hat{H}$ is a quadratic form of fermion operators

$$\hat{H} = c^\dagger H c, \tag{2.32}$$

where H is an $N \times N$ Hermitian matrix, then

$$Tr(e^{-\beta\hat{H}}) = det[I + e^{-\beta H}] = \prod_{i=1}^{N}(1 + e^{-\beta\lambda_i}), \tag{2.33}$$

where λ_i are eigenvalues of H.

Proof. Diagonalizing the Hamiltonian (2.32), we get

$$\hat{H} = \sum_{i=1}^{N} \lambda_i c_i^\dagger c_i = \sum_{i=1}^{N} \hat{n}_i \tag{2.34}$$

$$Tr(e^{-\beta\hat{H}}) = Tre^{-\beta\sum_{i=1}^{N}\hat{n}_i} = Tr\left(\prod_{i=1}^{N} e^{-\beta\lambda_i\hat{n}_i}\right) = \prod_{i=1}^{N}\left(1 + e^{-\beta\lambda_i}\right), \tag{2.35}$$

where we used the fact that $\hat{n}_i$ has eigenvalues 0 and 1.

The Hubbard Hamiltonian has all terms in quadratic form, except the interaction term

$$U\sum_j (n_{j\uparrow} - \frac{1}{2})(n_{j\downarrow} - \frac{1}{2}), \tag{2.36}$$

which is quartic. The next subsection describes how the interaction term is converted into a quadratic form.

2.2.4 Hubbard-Stratonovich Transformation

The Hubbard-Stratonovich transformation is an operator analogy of the familiar Gaussian integral for a number A

$$e^{\frac{1}{2}A^2} = \sqrt{\frac{1}{2\pi}} \int_{-\infty}^{\infty} dx e^{-\frac{1}{2}x^2 - xA} \tag{2.37}$$

Note that quadratic A in LHS appears as linear in RHS, at the price of an extra integral by x. We can write a similar equation for operators $n_\uparrow$ and $n_\downarrow$

$$e^{-U\Delta\tau(n_\uparrow-1/2)(n_\downarrow-1/2)} = \sqrt{\frac{1}{2\pi}} e^{-\frac{U\Delta\tau}{4}} \int_{-\infty}^{\infty} dx e^{-\frac{1}{2}x^2+\sqrt{U\Delta\tau}x(n_\uparrow-n_\downarrow)} \tag{2.38}$$

Rather than use a continuous variable x it is somewhat more efficient to employ the discrete Hubbard-Stratonovich transformation

$$e^{-U\Delta\tau(n_{i\uparrow}-\frac{1}{2})(n_{i\downarrow}-\frac{1}{2})} = \frac{1}{2} e^{-\frac{U\Delta\tau}{4}} \sum_{s_i=\pm 1} e^{\lambda s_i(n_{i\uparrow}-n_{i\downarrow})} \tag{2.39}$$

where $\cosh\lambda = \frac{1}{2}e^{\frac{U\Delta\tau}{4}}$. This equation is valid because the eigenvalues of the Fermion number operator take only values of 0 and 1.

With the Hubbard-Stratonovich transformation, the Hubbard model Hamiltonian can be made completely quadratic, at the price of introducing the auxiliary field s_i, and can be used for DQMC algorithm, which we'll now describe.

2.2.5 Determinant Quantum Monte Carlo Algorithm

In order to apply Eq. (2.39) we need to isolate the exponential of the interaction term. We cannot, however, write $e^{-\beta(\hat{K}+\hat{V})} = e^{-\beta\hat{K}}e^{-\beta\hat{V}}$ since $[\hat{K},\hat{V}] \neq 0$. We proceed by dividing the imaginary-time interval $[0,\beta]$ into L equal subintervals of the width $\Delta\tau = \frac{\beta}{L}$:

$$Z = Tr(e^{-\beta H}) = Tr\left(\prod_{l=1}^{L} e^{-\Delta\tau H}\right) = Tr\left(\prod_{l=1}^{L} e^{-\Delta\tau H_K} e^{-\Delta\tau H_V}\right) + O(\Delta\tau^2), \tag{2.40}$$

where H_K and H_V are respectively kinetic and potential parts of the Hamiltonian. The key idea is that $e^{-\Delta\tau(H_K+H_V)} = e^{-\Delta\tau H_K}e^{-\Delta\tau H_V}$ becomes a better and better approximation as $\Delta\tau \to 0$. The kinetic term H_K is quadratic in Fermion operators, and spin-up and

spin-down operators are independent, so it can be written as a product

$$e^{-\Delta\tau H_K} = e^{-\Delta\tau H_{K\uparrow}} e^{-\Delta\tau H_{K\downarrow}}, \tag{2.41}$$

where

$$H_{K\sigma} = -t c_\sigma^\dagger K c_\sigma, \tag{2.42}$$

and $N \times N$ matrix K describes the hopping. For 1-D, K is tri-diagonal

$$K = \begin{pmatrix} 0 & 1 & 0 & ... & 1 \\ 1 & 0 & 1 & ... & 0 \\ ... & ... & ... & ... & ... \\ 0 & 0 & 0 & ... & 1 \\ 1 & 0 & 0 & ... & 0 \end{pmatrix} \tag{2.43}$$

The potential term is quartic in Fermion operators and we make it quadratic using Hubbard-Stratonovich transformation. We'll use the following theorem [25]: If operators $\mathcal{B}_l$ are quadratic forms of Fermion operators

$$\mathcal{B}_l = \sum_{i,j} c_i^\dagger (B_l)_{ij} c_j, \tag{2.44}$$

where B_l are matrices of real numbers, then

$$Tr(e^{-\mathcal{B}_1} e^{-\mathcal{B}_2} ... e^{-\mathcal{B}_L}) = det(I + e^{-B_L} e^{-B_{L-1}} ... e^{-B_1}). \tag{2.45}$$

This theorem is nontrivial to prove. However it can be seen to be true for $L = 1$ as argued in 2.34-2.35. See reference above for details.

The entire Hubbard-Stratonovich field consists of a set of $L = \beta/\Delta\tau$ vectors of dimension N (the number of spatial sites) $s_1, s_2, ..., s_l, ..., s_L$. Each of the vectors corresponds to one

time slice. We'll use s to denote the whole configuration of $\{s_l\}$, and s_{li} to an entry i at a particular spatial site of the vector s_l for time slice l.

The partition function now becomes

$$Z = CTr_s det(M_\uparrow(s))det(M_\downarrow(s)) \tag{2.46}$$

where C is a constant,

$$M_\sigma = I + B_{L,\sigma}(s_L)B_{L-1,\sigma}(s_{L-1})...B_{1,\sigma}(s_1), \tag{2.47}$$

where

$$B_{l,\uparrow(\downarrow)}(s_l) = e^{t\Delta\tau K}e^{+(-)\lambda V_l(s_l)}, \tag{2.48}$$

where $V_l(s_l) = diag(s_{l1}, s_{l2}, , , , s_{lN})$. The relative sign in 2.48 comes from 2.39.

DQMC Algorithm

- Initialize $s_{l,i} = \pm 1$
- MC loop (warm-up + measurement)
  - Loop $l = 1$ to L
    - Loop $i = 1$ to N
      - Propose a new configuration s' by flipping $s'_{l,i} = -s_{l,i}$
      - compute

$$r_{l,i} = \frac{det((M_\uparrow(s'))det(M_\downarrow(s'))}{det((M_\uparrow(s))det(M_\downarrow(s))} \tag{2.49}$$

      - Metropolis acceptance/rejection:

        Choose r = random number uniform[0,1]

        $r \leq r_{l,i} \Rightarrow$ accept the move: $s_{l,i} = s'_{l,i}$

Otherwise reject the move: $s_{l,i} = s_{l,i}$

- After warm-up, perform measurements, as described below.

2.2.6 Measurement of Observables

The observables can be obtained from the single-particle Green's function

$$G_{ij}^{\sigma} = \langle c_{i\sigma} c_{j\sigma}^{\dagger} \rangle = (M_{\sigma}^{-1}(s))_{ij} = \left([I + B_{L,\sigma}(s_L) B_{L-1,\sigma}(s_{L-1}) ... B_{1,\sigma}(s_1)]^{-1} \right)_{ij} \tag{2.50}$$

For example, the density of spin σ fermions on site i is calculated as

$$\rho_{i,\sigma} = \langle n_{i,\sigma} \rangle = \langle c_{i,\sigma}^{\dagger} c_{i,\sigma} \rangle = 1 - \langle c_{i,\sigma} c_{i,\sigma}^{\dagger} \rangle = 1 - G_{ii}^{\sigma} \tag{2.51}$$

Since the Hubbard Hamiltonian is translationally invariant, and up and down spins are equivalent, one can reduce error bars by averaging over all sites and spins

$$\rho = \frac{1}{2N} \sum_{\sigma} \sum_{i=1}^{N} \rho_{i,\sigma} \tag{2.52}$$

The kinetic energy is

$$\langle H_K \rangle = -t \langle \sum_{\langle i,j \rangle, \sigma} (c_{i,\sigma}^{\dagger} c_{j,\sigma} + c_{j,\sigma}^{\dagger} c_{i,\sigma}) \rangle = t \sum_{\langle i,j \rangle, \sigma} (G_{i,j}^{\sigma} + G_{j,i}^{\sigma}) \tag{2.53}$$

Various correlation functions also can be obtained from the Green's function. For instance, the s-wave superconducting order correlation function

$$\langle c_{SC}(j) \rangle = \langle c_{i+j,\downarrow} c_{i+j,\uparrow} c_{i,\uparrow}^{\dagger} c_{i,\downarrow}^{\dagger} \rangle = G_{i+j,i}^{\uparrow} G_{i+j,i}^{\downarrow} \tag{2.54}$$

Here $c_{i,\uparrow}^{\dagger} c_{i,\downarrow}^{\dagger}$ means creation of a pair on site i, and $c_{i+j,\downarrow} c_{i+j,\uparrow}$ means destruction of a pair on site $i + j$. If $\langle c_{SC}(j) \rangle$ stays finite as $j \to \infty$, then we have an off-diagonal long-range order (ODLRO), which means superconductivity.

Another observable of importance is the spin order correlation function, which probes magnetism,

$$\langle c_S(j)\rangle = \langle c^\dagger_{i+j,\downarrow} c_{i+j,\uparrow} c^\dagger_{i,\uparrow} c_{i,\downarrow}\rangle = G^\uparrow_{i+j,i} G^\downarrow_{i,i+j} \tag{2.55}$$

2.3 Canonical Worm Algorithm

In this section we'll describe the Worm algorithm, introduced starting from Path Integral Monte Carlo (PIMC), and its variation used in this work - the Canonical Worm algorithm. The DQMC method just described used a Hubbard-Stratonovich transformation to allow the fermion degrees of freedom to be integrated out analytically. The resulting Monte Carlo simulation was in the rather abstract space of the Hubbard-Stratonovich variables. An alternate approach, which works for fermions in 1D and bosons in all dimensions, is the "World Line" method. In this technique one does a monte carlo sampling of the positions of the original quantum particles, as they propagate spatially and in "imaginary time", ie as a function of $0 < \tau < \beta$. The reader is referred to the literature for the formulation of the most basic world line approaches[28]. Here we review only a more recent class of algorithms which allow a more efficient sampling of phase space and also a wider variety of measurements.

2.3.1 Worm Algorithm

The difference between the Worm algorithm[29] and conventional PIMC, is that it works in extended configurational space. This configurational space of the conventional PIMC contains only closed world line configurations, which we'll be calling Z or diagonal configurations. The Worm algorithm introduces open world line configurations, which we'll be calling G or off-diagonal configurations. The transitions are possible (and necessary for the algorithm to work) from G to Z sector by closing an open worldline, or removing it, and from Z to G sector by creating a new open worldline, or opening an existing closed

one. Expectation values, except that of the Green's function, are updated only from the Z sector.

Z sector

The Z sector is just the full configuration space of the conventional PIMC. We start from the grand partition function

$$Z = Tre^{-\beta(\hat{H}-\mu\hat{N})}. \tag{2.56}$$

(To avoid confusion: The use of Z for partition function is unrelated to the use for Z sector.) We need to represent Z in path integral form. We divide imaginary time into L slices of length $\Delta\tau = \beta/L$, and many-particle path is $X = (R_0, R_1, ..., R_L)$, where $R_L = R_0$, except possible permutations of particle labels, and the partition function

$$Z \approx \sum_{N=0}^{\infty} \int dX A(X, \Delta\tau) e^{-U(X)}. \tag{2.57}$$

where

$$A(X, \Delta\tau) = \prod_{j=0}^{L-1} \rho_F(R_j, R_{j+1}, \Delta\tau), \tag{2.58}$$

where ρ_F is a product of free-particle imaginary time propagators

$$\rho_F(R_j, R_{j+1}, \Delta\tau) = \prod_{i=1}^{N} \rho_0(r_{i,j}, r_{i,j+1}, \Delta\tau) \tag{2.59}$$

where

$$\rho_0(r, r', \Delta\tau) = (4\pi\lambda\Delta\tau)^{-d/2} e^{-\frac{(r-r')^2}{4\lambda\Delta\tau}}, \tag{2.60}$$

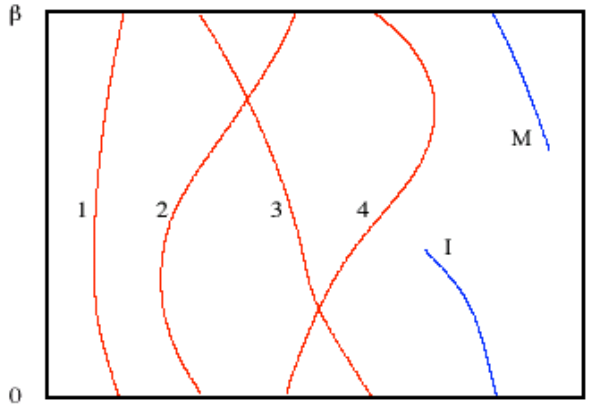

Figure 2.6: Basic idea: work in extended configuration space. Include 1 open World Line (worm) whose head and tail can advance and recede in imaginary time (From Boninsegni presentation at
*http : //online.itp.ucsb.edu/online/smatter_m*06/*boninsegni/pdf/Boninsegni_KITP.pdf*).

where $\lambda = \hbar^2/2m$. The function $U(X)$ incorporates correlations in space and imaginary time, arising from particle interactions.

In this representation, the configuration space is made up from N single particle paths (world lines), propagating in discretized imaginary time interval [0,β]. Each world line consists of L linked "beads". Due to the periodicity in imaginary time, each worldline must have its $(L-1)$st bead be linked to zeroth bead of itself, or another worldline. These exchange cycles arise from the indistinguishability of particles, and are essential to calculations.

G sector

The main idea of the Worm algorithm is that it introduces **open** worldlines (Figure 2.6). If we remove a link between jst and $(j+1)$st beads in some worldline, it will give us more choice in Monte Carlo moves. These disconnected beads - "head" and "tail" of a "worm" - may move separately around all space, may reconnect, or break another worldline and connect to it.

One of the main advantages is that now there are easily obtainable configurations with

non-zero winding, which are practically impossible to obtain in conventional PIMC except in very small space with periodic boundary conditions. Since winding is used to estimate superfluid density, it is important in simulations of superfluids.

Worm Monte Carlo moves

We'll now describe new Monte Carlo moves introduced in Worm algorithm. We refer the reader to the literature for the proof that these moves properly satisfy detailed balance. We will call open ends of a worldline by $\mathcal{I}$ and $\mathcal{M}$ (from *Ira* and *Masha* for historical reason).

(1a) Open. The move is only possible in diagonal (Z sector) configuration. A random worldline is selected, and a random number [0,L-1] beads, and connecting links are removed.

(1b) Close. The move is only possible in off-diagonal (G sector) configuration. It is a move opposite to (1a). The open worldline is closed, the ends $\mathcal{I}$ and $\mathcal{M}$ are reconnected, with missing beads and connecting links inserted.

(2a) Insert. It is another way to create off-diagonal configuration. A random open worldline is inserted.

(2b) Remove. It is a move opposite to (2a). The open worldline is removed.

(3a) Advance. The move advances the open worldline end $\mathcal{I}$ by a random number M of slices forward in time.

(3b) Recede. It is a move opposite to (3a). The move recedes the open worldline end $\mathcal{I}$ by a random number M of slices backward in time, removing M beads.

(4) Swap. The move is only possible in off-diagonal (G sector) configuration. It can be described as a combination of (1a) open and (1b) close. Originally we have one open worldline with ends $\mathcal{I}$ and $\mathcal{M}$. Let's take another worldline and open it, creating new open ends $\mathcal{I}'$ and $\mathcal{M}'$. Then, let's connect ends $\mathcal{I}$ and $\mathcal{M}'$. The remaining open ends $\mathcal{I}'$ and $\mathcal{M}$ now become $\mathcal{I}$ and $\mathcal{M}$. The *Swap* move produces all possible many-body permutations. Figure 2.7 illustrates the *Swap* move.

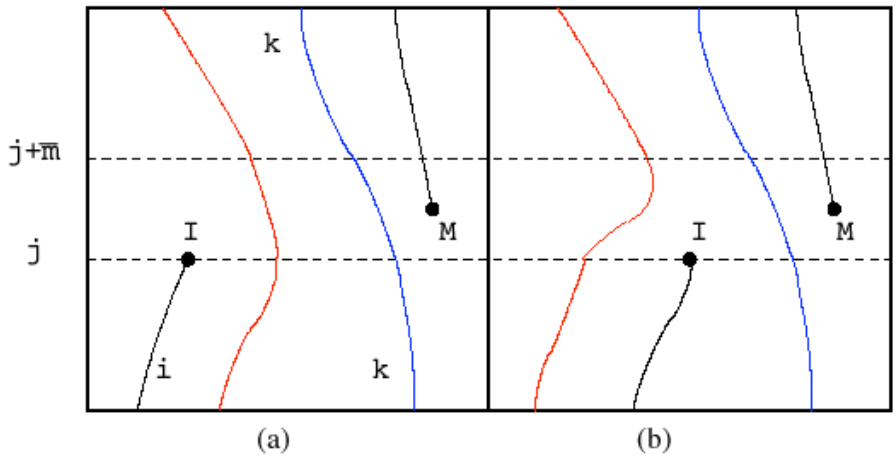

Figure 2.7: Head and tail of worm can swap with other World Lines (From Boninsegni presentation at
http : *//online.itp.ucsb.edu/online/smatter_m*06*/boninsegni/pdf/Boninsegni_KITP.pdf*).

Physical estimators

The physical estimators are computed from diagonal configurations (in Z sector). The computations therefore are identical to the ones of the conventional PIMC. The details may be found in the now classical Ceperley paper [30].

2.3.2 Canonical Worm Algorithm

As the name indicates, the Canonical Worm algorithm is a variation of Worm algorithm with the number of particles conserved. The Canonical Worm algorithm and code was created by Valy G. Rousseau and Peter Denteneer, and used in Chapter 4 of this work.

2.4 Mean Field Theory

In this section we'll give a short introduction to mean field theory, consider an example of Ising model, and then describe its application to the Hubbard model. An introduction to the mean field theory may be found in many, or most textbooks on the condensed matter, or statistical mechanics, e.g. Pathria [31]. This method is used in Chapter 6 of this thesis.

2.4.1 Introduction

A many-body system with interactions, such as a crystal, is usually very difficult, or impossible, to solve exactly. Mean field theory is an approximation of a system, neglecting fluctuations. Mean field theory may only be exact if the range of interactions is infinite. It is however a useful theory. When confronted with a new situation, mean field theory may be a first rough approximation, and give a useful idea of possible ordered phases. It also makes quantitatively correct predictions about some physical phenomena, like critical exponents in higher dimensions, where number of nearest neighbors is large.

2.4.2 An Example: Ising model

As an example, let us consider an Ising model in zero external field with Hamiltonian

$$H = -J \sum_{\langle ij \rangle} s_i s_j \tag{2.61}$$

We want to investigate the spontaneous magnetization. Defining an order parameter,

$$m = \frac{1}{N} \sum_i s_i = \frac{N_+ - N_-}{N}, \tag{2.62}$$

from which

$$N_+ = \frac{N}{2}(1+m), \quad N_- = \frac{N}{2}(1-m) \tag{2.63}$$

To do mean field approximation, we'll replace for each spin the sum of its q nearest neighbors spins with the sum of average:

$$H = -\frac{1}{2} qJm \sum_i s_i = -\frac{1}{2} qJNm^2, \tag{2.64}$$

where the factor $\frac{1}{2}$ is included to avoid double-counting of the nearest neighbor pairs.

The difference in energy at flipping one spin from up to down is

$$\Delta\epsilon = -Jqm\Delta s = 2Jqm. \tag{2.65}$$

According to the Boltzmann principle, the relative values of the equilibrium numbers N_+ and N_- are

$$\frac{N_-}{N_+} = e^{-\beta\Delta\epsilon} = e^{-2\beta qJm}, \tag{2.66}$$

or

$$\frac{1-m}{1+m} = e^{-2\beta qJm}, \tag{2.67}$$

which can be rewritten as

$$m = \tanh(\beta qJm) \tag{2.68}$$

The equation may be solved numerically. A non-zero solution for m exists if $\beta qJ > 1$, or $T < T_c = \frac{qJ}{k_B}$.

This example illustrates another name of mean field theory - self-consistent field theory: We put in an order parameter m, and after calculations, get as a result an order parameter. The goal of the calculations is to make the calculations consistent - so that the order parameter we put in equals the order parameter we calculate.

2.4.3 Implementation for Hubbard Model

Let us consider the Hubbard Hamiltonian

$$H = -t\sum_{\langle ij\sigma\rangle}(c^\dagger_{i\sigma}c_{j\sigma} + H.c.) + U\sum_i n_{i\uparrow}n_{i\downarrow} - \mu\sum_i n_i. \tag{2.69}$$

As noted earlier, if there were no quartic term, we could solve the model. We can simplify the problem, using mean field approach. We replace the quartic term with quadratic:

$$H = -t \sum_{\langle ij\sigma \rangle} (c^{\dagger}_{i\sigma} c_{j\sigma} + H.c.) + U \sum_{i} [n_{i\uparrow} \langle n_{i\downarrow} \rangle + n_{i\downarrow} \langle n_{i\uparrow} \rangle - \langle n_{i\uparrow} \rangle \langle n_{i\downarrow} \rangle] - \mu \sum_{i} n_i \quad (2.70)$$

We can make different assumptions about the averages. Here we will take $\langle n_{i\uparrow} \rangle$ and $\langle n_{i\downarrow} \rangle$ to be defined by combination of ferromagnetic and antiferromagnetic order parameters: Odd sites:

$$\langle n_{i\uparrow} \rangle = n + m_f + m_{af} \qquad \langle n_{i\downarrow} \rangle = n - m_f - m_{af} \quad (2.71)$$

Even sites:

$$\langle n_{i\uparrow} \rangle = n + m_f - m_{af} \qquad \langle n_{i\downarrow} \rangle = n - m_f + m_{af} \quad (2.72)$$

Self Consistency Conditions

The problem is solved self-consistently:

- Order parameters m_f, m_{af} set to initial values;
- Repeat until convergence:
    - m_f, m_{af} are put into Hamiltonian;
    - Hamiltonian diagonalized, obtaining eigenvalues $E_{k\sigma}$ and eigenfunctions $\psi_{k\sigma}$;
    - From the solution, recompute m_f, m_{af}:

$$m_f = \frac{1}{N} \sum_{i} (n_{i\uparrow} - n_{i\downarrow}) \quad (2.73)$$

$$m_{af} = \frac{1}{N} \sum_{i} (-1)^i (n_{i\uparrow} - n_{i\downarrow}) \quad (2.74)$$

where $n_{i\sigma}$ - occupancy of site i with spin-σ particles:

$$n_{i\sigma} = \sum_k |\psi_{ki\sigma}|^2 f_{k\sigma} \tag{2.75}$$

where f_k is Fermi-Dirac distribution function

$$f_{k\sigma} = \frac{1}{1 + e^{\beta(E_{k\sigma} - \mu)}} \tag{2.76}$$

and $\psi_{ki\sigma}$ is the ith component of the eigenfunction $\psi_{k\sigma}$. For the simple ansatz of Eqs. 2.71 and 2.72 we can get $E_{k\sigma}$ analytically. In general the eigenvalues might be computed numerically using a matrix diagonalization package.

Minimization of Free Energy and Self Consistency

It is known that the system at equilibrium must have minimum of Helmholtz free energy. The correct algorithm therefore must be minimizing free energy with respect to the order parameters. It can be shown that the self-consistency satisfies the minimum of free energy condition.

The free energy can also be calculated in Mean Field Theory

$$F = -\frac{1}{\beta} \sum_{k\sigma} \ln \left(1 + e^{-\beta(E_{k\sigma} - \mu)}\right) - U \sum_i \langle n_{i\uparrow} \rangle \langle n_{i\downarrow} \rangle \tag{2.77}$$

The condition $-\frac{\partial F}{\partial \mu} = N$ works here because

$$-\frac{\partial F}{\partial \mu} = \frac{1}{\beta} \sum_{k\sigma} \left(1 + e^{-\beta(E_{k\sigma} - \mu)}\right)^{-1} e^{-\beta(E_{k\sigma} - \mu)} \beta = \sum_{k\sigma} \frac{1}{e^{\beta(E_{k\sigma} - \mu)} + 1} \tag{2.78}$$

Also, the minimization of F with respect to $\langle n_{i\sigma} \rangle$ automatically makes the occupations self consistent.

$$\frac{\partial F}{\partial \langle n_{i\sigma} \rangle} = -\frac{1}{\beta} \sum_k \left(1 + e^{-\beta(E_{k,-\sigma} - \mu)}\right)^{-1} e^{-\beta(E_{k,-\sigma} - \mu)} \frac{\partial E_{k,-\sigma}}{\partial \langle n_{i\sigma} \rangle} (-\beta) - U \langle n_{i,-\sigma} \rangle, \tag{2.79}$$

Setting it to zero yields

$$\langle n_{i,-\sigma}\rangle = \frac{1}{U}\sum_k \left(e^{\beta(E_{k,-\sigma}-\mu)}+1\right)^{-1} \frac{\partial E_{k,-\sigma}}{\partial\langle n_{i\sigma}\rangle} \tag{2.80}$$

Consider now the effect of a perturbation of the ith diagonal entry of a matrix on its ith eigenvalues $H = H_0 + V$, where $V_{nm} = \delta_{in}\delta_{im}U$:

$$E_{k\sigma} = E^0_{k\sigma} + \langle\psi^0_{k\sigma}|V|\psi^0_{k\sigma}\rangle = E^0_{k\sigma} + |\psi^0_{k\sigma i}|^2 U. \tag{2.81}$$

Applying it to Eq. 2.80, we get

$$\langle n_{i,-\sigma}\rangle = \sum_k \left(e^{\beta(E_{k,-\sigma}-\mu)}+1\right)^{-1} |\psi_{k,-\sigma i}|^2. \tag{2.82}$$

This is precisely the self consistency equation.

2.5 Summary

Having reviewed the key methods used in our thesis work, we now turn to discussing specific applications of these techniques to superfluid, magnetic, and Mott transitions in interacting quantum systems.

Part II

Applications

Chapter 3

Monte Carlo Simulations of an Extended Feynman Kikuchi Model

Most of the contents of this chapter first appeared in Physical Review B 76, 174524 (2007). It is a collaborative work with Professor Scalettar.

We present Monte Carlo simulations of a generalization of the Feynman-Kikuchi model which includes the possibility of vacancies and interactions between the particles undergoing exchange. By measuring the winding number (superfluid density) and density structure factor, we determine the phase diagram, and show that it exhibits regions which possess both superfluid and charge ordering.

3.1 Introduction

The study of continuum superfluid phase transitions using Monte Carlo (MC) methods has a history which includes path integral simulations of Helium using realistic interatomic potentials, which capture T_λ in good quantitative agreement with experiment [12], to recent numerical work [33] focusing on experiments [34, 35] which observe 'supersolid' order [36], the simultaneous presence of both superfluidity and long range density correlations. Kim

and Chan [34] in their experiment use torsional oscillator to detect supersolidity and measure supersolid partof the solid helium, in much the same way as Andronikashvili used it to detect superfluidity and measure superfluid part of the liquid helium. Their torsional oscillator measurements on solid helium grown inside a porous Vycor glass disc show a decrease in the resonant period, which indicates supersolid state.

At the same time, related path integral studies of lattice models (the 'boson-Hubbard' Hamiltonian) [37, 38] have been undertaken. These too have been partially motivated by the issue of supersolid order, but have also been driven by the possibility of studying the universal conductivity in granular superconductors [39], and superfluid-Mott insulator transitions of relevance to optically trapped atoms [38]

Many of these simulations emphasize Feynman's picture of the connection between the superfluid transition and the increasing entanglement (and ultimate development of macroscopic 'winding' across the whole sample) of quantum paths as the temperature is lowered. Indeed, the superfluid density ρ_s is proportional to the mean square winding of paths around the lattice[12].

However, even before the advent of these large scale QMC simulations which allow the study of the superfluid transition exactly, Feynman[11] and Kikuchi[40, 41] suggested, and studied analytically, an approximate 'classical' model whose configurations are permutation loops of sites on a $d = 3$ lattice. The partition function they suggested is,

$$Z = \int \prod_{i=1}^{N} d\mathbf{r}_i \sum_{\mathcal{P}} \rho(\mathbf{r}_1, \mathbf{r}_2, \cdots, \mathbf{r}_N) \times \exp\left[\; - \frac{m_{\rm eff} k_{\rm B} T}{2\hbar^2} \sum_i (\mathbf{r}_i - \mathcal{P}\mathbf{r}_i)^2 \; \right] . \tag{3.1}$$

Here $m_{\rm eff}$ is the effective mass of He atoms, and the function $\rho(\mathbf{r}_1, \mathbf{r}_2, \cdots, \mathbf{r}_N)$ is assumed to be nonvanishing only when the coordinates $\mathbf{r}_i$ are located on the sites of a regular lattice (a cubic lattice in the original treatments). $\mathcal{P}$ refers to a permutation of the coordinates. A transition to a 'superfluid' phase where a macroscopic number of sites participate in a

single large loop, as the temperature T is lowered, was discovered and investigated.

Various approximations were employed to determine the properties of this model, predominantly diagrammatic (series) expansions in the exchange loops. To faclitate these analytic treatments, in many of the early studies the allowed permutations were restricted to "near-neighbor" exchange in which the maximum "distance traveled" by each particle i, is only one lattice constant d. That is, $|\mathbf{r}_i - \mathcal{P}\mathbf{r}_i| = d$ or zero for all particles i. One of the early issues concerned whether the superfluid transition was third order, as originally found by Feynman [11], or second order [42, 43, 44, 45] and whether the order was affected by the restriction to near-neighbor exchange. Another issue was the behavior of the specific heat, both how to eliminate various artificial structures (and even negative values) near the phase transition, and also how to recover the experimentally observed T^3 behavior in superfluids at low temperatures. Here the removal of the restriction to local permutations was found to be crucial [41].

The Feynman-Kikuchi (FK) model is closely related to the duality-transformed XY model [46, 47], where the partition function can also be expressed in terms of sums of closed paths on a lattice. The allowed configurations are somewhat different, since in the XY case path overlap is allowed whereas in the FK model, each $\mathbf{r}_i$ appears only once in $\mathcal{P}\mathbf{r}_i$. However, the energy for paths grows quadratically with the overlap, so that in practice large overlaps are unlikely, enhancing the similarities between the partition functions. This connection is perhaps not so surprising since both models offer ways to understand the superfluid phase transition.

In this paper we will study the FK model in $d = 2$ using Monte Carlo simulations [47]. Motivated by recent work on supersolids, we will then suggest a generalization which contains 'vacancies' and interactions between the occupied sites. We will determine the nature of the superfluid phase transition, and how it depends on particle density, and also study the possibility of charge ordered states arising from the interactions. The results allow us to construct the phase diagram of our generalized FK model.

3.2 Model and Computational Methods

We begin by briefly reviewing the motivation for the FK model which will expose the connection with exact path integral expressions for the partition function. Consider the quantum Hamiltonian for a system of N interacting bosons,

$$\hat{H} = \sum_{i=1}^{N} \frac{\hat{\mathbf{p}}_i^2}{2m} + V(\hat{\mathbf{r}}_1, \hat{\mathbf{r}}_2, \cdots \hat{\mathbf{r}}_N) \ . \tag{3.2}$$

Here $\hat{\mathbf{p}}_i$ and $\hat{\mathbf{r}}_i$ are the momentum and position operators. The partition function is given by,

$$\begin{aligned} Z &= \mathrm{Tr}\, e^{-\hat{H}/T} = \mathrm{Tr}\left[e^{-\epsilon \hat{H}/T} \cdots e^{-\epsilon \hat{H}/T} \right] \\ &\approx \mathrm{Tr}\left[e^{-\epsilon \hat{K}/T}\, e^{-\epsilon \hat{V}/T} \cdots e^{-\epsilon \hat{K}/T}\, e^{-\epsilon \hat{V}/T} \right] \end{aligned} \tag{3.3}$$

where, following the usual the path integral approach [48, 49], a small parameter ϵ has been introduced, the exponential of the full Hamiltonian has been broken into M pieces with $M\epsilon = 1$, and then approximated by the product of the exponentials of the kinetic and potential energies individually. This 'Trotter' approximation[50, 51, 52] becomes exact in the limit $\epsilon \to 0$ ($M \to \infty$). We have set Boltzmann's constant $k_{\mathrm{B}} = 1$ for simplicity.

The trace is evaluated by summing over a complete set of position eigenstates, and also inserting additional complete sets of position eigenstates throughout the string of incremental imaginary time evolution operators. The potential energy exponentials act on the eigenstates to give numbers, and the remaining matrix elements of the kinetic energy

operators are readily computed, yielding,

$$\begin{aligned} Z &= \sum_{\mathcal{P}} \int \prod_{i=1}^{N} \prod_{m=1}^{M} d\mathbf{r}_i^m \, e^{-S} \\ S &= \frac{\epsilon}{T} \sum_{m=1}^{M} V(\mathbf{r}_1^m, \mathbf{r}_2^m, \cdots \mathbf{r}_N^m) \\ &+ \frac{\epsilon}{T} \sum_{m=1}^{M} \sum_{i=1}^{N} \big[\frac{\mathbf{r}_i^{m+1} - \mathbf{r}_i^m}{\epsilon/T} \big]^2 \, . \end{aligned} \tag{3.4}$$

Here the superscript m is an 'imaginary time' index which labels the point of insertion of the different complete sets of states. The final set of positions $\{\mathbf{r}_i^M\}$ is constrained to be a permutation $\mathcal{P}$ of the original positions $\{\mathbf{r}_i^1\}$, as a consequence of the trace in the definition of the quantum partition function. The sum over permutations $\mathcal{P}$ incorporates the indistiguishability of the bosonic particles. This completes the representation of the partition function as an integral over classical paths in space and imaginary time.

Examination of this *exact* expression for the partition function, now readily motivates the origin of the FK model. The function $\rho(\mathbf{r}_1, \mathbf{r}_2, \cdots, \mathbf{r}_N)$, and its restriction to a cubic lattice, can be thought of as arising from the potential energy terms which act to tend to localize the particle positions in a regular array. The *single* exponential in the particle positions in the FK model can be regarded as a truncation of the complete set of M exponentials for all imaginary times. Notice that the combination of the leading factor ϵ/T and the two such factors in the denominator of the 'kinetic energy' lead to the appearance of the temperature in the *numerator*. From the viewpoint of the original path integral, this reflects the fact that as the temperature is lowered, the paths have more (imaginary) time in which to propagate, and it becomes increasingly easy for them to permute. Physically, this then leads to a superfluid phase transition as T is lowered.

In this paper, we will work with the FK model on a two dimensional square lattice. We will denote by β the inverse of the prefactor of the sum of the distances traveled by

the individual particles. That is, our partition function will be,

$$Z = \sum_{\mathcal{P}} \exp\big[- \frac{E}{\beta}\big] = \sum_{\mathcal{P}} \exp\big[- \frac{1}{\beta} \sum_{i} (\mathbf{r}_i - \mathcal{P}\mathbf{r}_i)^2\big] \tag{3.5}$$

To be explicit, to a labeling of the sites of the two dimensional square lattice, illustrated in Fig.3.1(left) we associate a permutation $\mathcal{P}$. An example is shown in Fig.3.1 (right). This configuration contains three nontrivial permutation loops: The particles at sites 8 and 9 are in a 'two particle' loop, as are the particles at sites 5 and 18. Note that in the former each particle moves a single lattice site, and contributes '1' to the energy, while the square of the distances traveled by each particle in the latter case is 5. The fourth and fifth rows contain a loop of five particles (moving distances $(\mathbf{r}_i - \mathcal{P}\mathbf{r}_i)^2 = 5, 1, 2, 1,$ and 1) which extends ('winds') all the way across the lattice in the x direction. The remaining sites, which share the same labels in the left and right, correspond physically to particles which have not undergone an exchange. The total energy E of the three loops in this configuration $\mathcal{P}\mathbf{r}_i$ is $E = (1+1) + (5+5) + (5+1+2+1+1) = 22$.

The periodic boundary conditions produce an ambiguity in the definition of the energy, since there is more than one way in which to compute the distance traveled by each particle. We define the energy by choosing the smallest of such distances.

In order to monitor the superfluid phase transition we measure the winding across the lattice in the x and y directions. W_x counts the difference between the number of particles which move to the right across the vertical edge of the lattice and those which move to the left. An analogous definition applies for W_y across the top, horizontal edge. We define $W^2 = W_x^2 + W_y^2$. In the right panel of Fig.3.1, $W_x = 1$ and $W_y = 0$.

We now introduce our extension of the FK model to allow for vacancies. In so doing, we are motivated by recent work on 'supersolid' phases [34, 33] which are, in fact, continuations of an extensive history. In the configuration in the right panel of Fig.3.1, each site is labeled by one of the 36 sites in the left panel. All sites are occupied. We can define a set of 'vacancies' by assigning '0' to a subset of the sites in the lattice (Fig. 3.2, left). An

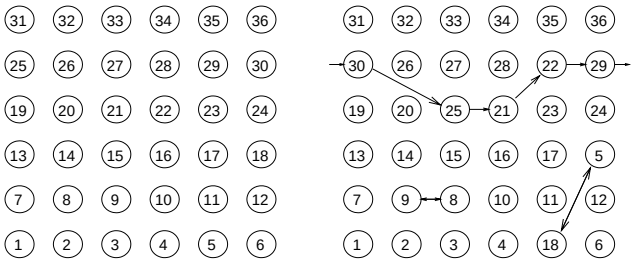

Figure 3.1: Left: Unpermuted labeling of the sites in a 6×6 lattice. Right: Representative configuration in our simulation. The energy $E = 22$ and the windings $W_x = 1, W_y = 0$. See text for explanation.

allowed configuration $\mathcal{P}(\mathbf{r}_i)$ of the system has zeroes at the same sites as the vacant sites in $\mathbf{r}_i$ and the occupied site labels are permuted. An example is given in Fig.3.2 (right). By a similar calculation to that described for Fig.3.1, the configuration shown has energy $E = 20$. Note that we will consider "annealed" vacancies: the vacancy density is fixed, but the system is allowed to sample all possible density locations satisfying that global constraint.

Once vacancies are allowed, it is possible to introduce additional terms in the summand of the partition function which control their relative positions on the lattice. We choose to add the simplest possible term,

$$\begin{aligned} E_v &= +V \sum_{\langle ij \rangle} (1 - \delta_{0,\mathcal{P}\mathbf{r}_i}) (1 - \delta_{0,\mathcal{P}\mathbf{r}_j}) \\ &= +V \sum_{\langle ij \rangle} (1 - \delta_{0,\mathbf{r}_i}) (1 - \delta_{0,\mathbf{r}_j}) \ . \end{aligned} \tag{3.6}$$

The sum is over neighboring sites $\langle ij \rangle$ of the lattice. E_v adds V to the energy for each link which connects sites both of which are occupied. As emphasized in Eq. 3.6, this number is the same whether the permuted or unpermuted sites are used in the summand, since

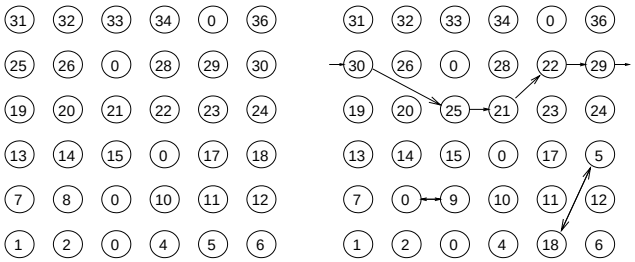

Figure 3.2: Left: Unpermuted labeling of the sites in a 6×6 lattice when the number of bosons $N_b = 31 < 36$. Empty sites are labeled by zeroes. Right: Representative configuration in our simulation of our extension of the FK model after two monte carlo moves. In the larger exchange move, no vacancies are involved, and only the site labels have been permuted relative to the panel at left. In the vacancy move, from site 9 to site 8, the site labels change as well. See text for further explanation.

the collection of occupied sites before and after the exchanges is the same.

The resulting partition function combines the original FK exchange term and the new interaction term,

$$\begin{aligned} Z &= \sum_{\mathcal{P}} \exp\Big[-\frac{1}{\beta}\sum_i (\mathbf{r}_i - \mathcal{P}\mathbf{r}_i)^2 \\ &- \beta V \sum_{\langle ij \rangle} (1 - \delta_{0,\mathcal{P}\mathbf{r}_i})\,(1 - \delta_{0,\mathcal{P}\mathbf{r}_j})\Big] \,. \end{aligned} \tag{3.7}$$

The inverse temperature β appears in the interaction term in its usual place.

We conclude this section by briefly discussing our simulation algorithm. Our approach is a straightforward implementation of the Metropolis Monte Carlo method [53]. We suggest a change in our permutation which consists of interchanging two, randomly selected, entries $\mathcal{P}\mathbf{r}_i$ and $\mathcal{P}\mathbf{r}_j$ in the permutation $\mathcal{P}$. If a vacancy is moved, the list of occupied sites and their permutation must be changed accordingly. The resulting change Δ in the argument of the exponential appearing in the partition function is evaluated, and the change

is accepted with probability $p = \min\left(1, e^{-\Delta}\right)$.

As with most path integral simulations, such local moves have difficulty evolving the configuration through phase space at large β where the important paths are dominated by large loops. We therefore also introduce 'global' moves which shift the elements $\mathcal{P}\mathbf{r}_i$ by one lattice constant for sites i across an entire column or row of the lattice. Such moves change the vertical or horizontal winding of the lattice by $\Delta W = \pm 1$. In some simulations such moves have low acceptance rates as the system size increases. Indeed, this is a primary limitation of simulations of real Helium [12]. However, we do not encounter this difficulty here.

3.3 Simulation Results: Feynman-Kikuchi Model

We begin by studying the original FK model. In Fig.3.3 we show data for the mean square winding $\langle W^2 \rangle$ as a function of β for different lattice sizes. We see that the winding becomes nonzero as β increases, and that the onset of nonzero winding becomes increasingly sharp as the lattice size grows. This raw data is suggestive of a critical $\beta_c \approx 0.6$ for the development of macroscopic loops. In simulations of the FK model in which only local exchanges are allowed, on a $d = 3$ cubic lattice [47], Elser finds $\beta_c \approx 0.69$. Presumably the higher dimensionality lowers β_c relative to our $d = 2$ square lattice while the restriction to local exchage would tend to raise β_c. Hence a rough match of the critical points is plausible.

We can make the case for a phase transition, and determine β_c with higher precision, by scaling our raw data. We adopt the usual ansatz [54] which postulates that the dependence of the order parameter on the parameter controlling the transition and on the lattice size takes the scaling form,

$$W^2\left(L, \beta\right) = L^a f\left[\, L^b(\beta - \beta_c)\,\right] . \tag{3.8}$$

Here f is a universal (lattice size independent) function of its argument, and a and b are

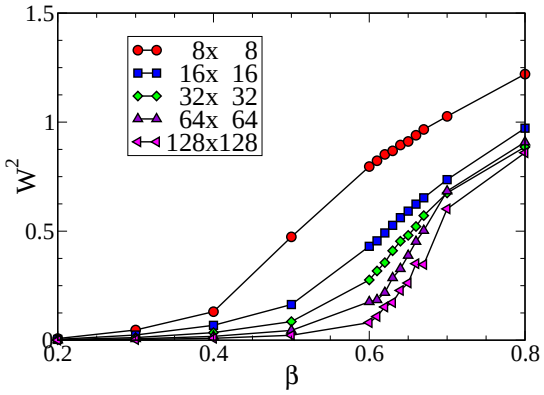

Figure 3.3: Raw data for the mean square winding as a function of β on lattice sizes ranging from 8×8 to 128×128.

critical exponents.

This scaling form is usefully rewritten as,

$$L^{-a} W^2 (L, \beta) = f\big[L^b (\beta - \beta_c) \big] \ . \tag{3.9}$$

From this expression it is clear that if we scale the order parameter $\langle W^2 \rangle$ by the lattice size to an appropriate exponent, $L^{-a} \langle W^2 \rangle$, and plot as a function of the control parameter β, all the curves will cross at the universal value $f(0)$ when $\beta = \beta_c$, regardless of the value of the second exponent b.

Fig.3.4 presents the results of the analysis in which the vertical (order parameter, $\langle W^2 \rangle$) axis alone is scaled. We observe a universal crossing of the five curves, and infer $\beta_c = 0.62 \pm 0.01$ and $a = 0.61 \pm 0.03$. We choose a using minimum mean square error estimation.

We calculate the average energy and specific heat from the partition function using the standard thermodynamics formulae,

$$\langle E \rangle = -\frac{\partial \ln Z}{\partial \beta} \qquad C = \frac{\partial E}{\partial T} \tag{3.10}$$

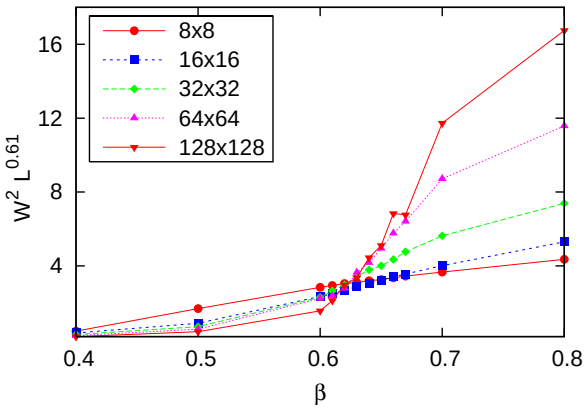

Figure 3.4: Raw data of Fig.3.3 for the mean square winding scaled by the lattice size. The intersection of the curves determines $\beta_c = 0.62 \pm 0.01$.

Fig. 3.5 shows a plot of specific heat as a function of temperature. We used the temperature rather than β as our horizontal axis, as is more conventional. We see that there is a peak in the specific heat at roughly the same position as the crossing of the winding $T_c = 1/\beta_c = 1/0.62 = 1.61$. The relatively large difference of T_c from the position of the peak is possibly due to the anomalous position of beta (in the denominator of the argument of the exponential), which creates the negative values of C at low T and small lattices, thus worsening the ability to extract Tc.

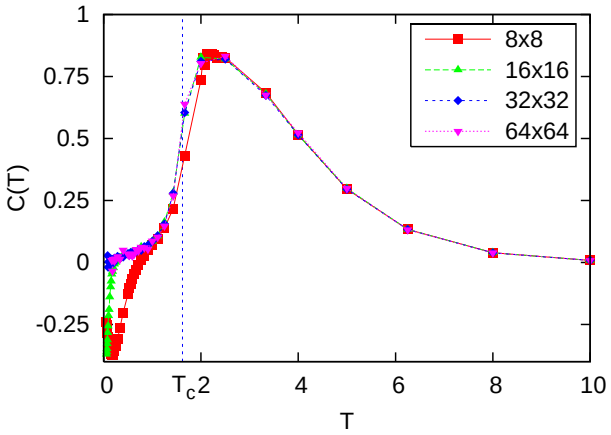

Figure 3.5: Plot of specific heat for the original FK model, that is, a fully filled lattice with no vacancies and no interactions. The value of the critical temperature inferred from the scaling of the winding (Fig. 3.4) is indicated as a vertical dotted line. The negative values of $C(T)$ at low T are a finite size artifact, as explained in the text.

The specific heat exhibits a sharp drop, and goes negative, close to $T = 0$. This is a non-physical effect which appears due to the finite size of the lattice, as can be seen as follows. Starting with the partition function of Eq. 3.5 we obtain,

$$E = -\frac{\partial \ln Z}{\partial \beta} = -\frac{1}{\beta^2}\frac{\sum_n K e^{-\frac{K}{\beta}}}{Z_0} = -\frac{1}{\beta^2}\langle E\rangle \tag{3.11}$$

where $Z_0 = \sum_n e^{-\frac{K}{\beta}}$ is the partition function used in Monte Carlo simulations; $\langle E\rangle$ is our MC calculation of energy. The specific heat

$$\begin{aligned} C &= \frac{\partial E}{\partial T} = \frac{\partial E}{\partial(1/\beta)} \\ &= -\frac{1}{\beta}\langle E\rangle + \frac{1}{\beta^2}\left(\langle E^2\rangle - \langle E\rangle^2\right) \\ &= -\frac{1}{\beta}B + \frac{1}{\beta^2}A \end{aligned} \tag{3.12}$$

For a finite lattice, as $\beta \to \infty$, A and B approach constant values given by all permutations on the $L \times L$ lattice having equal probability. As a consequence, as $\beta \to \infty$,

$$-\frac{1}{\beta}B + \frac{1}{\beta^2}A = \frac{1}{\beta^2}(A - B\beta) \ \to 0^-$$

So at large β, or small T, the specific heat becomes negative, achieves its minimum, and goes back to zero, as $T \to 0$. As the lattice size increases, the area of negative specific heat moves closer to $T = 0$. This is because the situation when all permutations have approximately equal probability occurs when $K/\beta \to 0$, or $L^2/\beta \to 0$, so $\beta \sim L^2$, or $T \sim L^{-2}$ for this area of negative specific heat.

Despite the crudity of the model, we can, following Feynman and Kikuchi[11, 40], use these results to infer a rough critical temperature for Helium, The scaling of the winding gives $\beta_c = 0.62$, or $T_c = 1.62$. To recover physical values for the temperature we note our unit is $T_1 = \hbar^2/k_B m d^2$, where m is the mass of boson, and d is lattice spacing. For ^{4}He, using density of 146 kg/m^3, and $d = 3.57 \cdot 10^{-10} m$, we obtain $T_1 = 0.95K$. This puts our

transition temperature around 1.5 K, which is in the same ballpark as T_λ for Helium.

We close this section by examining the low T behavior of the specific heat, since obtaining the proper exponent was the focus of much of the original work on the FK model. In three dimensions, where the initial analytic studies were performed, a linearly dispersing (phonon) mode $E(k) = ck$ gives $C(T) \sim T^3$ at low T. Here we are working in $d = 2$, where instead $C(T) \sim T^2$. Fig. 3.6 shows an attempt to fit $C(T)$ to a power law. The least squares fit gives $C(T) \sim T^{1.95\pm0.1}$ for lattices of different sizes, which is in reasonable agreement with the prediction based on a linearly dispersing mode. (We restrict our fit to temperatures higher than those at which the finite size artifact negative $C(T)$ values onset.)

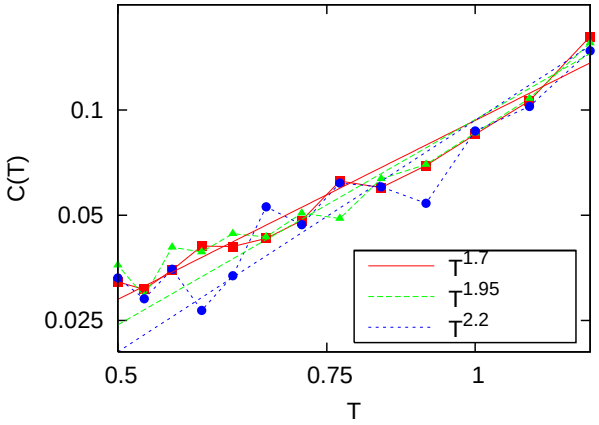

Figure 3.6: A log-log plot of specific heat versus temperature yields data consistent with a straight line of slope 1.95 ± 0.1, in agreement with the expected value, 2. We used a temperature range $0.5 \leq T \leq 1.25$, where T is small, but out of range of the (non-physical) dip in C.

3.3.1 Simulation Results: Feynman-Kikuchi Model with local constraints

For completeness, we now present analogous results for the model in which the local constraint on the paths in the permutations is included. The raw data for the winding is given in Fig. 3.7. Again we observe an onset of nonzero winding as β increases.

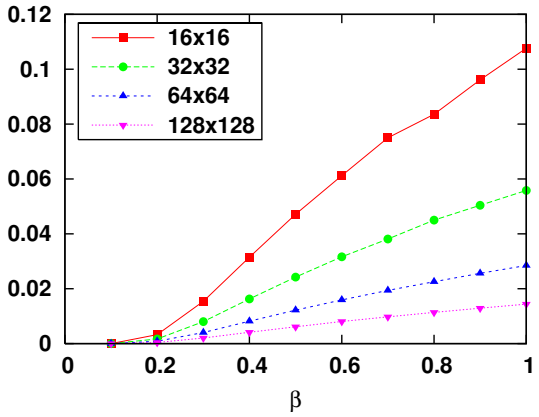

Figure 3.7: Raw data for the mean square winding as a function of β on lattice sizes ranging from 8×8 to 64×64. Here the permutations are constrained to allow only near-neighbor exchanges.

We use the same procedure of scaling as we did for the model without constraints. Scaling the order parameter $\langle W^2 \rangle$ by the lattice size to an appropriate exponent, $L^{-a}\langle W^2 \rangle$, we must get a universal crossing point.

Actually, here we get a complete collapse as shown in Fig. 3.8.

Having the total collapse means that we have for scaling $a = -1$ and $b = 0$. We can find β_c by setting $b \neq 0$ and guessing β_c. Trying β_c obtained in the previous case - a model without local constraint, we get reasonably good crossing on Fig. 3.9, but it's not quite at $T = T_c$. We need to find the best fitting β_c. Similarly to the model without local constraints, we get plot of specific heat - Fig. 3.10. Here we also got a negative region close to $T = 0$, but in difference to the model without constraints, it doesn't seem to depend on lattice size, and it indicates that there may be something wrong with the model with constraints.

3.4 Simulation Results: Extended Feynman Kikuchi Model

We now turn to our generalization of the FK model in which we allow a lattice with partial filling and a repulsive interaction V between nearest neighbor sites. We study first the special case of half-filling, where it is possible to have perfect ordering of the

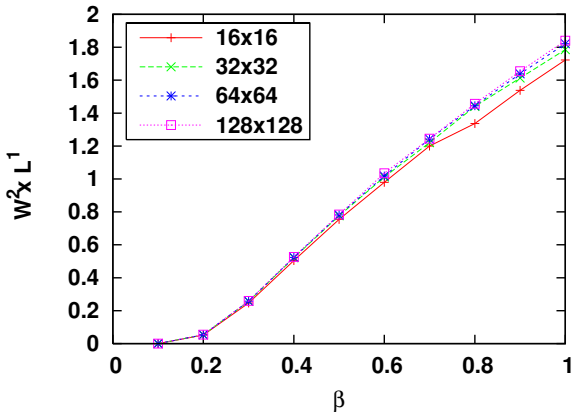

Figure 3.8: Raw data of Fig. 3.7 for the mean square winding scaled by the lattice size in the constrained case. The intersection of the curves should determine β_c. Instead, we have complete data collapse.

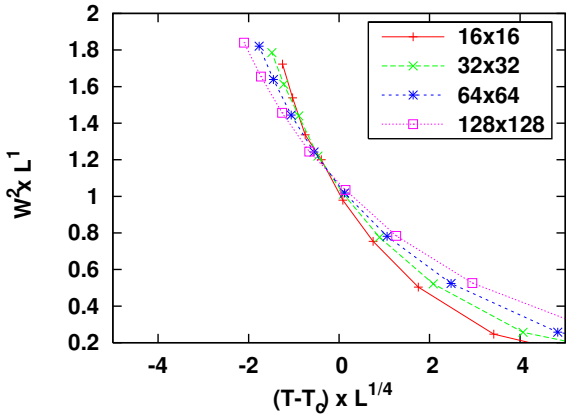

Figure 3.9: Reversing the procedure: "Uncollapsing" data to get critical point.

vacancies/particles in a "checkerboard" pattern.

3.4.1 Half-filling: $\langle\rho\rangle = \frac{1}{2}$

How does the introduction of vacancies affect $\beta_c^{\rm sf}$ in the absence of interactions, $V = 0$? (Henceforth in this manuscript we will append a superscript 'sf' to β_c for the superfluid transition, to distinguish it from the $\beta_c^{\rm cdw}$ for charge ordering. See below.) Figs. 3.11 and 3.12 are the analogs of Figs. 3.3 and 3.4, and show the unscaled and scaled winding as a function of β. As before, we have done simulations for lattices of different sizes to perform

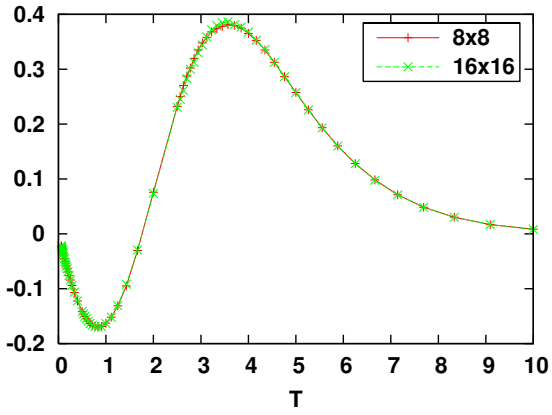

Figure 3.10: Plot of specific heat for a model with local constraints. Note: part of the plot is negative.

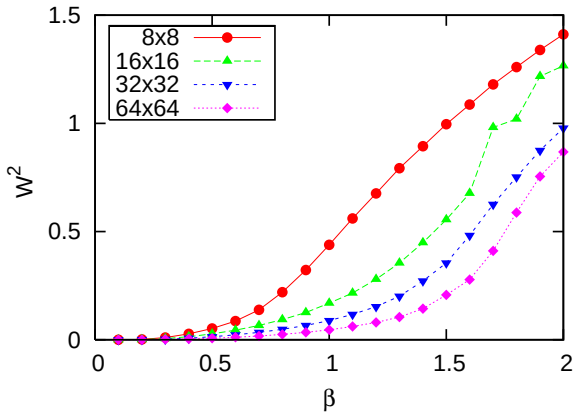

Figure 3.11: Raw data for $\langle W^2 \rangle$ for the extended FK model with half-filling and $V = 0$.

the finite size scaling. The crossing occurs at $\beta_c^{\rm sf} = 1.50 \pm 0.02$. By repeating this sweep of β for different V, we can compute the superfluid phase boundary $\beta_c^{\rm sf}(V)$ in the $V - \beta$ plane at half-filling. This is shown in Fig. 3.15.

A natural question to ask is whether E_v induces vacancy/density ordering. We define the real space density correlation function,

$$c(\mathbf{r}, \mathbf{r}') \;=\; \langle\, (\rho(\mathbf{r}) - \langle\rho\rangle)\,\big(\rho(\mathbf{r}') - \langle\rho\rangle\big)\,\rangle \;, \tag{3.13}$$

where the density $\rho(\mathbf{r}_i) = 1$ if the site i is occupied and is zero otherwise. The structure

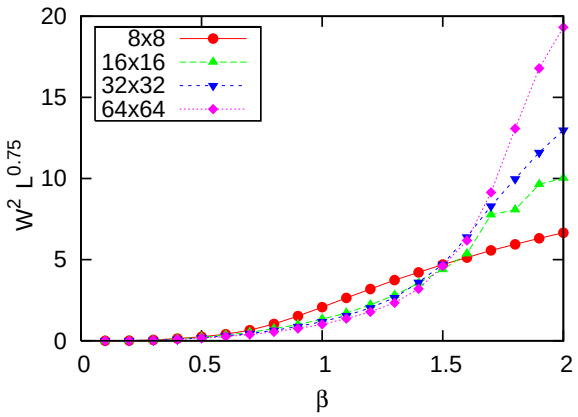

Figure 3.12: Data of Fig. 3.11, scaled. We infer $\beta_c^{\rm sf} = 1.50 \pm 0.02$.

function,

$$S(\mathbf{q}) = \frac{1}{N} \sum_{\mathbf{r},\mathbf{r}'} e^{i\mathbf{q}\cdot(\mathbf{r}-\mathbf{r}')} c(\mathbf{r},\mathbf{r}') \ , \tag{3.14}$$

is the Fourier transform of the density correlations. Here N is number of sites. At half-filling, the ordering vector $\mathbf{q} = (\pi, \pi)$. In a disordered phase where $c(\mathbf{r}, \mathbf{r}')$ decays exponentially with $|\mathbf{r} - \mathbf{r}'|$, $S(\mathbf{q})$ will vanish in the thermodynamic limit (proportional to $1/N$). In an ordered phase, $S(\mathbf{q})$ will go to a constant as the system size increases, for the appropriate ordering wave vector $\mathbf{q}$.

Proceeding in analogy with the winding $\langle W^2 \rangle$, we measure $S(\pi, \pi)$ for different lattice sizes and do finite size scaling to determine $\beta_c^{\rm cdw}$ for the CDW transition. Representative plots, for $V = 2.5$, are shown in Figs. 3.13 and 3.14. Putting together such sweeps for different interaction strengths V yields the density order-disorder (CDW) phase boundary in the $\beta - V$ plane at half-filling shown in Fig. 3.15.

In fact, a number of aspects of the phase diagram of Fig. 3.15 can be inferred by a mapping to the Ising model. We note that the interaction energy E_v of Eq. 3.6 maps precisely to that of the Ising model (the well-known equivalence of lattice-gas and Ising models) with the definition of the spin $S_i^z = 2(\rho(\mathbf{r}_i) - \frac{1}{2})$. The alternating occupied and empty site pattern caused by the repulsive particle-particle interaction ($V > 0$) corresponds

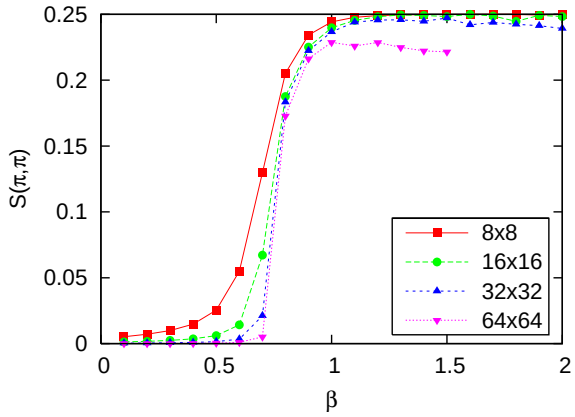

Figure 3.13: The structure factor $S(\pi, \pi)$ is shown as a function of β at half-filling and $V = 2.5$.

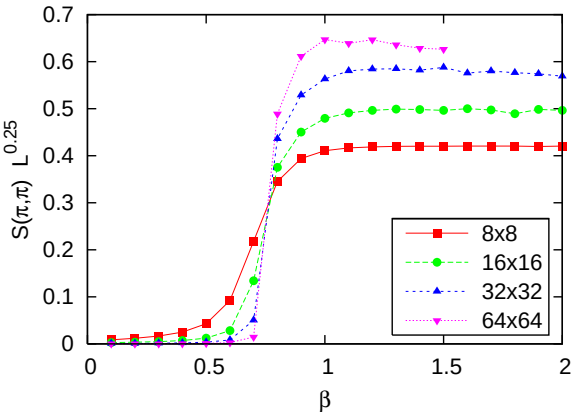

Figure 3.14: Scaled data of Fig. 3.13. The crossing point defines $\beta_c^{\rm cdw}$ for CDW ordering. The scaling exponent multiplying S on the vertical axis is that of the $d = 2$ Ising model, as discussed in the text.

to an antiferromagnetic arrangement in spin language. The quantity $V/4$ plays the role of the exchange constant J. The critical temperature of the Ising model given by the Onsager solution $T_c = 2.269J$ then implies a density ordering $\beta_c^{\rm cdw} = 4/(2.269\,V) = 1.763/V$. We expect this result to be accurate for large β, when E_v dominates over any effects on the site densities which might be caused by the exchange term (which has β in denominator in partition function). This curve is shown as the dotted line in Fig. 3.15.

We can also make a qualitative argument for how the phase boundary might bend away from this Ising limit as the role of β becomes larger. For any given density arrangement,

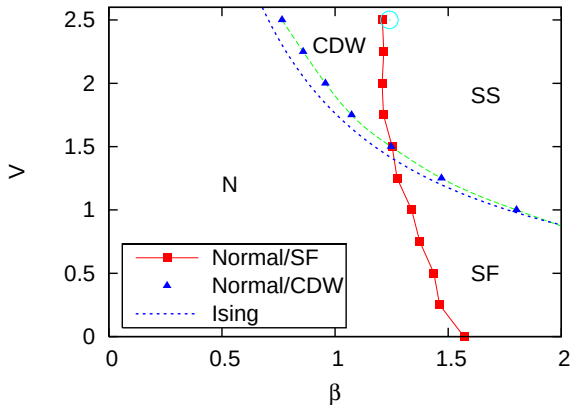

Figure 3.15: The central result of our paper: Phase diagram of the extended Feynman-Kikuchi model in the $V - \beta$ plane at half-filling. Squares denote simulation results for the superfluid transition, and triangles the CDW transition. The CDW boundary is in good correspondence with the Ising limit $\beta_c^{\mathrm{cdw}} = 4/(2.269\,V)$, indicated by the dotted line. The circle at $V = 2.5$ is the prediction $\beta_c^{\mathrm{sf}}(\rho) = \beta_c^{\mathrm{sf}}(\rho = 1)/\rho$. See text for details. In the right upper corner we observe supersolid phase - the simultaneous presence of both superfluidity and long range density correlations.

the exchange of particles provides additional configurations of the system associated with permutations of the particle indices. Such configurations have lower energy when the occupied sites are adjacent. Thus we expect that the exchange term will favor "ferromagnetic" spin configurations, in competition with the "antiferromagnetism" driven by E_v. This suggests a lowering of the CDW transition temperature. Just such an increase in β_c^{cdw} is seen in the phase diagram. One may well ask whether there is an extreme limit where the attraction between particles due to the greater ease of exchange becomes so dominant that phase separation occurs (ferromagnetic clusters in spin language). We will address this possibililty later.

The corresponding effect of V on the superfluid phase transition is less easy to describe rigorously, in part because we do not begin from a known limit like the Onsager solution in the density transition case. On the one hand, increasing V drives the particles apart, making local exchange more expensive, suggesting that β_c^{sf} might increase. On the other hand, the superfluid transition is not caused by local exchange but instead by global winding, and by separating the particles, V might help provide regularly spaced "stepping

stones," aiding global winding and decreasing $\beta_c^{\rm sf}$. While these qualitative arguments provide different conclusions, numerically, the answer is clear from Fig. 3.15: turning on V decreases $\beta_c^{\rm sf}$. The effect is not large, however.

In the limit of large V and half-filling, a perfect CDW phase forms, which corresponds to a completely filled square lattice with a lattice constant $\sqrt{2}$ larger than the original lattice (and rotated by 45 degrees). The squared distances in the FK exchange energy will be scaled up by a factor of two, and hence $\beta_c^{\rm sf}$ will be twice the value for the no-vacancy FK model of the previous section. Thus $\beta_c^{\rm sf} = 2\,(0.62 \pm 0.01)$. This value is shown as the circle at $V = 2.5$ in Fig. 3.15.

In order to develop a simple understanding of $\beta_c^{\rm sf}$ for general V, we consider a small (four site, two particle) cluster and enumerate completely the allowed configurations. There are six possible density configurations, which separate into two classes. Four of them have the two particles adjacent, while the other two have the two particles separated by vacancies:

Configuration	K energy	P energy	Weight
$\bullet - \bullet - \circ - \circ$	$1/2 + 9/2$	V	$4\,e^{-\left(\frac{5}{\beta}+V\beta\right)}$
$\bullet - \circ - \bullet - \circ$	$4/2 + 4/2$	0	$2\,e^{-\left(\frac{4}{\beta}\right)}$

We have included the degeneracy factors in the weight. For each density configuration, there are two permutations. Since we are interested in the superfluid transition, we will restrict ourselves to the case where the two particles do exchange, which is reflected in the nonzero value of the kinetic energy in the table above.

The expectation value of the Kinetic energy is

$$\begin{aligned} \langle K \rangle &= \frac{2 \cdot 5 e^{-\left(\frac{5}{\beta}+V\beta\right)} + 4 e^{-\left(\frac{4}{\beta}\right)}}{2 e^{-\left(\frac{5}{\beta}+V\beta\right)} + e^{-\left(\frac{4}{\beta}\right)}} \\ &= 4 + \frac{2}{2 + e^{\left(\frac{1}{\beta}+V\beta\right)}} \end{aligned} \tag{3.15}$$

Note that $\langle K \rangle = 4$ is kinetic energy at $V \to \infty$. The superfluid transition occurs when $K \sim \beta$. If we set $\langle K \rangle = \beta_c^{\rm sf}$ and use $\langle K(V \to \infty) \rangle = 4 = \beta_c^{\rm sf}(V \to \infty)$ we find that the shift in the superfluid transition is given by,

$$\frac{\Delta\beta_c}{\beta_c(V \to \infty)} = \frac{1}{2} \cdot \frac{1}{2 + e^{\left(\frac{1}{\beta} + V\beta\right)}} \tag{3.16}$$

This result is qualitatively correct at $V = 0$, predicting a small positive shift in $\beta_c^{\rm sf}$ relative to $V \to \infty$).

Our phase diagram (Fig. 3.15) has a supersolid phase in the right upper corner. How relevant is this result to experiments? According to Mahan [55] at $T = 1\ KE = 15K$, which in a Hubbard model makes $t = 15/12 = 1.25K$, and at $T_c = 2.17K\ T/t \approx 1.7$, $V \approx 10K$, $V/t \approx 8$. Kim and Chan observe supersolidity at $T \approx 0.2K$. In our phase diagram, this point lies within the supersolid phase, to the right and up of its borders. We should take into account the difference in our model being at half-filling.

3.4.2 Doped system $\langle \rho \rangle \neq \frac{1}{2}$

In this section we consider general filling ρ. Specifically, in Fig. 3.16 we exhibit the phase diagram in the $\beta - \rho$ plane for two fixed values of the interaction, $V = 1.25$ and $V = 2.50$. Fig. 3.16 was obtained using the same analysis as in the earlier sections: Evaluation and scaling of the winding and structure factor as a function of β for different V and ρ. Several features are immediately apparent from the phase diagram: Charge ordering is, as expected, favored close to half-filling, with the highest transition temperature at $\rho = 1/2$. We have also measured the structure factor $S(\mathbf{q})$ for other $\mathbf{q}$ to see whether doping introduces order at incommensurate wavevectors. The peak in $S(\mathbf{q})$ remains at $\mathbf{q} = (\pi, \pi)$ even when the system is doped.

Interestingly, the shape and size of the density ordered region around half-filling is in rough agreement with the boundaries obtained for checkerboard solid order in the extended boson-Hubbard model [56, 57] where similar superfluid and charge ordered phases are

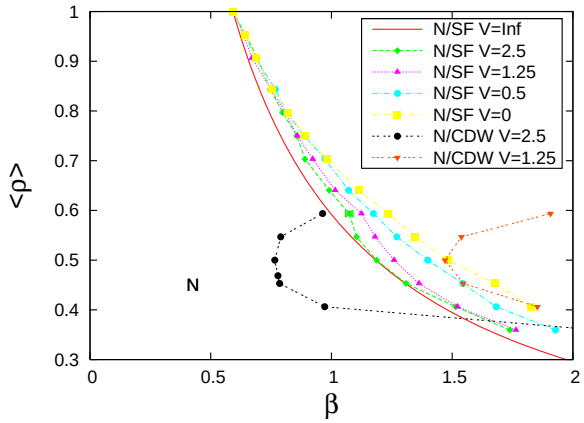

Figure 3.16: Phase diagram in the $\rho - \beta$ plane for the extended FK model for different values of V. Triangles: the numerically obtained cdw transitions. Squares: the numerically obtained superfluid transitions. The superfluid phase boundary is reasonably well approximated by $\beta_c^{\rm sf} \propto 1/\rho$ (solid curve). See text.

present in an explicitly quantum model.

In the preceding section we argued that $\beta_c^{\rm sf}$ for half-filling and $V = \infty$ should be a factor of two larger than for the original, no vacancy FK model, and showed this was borne out numerically. One might expect that a similar result would be true for general fillings and that $\beta_c^{\rm sf}$ would be increased by a factor of $1/\rho$, since this factor reflects the increase in the square of the average interparticle spacing.

$$\beta_c^{\rm sf}(\rho, V \to \infty) = \frac{1}{\rho}\beta_c^{\rm sf}(\rho = 1) \tag{3.17}$$

However, on further consideration, it is not quite so. Half-filling and $V = \infty$ is a special case and in general the particles are not dispersed uniformly, that is, they no longer all have the same distance from their nearest neighbors. Nevertheless, this relation provides a reasonable guide to the density dependence of the superfluid transition, and is shown on phase diagram at Fig. 3.16 as the line "$N/SF\ V = \text{Inf}$".

For the CDW transition we use semi-empirical formula

$$\left(\rho - \frac{1}{2}\right)^2 + \frac{(K/V)^2}{\beta^2} \;=\; C^2.$$

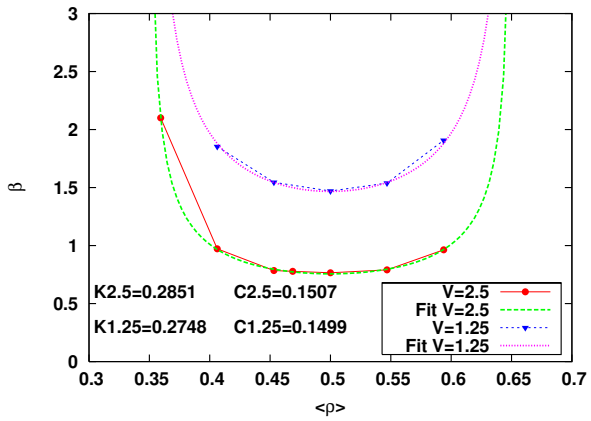

Figure 3.17: Fitting CDW transition from Fig. 3.16. K and C practically don't depend on V.

Fitting our plots into this formula is presented on Fig. 3.17. As can be seen, K and C don't depend considerably on V and at first approximation we may consider them to be constants, $K \approx 0.28$, $C \approx 0.15$. It follows that CDW can only exist when $\left|\rho - \frac{1}{2}\right| < C$.

In Fig. 3.16 we also see that as β is increased at $\rho = 1/2$ and fixed $V = 1.25$, we go from normal to superfluid to supersolid, where the phases are labeled by the behavior of the two order parameters, $\langle W^2 \rangle$ and $S(\pi, \pi)$. Likewise at larger $V = 2.50$ we go from normal to CDW to supersolid.

While the order parameters provide unambiguous identification of the phases, it is also interesting to see if the thermodynamics can pick up the two successive transitions in the form of separate peaks in the specific heat. To study $C(T)$, we proceed similarly to the derivation for the partition function with only the kinetic energy term. Now our partition

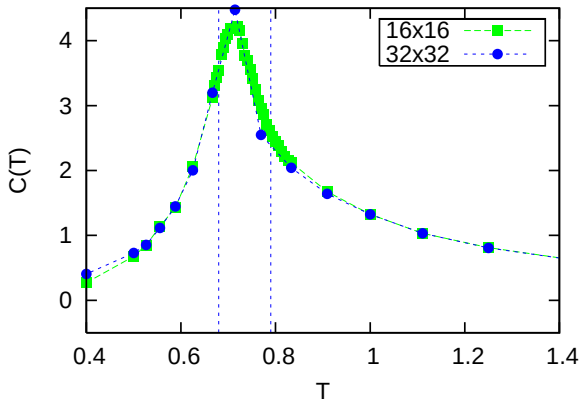

Figure 3.18: Specific heat for half-filling, $V = 1.25$. From Fig. 3.16, the SF transition is at $T = 0.79$, and the CDW transition at $T = 0.68$. These values are shown as vertical dashed lines. The specific heat cannot resolve the two peaks.

function has both potential and kinetic energy.

$$\begin{aligned} Z &= \sum_n e^{-P\beta-\frac{K}{\beta}} \\ E &= -\frac{\partial \ln Z}{\partial \beta} = \frac{\sum_n \left(P-\frac{K}{\beta^2}\right) e^{-P\beta-\frac{K}{\beta}}}{Z_0} \\ C &= \frac{\partial E}{\partial T} = \frac{\partial E}{\partial (1/\beta)} \\ &= -\left(\langle P\rangle\beta - \frac{\langle K\rangle}{\beta}\right)^2 \\ &+ \left\langle \left(P\beta - \frac{K}{\beta}\right)^2 \right\rangle - \frac{\langle K\rangle}{\beta} \end{aligned} \tag{3.18}$$

Fig. 3.18 shows the specific heat as a function of temperature for half-filling and interaction $V = 1.25$. According to the phase diagram Fig. 3.16, the two transition points are N/SF at $\beta = 1.26$ ($T = 0.79$) and N/CDW at $\beta = 1.47$ ($T = 0.68$). As can be seen, we cannot resolve separate peaks in $C(T)$ associated with these transitions. It is likely that the critical temperatures are too close and that the finite size rounding blurs the two peaks into a single maximum.

We can however exhibit separate SF and CDW peaks in the specific heat if we push

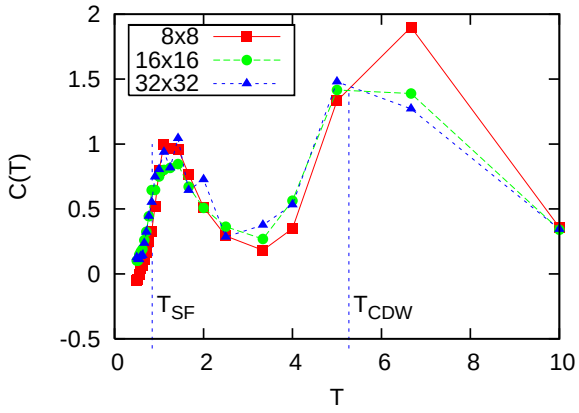

Figure 3.19: Specific heat for half-filling and $V = 10$. Two peaks corresponding to SF and CDW transitions are clearly seen. The critical values given by the winding and structure factor are shown as vertical dashed lines. The Ising mapping would give $T_{CDW} = 5.67$.

the transitions apart sufficiently. For example, at $V = 10$ the CDW transition occurs at a much higher temperature than the SF transition. Indeed, in Fig. 3.19 we can now observe separate signatures of the two transitions in $C(T)$. The maxima occur close to the transition points given by the order parameters.

Our final results concern the possibility of phase separation. One might argue that in a model with vacancies, especially at low or vanishing V, the particles will clump together in order to facilitate exchange. Indeed, phase separation has been observed in a related model: the Bose-Hubbard Hamiltonian with ring exchange, precisely due to this mechanism [58].

Phase separation is signalled by a peak in the density structure factor at small momenta $\mathbf{q}$ (as opposed to the CDW ordering vector at the largest $\mathbf{q} = (\pi, \pi)$). Crudely speaking there are real space density fluctuations at long wavelengths, corresponding to a lattice with one side half occupied and the other half empty. These translate into a peak in $S(\mathbf{q})$ at small $\mathbf{q}$. Note that in a canonical ensemble simulation such as is performed here we cannot set $\mathbf{q} = (0, 0)$ since that value of the structure factor is just a constant set by the filling. Indeed with our definition of the density correlations in terms of fluctuations about the average density per site, Eq. 3.14, $S(0, 0) = 0$.

For a perfectly phase separated state with all particles on the right-most half of the

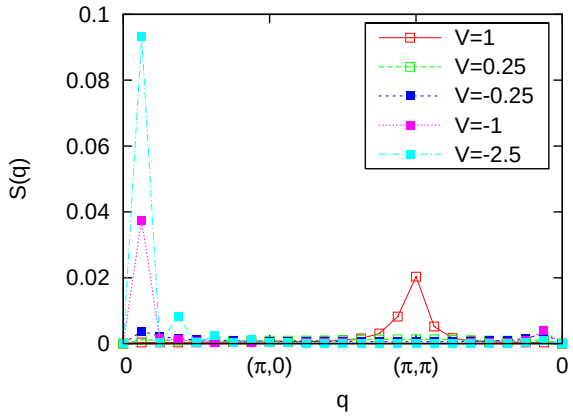

Figure 3.20: $S(\vec{q})$ for various V, $L = 16$, $\beta = 1.5$. $S(2\pi/L, 0)$ should signal phase separation if it is $\sim$ 0.1. It is however not close to that number for $V > 0$. For comparison, plots for $V < 0$ are given, and they indicate phase separation.

lattice we find $S(2\pi/L, 0) \approx 0.11$ for $L = 16$. In Fig. 3.20 we see that $S(2\pi/L, 0)$ is $\sim$ 1/100 of that figure for $V > 0$. We conclude there is no phase separation in this model. The absence of a signal for phase separation is in contrast to the behavior in the related Bose-Hubbard model with ring exchange [58, 59] There the same quantity, the average of the structure factors at the three lowest momenta shows a sharp rise with increased exchange, as one enters the superfluid phase.

3.5 Conclusions

In this paper we have presented Monte Carlo simulations of the phase diagram of an extension of the $d = 2$ Feynman-Kikuchi model which includes vacancies. We found phases which have density and superfluid order, and where these two types of order coexist. Unlike the boson-Hubbard model where supersolid order requires doping away from half-filling in the extended FK model ρ_s is nonzero even in the defect-free checkerboard solid. The reason is that the boson-Hubbard kinetic energy moves particles only between near-neighbor sites. Bosons cannot exchange without passing through an energetically unfavorable region. But in the FK model, exchange at longer range can occur without ever 'passing through' the rare configurations with near-neighbor sites that are occupied. One might expect that

in the FK model which is restricted to local exchange, the half-filled supersolid might be eliminated.

A further problem of interest in the extended FK is to consider "quenched" vacancies in which the locations of the empty sites are frozen throughout the simulation. Here again we might expect that when a restriction to local exchange is enforced, there could be a destruction of the superfluid transition as the percolation threshold is crossed. In the model allowing exchanges of arbitrary distance, one expects a more trivial increase in β_c, but that the superfluid transition would likely persist.

A final avenue for exploration would be the inclusion of a one-body vacancy potential which could be chosen to confine the particles preferentially towards the center of the lattice. Such simulations would connect with recent experiments on cold atoms in magnetic and laser traps.

We acknowledge support from the National Science Foundation under award NSF ITR 0313390, and useful input from T.Tremeloes.

Chapter 4

Superfluid and Mott Insulator Phases of one dimensional Bose-Fermi Mixtures

The contents of this chapter first appeared in Physical Review A 78, 033619 (2008). It is a collaborative work with Andrew Baldwin, Richard Scalettar, Valery Rousseau, Peter Denteneer and Marcos Rigol. For simulations software written by Valery Roussesu and Peter Denteneer was used.

We study the ground state phases of Bose-Fermi mixtures in one-dimensional optical lattices with quantum Monte Carlo simulations using the Canonical Worm algorithm. Depending on the filling of bosons and fermions, and the on-site intra- and inter-species interaction, different kinds of incompressible and superfluid phases appear. On the compressible side, correlations between bosons and fermions can lead to a distinctive behavior of the bosonic superfluid density and the fermionic stiffness, as well as of the equal-time Green functions, which allow one to identify regions where the two species exhibit anti-correlated flow. We present here complete phase diagrams for these systems at different

fillings and as a function of the interaction parameters.

4.1 Introduction

The experimental realization of strongly correlated systems with ultracold gases loaded in optical lattices [61] has generated tremendous excitement during recent years. Initially thought of as a way to simulate condensed matter model Hamiltonians, like the Bose-Hubbard Hamiltonian [38], loading atoms on optical lattices has enabled the creation of quantum systems that are unexpected in the condensed matter context. Among these systems the realization of Bose-Fermi mixtures in optical lattices [62, 63, 64], where the inter- and intra-species interactions can be tuned to be attractive or repulsive [65], is a remarkable example of the scope of realizable models.

Theoretical studies of Bose-Fermi mixtures in one-dimensional lattices have been done for homogeneous [66, 20, 67, 68, 69, 70, 71, 72] and trapped [73, 74, 75] systems. Several approaches have been used: Gutzwiller mean-field theory [73], strong coupling expansions [20, 72], bosonization [66, 67] and exact analytical [68] and numerical [69, 70, 71, 75, 72] studies. Recently, a mixture of bosonic atoms and molecules on a lattice was studied numerically [76]. The landscape of phases encountered is expansive, and includes Mott insulators, spin and charge density waves, a variety of superfluids, phase separation, and Wigner crystals. However, the phase diagram in the chemical potential-interaction strength plane has not yet been reported.

It is our goal in this paper to present a study of repulsive Bose-Fermi mixtures in one-dimensional lattices that generalizes previous studies, which focused on specific special densities, to more general filling. After mapping the phase diagram we will explore different sections in greater detail. Since the particular case in which the lattice is half filled with bosons and half filled with fermions has been carefully studied in Ref. [69], we will instead concentrate here on two cases: (i) when the number of bosons is commensurate with the lattice size but the number of fermions is not, and (ii) when the sum of both species is

commensurate with the lattice size but the number of bosons and fermions are different. Some of the phases present in these cases have been identified by Sengupta and Pryadko in their grand canonical study in Ref. [70] and by Hébert *et al.* in the canonical study recently presented in Ref. [71].

The Hamiltonian of Bose-Fermi mixtures in one dimension can be written as

$$\begin{aligned} \hat{H} = & - t_B \sum_l (b_{l+1}^\dagger b_l + b_l^\dagger b_{l+1}) \\ & - t_F \sum_l (f_{l+1}^\dagger f_l + f_l^\dagger f_{l+1}) \\ & + U_{BB} \sum_l \hat{n}_l^B (\hat{n}_l^B - 1) + U_{BF} \sum_l \hat{n}_l^B \hat{n}_l^F \end{aligned} \tag{4.1}$$

where $b_l^\dagger (b_l)$ are the boson creation (destruction) operators on site l of the one-dimensional lattice with L sites. Similarly, $f_l^\dagger (f_l)$ are the creation (destruction) operators on site l for spinless fermions on the same lattice. For these creation and destruction operators $\hat{n}_l^{B,F}$ are the associated number operators. The bosonic and fermionic hopping parameters are denoted by t_B and t_F respectively, and the on-site boson-boson and boson-fermion interactions by U_{BB} and U_{BF}. In this paper we will consider the case $t_B = t_F = 1$ (i.e. when the boson and fermion hopping integrals are equal) and choose $t_B = 1$ to set the scale of energy.

It is useful to begin a discussion of the phase diagram with an analysis of the zero hopping limit ($t_B = t_F = 0$) similar to the one done by Fisher *et al.* in Ref. [37] for the purely bosonic case. Consider a particular fermion occupation of one fourth of the lattice sites, $N_F = L/4$ fixed. Bosons can be added up to $N_B = 3L/4$ without sitting on a site which is already occupied by either a boson or a fermion. Therefore the associated chemical potential μ is small. What happens when N_B exceeds $3L/4$ depends on the relative strength of U_{BB} and U_{BF}.

If U_{BF} is less than $2U_{BB}$ then the extra bosons sit atop of the fermions and μ jumps by U_{BF}. The chemical potential stays at this elevated value of U_{BF} until all the sites with

fermions also have a boson. At that point additional bosons start going onto sites with a boson already, and μ jumps to $2U_{BB}$. Thus in general there are incompressible phases where the boson chemical potential jumps both at commensurate $\rho_B = 1,\ 2,\ 3, ...$ (as for the pure boson-Hubbard model) and also at $\rho_B = 1 - \rho_F,\ 2 - \rho_F,\ 3 - \rho_F, \cdots$. For U_{BF} greater than $2U_{BB}$ and less than $6U_{BB}$ the incompressible phases still start at $\rho_B = 1 - \rho_F$ but the following potential jumps are shifted up by $1 - \rho_F$. Turning on the hoppings t_B, t_F introduces quantum fluctuations which will ultimately destroy these Mott plateaus and introduce new, intricate phases.

4.2 Canonical Worm Algorithm

We perform Quantum Monte Carlo simulations (QMC) using a recently proposed Canonical Worm algorithm [77, 78]. This approach makes use of global moves to update the configurations, samples the winding number, and gives access to the measurement of n-body Green functions. It also has the useful property of working in the *canonical* ensemble. This is particularly important for the present application since working with two species of particles leads to two different chemical potentials in the grand canonical ensemble. These prove difficult to adjust such that the precise, desired fillings are achieved. In our canonical simulations the Bose and Fermi occupations are exactly specified and the chemical potentials μ_B and μ_F are instead computed [79] via appropriate numerical derivatives of the resultant ground state energy (e.g. $\mu_B = E_0(N_B + 1) - E_0(N_B)$).

The Canonical Worm algorithm is a variation of the Prokof'ev *et al.* grand-canonical worm algorithm [80]. Within the Canonical Worm approach one starts by writing the Hamiltonian as $\hat{H} = \hat{V} - \hat{T}$, where $\hat{T}$ is comprised of the non-diagonal terms and is by necessity positive definite. The partition function $\mathcal{Z} = \mathrm{Tr} e^{-\beta \hat{H}}$ takes the form

$$\mathcal{Z} = \mathrm{Tr}\ e^{-\beta \hat{V}} \mathbf{T}_\tau e^{\int_0^\beta \hat{T}(\tau) d\tau} \tag{4.2}$$

$$= \mathrm{Tr}\ e^{-\beta \hat{V}} \sum_n \int_{0<\tau_1<\cdots<\tau_n<\beta} \hat{T}(\tau_n) \cdots \hat{T}(\tau_1) d\tau_1 \cdots d\tau_n \tag{4.3}$$

where $\hat{T}(\tau) = e^{\tau\hat{V}}\hat{T}e^{-\tau\hat{V}}$. In order to sample expression (4.3) an extended partition function is considered by breaking up the propagator at imaginary time τ and introducing a "worm operator" $\hat{W} = \sum_{ijkl} w_{ijkl} b_i^\dagger b_j f_k^\dagger f_l$ that leads to $\mathcal{Z}(\tau) = \mathrm{Tr} e^{-(\beta-\tau)\hat{H}}\hat{W}e^{-\tau\hat{H}}$. Complete sets of states are introduced between consecutive $\hat{T}$ operators to allow a mapping of the 1D quantum problem onto a 2D classical problem where a standard Monte Carlo technique can be applied. Measurements can be performed when configurations resulting in diagonal matrix elements of $\hat{W}$ occur. This way unphysical movements are exploited to help explore the Hilbert space, but are ignored when sampling for measurements.

As with pure bosonic systems, the evolution of the boson and fermion densities ρ_B, ρ_F with the associated chemical potential μ_B, μ_F identifies Mott insulating behavior [37]. A jump in μ signals a Mott phase where the compressibility $\kappa_B = \partial\rho_B/\partial\mu_B$ or $\kappa_F = \partial\rho_F/\partial\mu_F$ vanishes.

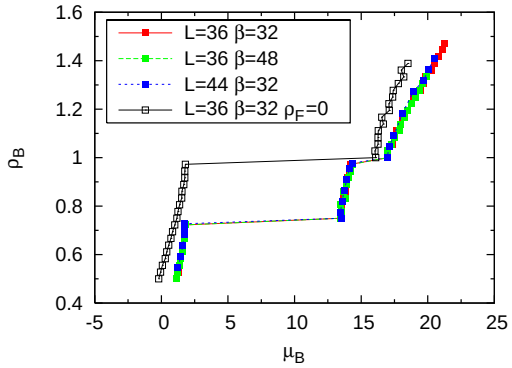

Figure 4.1: ρ_B as a function of chemical potential μ_B. The fermion density is $\rho_F = 1/4$ and the interaction strengths are fixed at $U_{BB} = 10$ and $U_{BF} = 16$. There are Mott plateaus at $\rho_B = 1 - \rho_F = 3/4$ and $\rho_B = 1$ as predicted by the $t_B = t_F = 0$ analysis. The positions of the Mott lobes coincide for different lattice sizes $L = 36, 44$ and temperatures $\beta = 32, 48$ to within our error bars, which are smaller than the symbol size. The dependence of ρ_B on μ_B in the absence of fermions is given for comparison.

Quantities of interest that we measure include the bosonic superfluid density and the

fermionic stiffness,

$$\begin{aligned} \rho_B^{\rm s} &= \langle W_B^2 \rangle L/2\beta \\ \rho_F^{\rm s} &= \langle W_F^2 \rangle L/2\beta \ . \end{aligned} \tag{4.4}$$

Here $\langle W^2 \rangle$ are the associated winding numbers. Correlations between the bosonic and fermionic winding numbers [69] are determined by the combinations,

$$\begin{aligned} \rho_c^{\rm s} &= \left\langle (W_B + W_F)^2 \right\rangle L/2\beta \\ \rho_a^{\rm s} &= \left\langle (W_B - W_F)^2 \right\rangle L/2\beta \ . \end{aligned} \tag{4.5}$$

In addition to the usual bosonic and fermionic Green function,

$$\begin{aligned} G_{ij}^B &= \langle b_i^\dagger b_j \rangle \\ G_{ij}^F &= \left\langle f_i^\dagger f_j \right\rangle \ , \end{aligned} \tag{4.6}$$

we also measure the composite anti-correlated two-body Green function

$$G_{ij}^a = \left\langle b_i^\dagger b_j f_j^\dagger f_i \right\rangle \ . \tag{4.7}$$

In G_{ij}^a, the fermion and boson propagate in opposite directions (one from j to i and one from i to j).

The Fourier transforms of G_{ij}^B and G_{ij}^F give the densities $n_B(k)$ and $n_F(k)$ in momentum space; $n_a(k)$ is the Fourier transform of the composite two-body Green function G_{ij}^a.

We performed extensive checks of the code against other quantum Monte Carlo simulations in the pure boson and pure fermion cases, and against exact diagonalization and Lanczos calculations for mixed systems on small lattices.

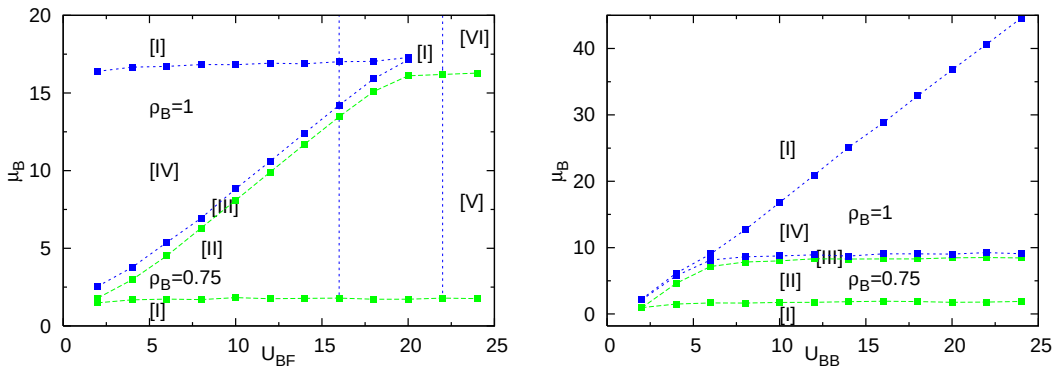

Figure 4.2: Top panel: Phase diagram in the μ_B-U_{BF} plane for $U_{BB} = 10$ and $\rho_F = 1/4$ obtained by a sequence of plots such as that in Fig. 4.1. The vertical line at $U_{BF} = 16$ corresponds to the coupling value in Fig. 4.1. Within the regions labeled $\rho_B = 0.75$ and $\rho_B = 1$, the boson density is frozen even though the chemical potential varies. The $\rho_B = 1$ lobe is pinched off at $U_{BF} \approx 2U_{BB}$. The labeling of the phases is: **I.** Superfluid ($\rho_B^s \neq 0$ $\rho_F^s \neq 0$); **II.** Anti-Correlated phase ($\rho_B^s \neq 0$, $\rho_F^s \neq 0$, $\rho_B^s = \rho_F^s$); **III.** Anti-Correlated phase / Relay Superfluid ($\rho_B^s \neq 0$, $\rho_F^s \neq 0$) (see text for detailed explanation); **IV.** Mott Insulator / Luttinger liquid ($\rho_B^s = 0$, $\rho_F^s \neq 0$); **V.** Insulator, $\rho_B^s = 0$ $\rho_F^s = 0$; **VI.** Phase separation.
Bottom panel: Phase diagram in the μ_B-U_{BB} plane for $U_{BF} = 10$ and $\rho_F = 1/4$. The upper boundary of phase II is defined by the increase of energy when a boson is added at filling $\rho_B + \rho_F = 1$; this is approximately $\mu_B = U_{BF}$ (for $U_{BF} < 2U_{BB}$), a line of slope 1 in the μ_B-U_{BF} plane and slope 0 in the μ_B-U_{BB} plane. A similar strong coupling analysis applies for the other boundaries. (See also Fig. 4.13 and [[20]].)

4.3 Phase Diagram in the μ_B-U_{BF} plane

We begin our determination of the phase diagram by calculating the dependence of the density ρ_B on chemical potential μ_B, mapping out the extent that the Mott plateaus described in the introduction survive the introduction of quantum fluctuations t_B, t_F. We examine a system with a fixed $U_{BB} = 10$ and $\rho_F = 1/4$ and focus on the regions through $\rho_B \leq 3/2$ and $U_{BF} \leq 5U_{BB}/2$ in the phase diagram. The $t_B = t_F = 0$ analysis suggests for $U_{BF} < 2U_{BB}$ there will be plateaus with compressibility $\kappa = 0$ at $\rho_B + \rho_F = 1$ (i.e. $\rho_B = 3/4$) caused by U_{BF} and at $\rho_B = 1$ caused by U_{BB}. Fig. 4.1 exhibits these plateaus for $U_{BF} = 16$ and $t_B = t_F = 1$. The complete phase diagram in the μ_B-U_{BF} plane at fixed $U_{BB} = 10$ is obtained by replicating Fig. 4.1 for different U_{BF}, and is given in

Fig. 4.2a. For weak U_{BF} the phase diagram is dominated by the $\rho_B = 1$ plateau where the chemical potential jumps by $2U_{BB} - U_{BF} \approx 2U_{BB} = 20$. As U_{BF} increases, this plateau shrinks and finally terminates at $U_{BF} \approx 2U_{BB} = 20$. At the same time, the plateau at $\rho_B = 1 - \rho_F$ grows to $U_{BF} = 20$. The explanation of the labeling of the different phases (**I-VI**) will be given after we discuss the superfluid response of the system. Fig. 4.2b shows the phase diagram in the μ_B and U_{BB} plane.

4.4 Superfluid Response at $\rho_B + \rho_F = 1$

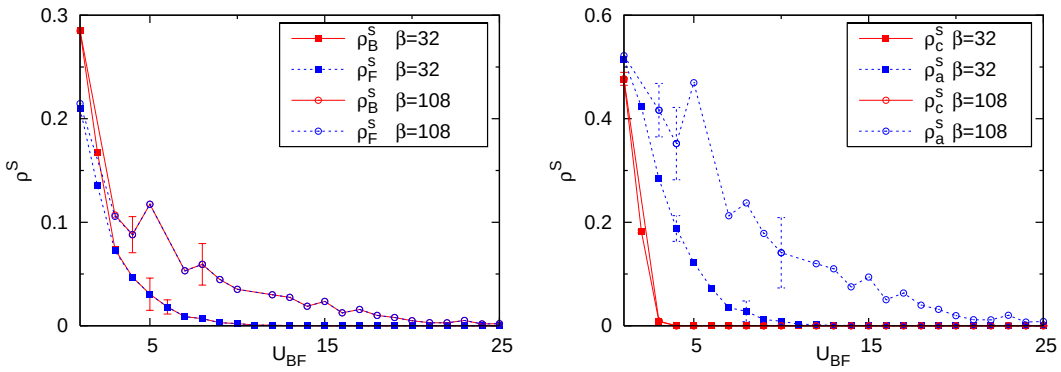

Figure 4.3: "Horizontal" sweep, that is fixed densities $\rho_B = 3/4$ and $\rho_F = 1/4$ and varying U_{BF}, through the phase diagram of Fig. 4.2. As in Figs. 4.1 and 4.2, $U_{BB} = 10$. Top panel: Both the bosonic and fermionic species exhibit a finite stiffness at weak coupling (region **II** of phase diagram), which decays as U_{BF} increases until insulating behavior occurs (region **V** of phase diagram). Bottom panel: Near $U_{BF} = 0$ both $\rho_c^s \neq 0$ and $\rho_a^s \neq 0$ are very similar. However, quickly after turning on U_{BF}, the correlated and anti-correlated stiffness show that the bosons and fermions propagate in opposite directions $\rho_a^s \neq 0$, while $\rho_c^s = 0$.

After determining the positions of the Mott plateaus, we examine the stiffness and Green functions. We take a "horizontal" cut through Fig. 4.2a by fixing $\rho_B + \rho_F = 1$ ($\rho_B = 3/4$) and increasing U_{BF}. In Fig. 4.3 we see that for $U_{BF} \lesssim 2U_{BB} = 20$ the interaction strength U_{BF} is small enough that fermions and bosons can briefly inhabit the same site. Now, when a boson visits the site of a neighboring fermion (or vice versa) it is equally likely that the fermion will exchange as for the boson to return to its original site.

Through these exchanges the bosons and fermions can achieve anti-correlated winding around the lattice. Thus, the bosonic superfluid density and the fermionic stiffness are both non-zero and identical [1]. However, as U_{BF} increases past $U_{BF} \approx 2U_{BB} = 20$ the cost of double occupancy becomes prohibitive. With its benefits outweighed by energy penalties exacted by U_{BF}, all anti-correlated "superfluidity" ceases. Pollet *et al.* [69] have argued that this region exhibits phase separation. Indeed we do detect a signal of phase separation through density structure factor. But the signal is weak, about 20 times weaker than what we get at phase **VI** (next section), and compressibility is close to zero, so we label this region as an insulator.

From the results depicted in Fig. 4.3 one should notice that while for quantities like the energy and Mott gap $\beta = 32$ is sufficiently low for $L = 32$ to capture the ground state behavior, for stiffnesses one requires much lower temperatures.

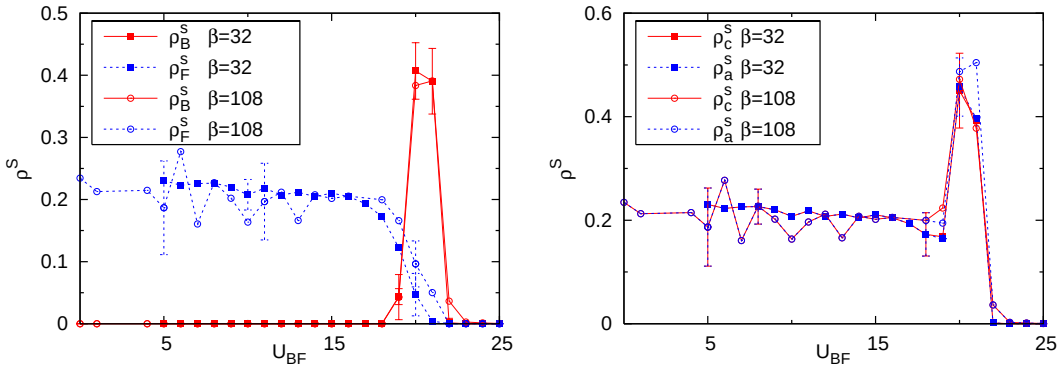

Figure 4.4: Same "horizontal cut" as Fig. 4.3 except at commensurate density for the boson species alone $\rho_B = 1$ and $\rho_F = 1/4$. Top panel: The bosons are insulating at weak U_{BF} within this Mott lobe of commensurate bosonic filling (region **IV** of phase diagram). However the fermions are free to flow on the uniform boson background and have nonzero stiffness. Upon emerging from the lobe, at $U_{BF} \approx 2U_{BB}$, ρ_B^s becomes nonzero in a window where the two repulsions work against each other. After the peak, the system becomes phase separated and ρ_B^s and ρ_F^s go to zero. Bottom panel: The correlated and anti-correlated stiffnesses are essentially equal throughout the weak coupling because the flow is dominated by fermions. However, in the window the anti-correlated stiffness increases beyond the correlated stiffness in a weak simulacrum of phase **II** (as discussed in the text).

[1] This phase has been termed "Super-Mott" as a consequence of its combining a non-zero gap with non-zero superflow [76].

4.5 Superfluid Response at $\rho_B = 1$

Although it shares the property that $\kappa_B = 0$ with the $\rho_B + \rho_F = 1$ lobe, a 'horizontal' cut (Fig. 4) through the $\rho_B = 1$ Mott lobe exhibits rather different superfluid response. This trajectory initially lies within the Mott lobe and then emerges into a region of non-zero compressibilities. As expected, the plateau in ρ_B (Mott gap) indicates the bosons are locked into place by the strong U_{BB}, and as a consequence $\rho_B^{\rm s} = 0$ (Fig. 4.4). Throughout this boson Mott lobe the fermions are, however, free to slide over the bosons and so $\rho_F^{\rm s}$ is non-zero. In this region, as expected, the fermion compressibility κ_F is nonzero.

The Bose-Fermi repulsion U_{BF} competes with U_{BB} and, in a window around $U_{BF} \approx 2U_{BB}$, it is energetically equivalent for a boson to share a site with another boson as with a fermion. The Mott lobe is terminated and a superfluid window opens for both species. Finally, for $U_{BF} > 2U_{BB}$, it is energetically unfavorable for a boson to share a site with a fermion. We enter a region of phase separation where superflow for both species stops, but the compressibilities κ_B and κ_F are nonzero. We also confirm phase separation through a density structure factor. See also [71, 72].

4.6 Superfluid Response At General Filling

Further insight into the physics of this phase diagram can be obtained by measuring the superfluid response along the same 'vertical' cuts through the phase diagram as done in Figs. 4.1 and 4.2, in which ρ_B is varied at fixed U_{BF}. In Figs. 4.5 and 4.6, we show the result. Distinctive densities in the latter figures are $\rho_B = 3/4$ (so that $\rho_B + \rho_F = 1$) and $\rho_B = 1$. We discuss first (Fig. 4.5) the case of $U_{BF} = 16$, where increasing ρ_B cuts through both Mott lobes. The bosonic superfluid density vanishes at $\rho_B = 1$, dips at $\rho_B + \rho_F = 1$, and is nonzero above, below, and between the lobes. The fermion superfluid density is never driven to zero in this cut, and only dips at the special value $\rho_B = 3/4$ where the commensurate total density works against superfluidity. In the case of $U_{BF} = 24$, Fig. 4.6, as ρ_B increases we cut through only the $\rho_B = 3/4$ lobe. Here the superfluid density is

pushed to zero for the entire region between $\rho_B = 3/4$ and $\rho_B = 1$, and is non-zero without.

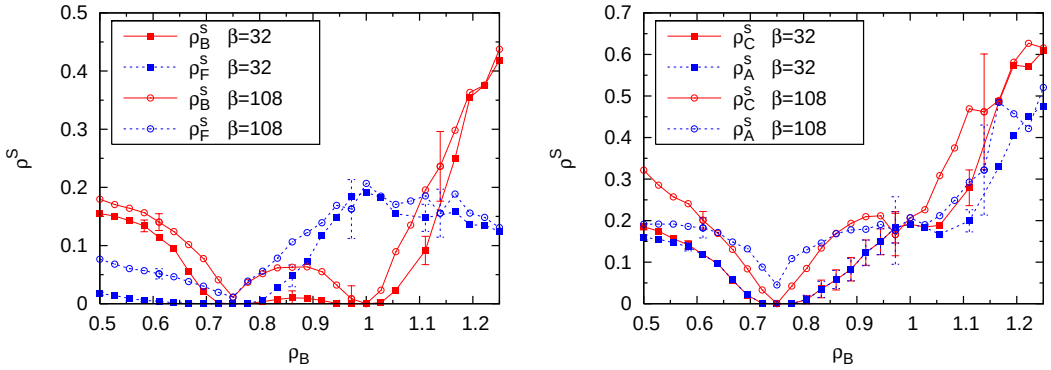

Figure 4.5: "Vertical" sweep across ρ_B at $\rho_F = 1/4$, $U_{BB} = 10$ and $U_{BF} = 16$. Top panel: The boson superfluid density changes much less as β is increased from $\beta = 32$ to $\beta = 108$ in the superfluid phase **I** at $\rho_B < 3/4$ and $\rho_B > 1$ than for phase **III** $3/4 < \rho_B < 1$. This is a hallmark of the "relay" superfluid discussed in the text. Bottom panel: The correlated winding decreases to zero at $\rho_B = 3/4$ while the anti-correlated winding remains finite. As ρ_B is increased beyond $3/4$ the correlated winding increases and overtakes the anti-correlated winding. This is another sign of the "relay" superfluid.

We now fill in the labeling of the phase diagram of Fig. 4.2. A gapless superfluid phase (**I**) with ($\rho_B^s \neq 0$ and $\rho_F^s \neq 0$) exists at low filling of the lattice $\rho_B + \rho_F < 1$. When the combined filling of the two species becomes commensurate, an anti-correlated (**II**) phase appears in which $\rho_B^s \neq 0$ and $\rho_F^s \neq 0$, but $\rho_B^s = \rho_F^s$. This phase is characterized by superflow of the two species in opposite directions and is gapped to the addition of bosons or fermions. The usual bosonic Mott insulator, phase **IV**, occurs at commensurate boson densities. However, it can be melted by increasing U_{BF} since the jump in bosonic chemical potential (Mott gap) is reduced to $2U_{BB} - U_{BF}$. There is no jump in μ_F. Eventually quantum fluctuations break this gap and superflow is allowed. When U_{BF} exceeds $2U_{BB}$, all superflow stops and we enter the insulating region **V** of the phase diagram.

We speculate that the nature of the superfluidity in the narrow phase **III**, which exists between the two Mott lobes is an unusual "relay" process. It is similar to the usual superfluid which exists between Mott lobes in the single species model, in that $\rho_B^s \neq 0$. However, the temperature scale at which superfluid correlations build up is dramatically reduced. This occurs because the bosons can exhibit superflow only by traveling along with

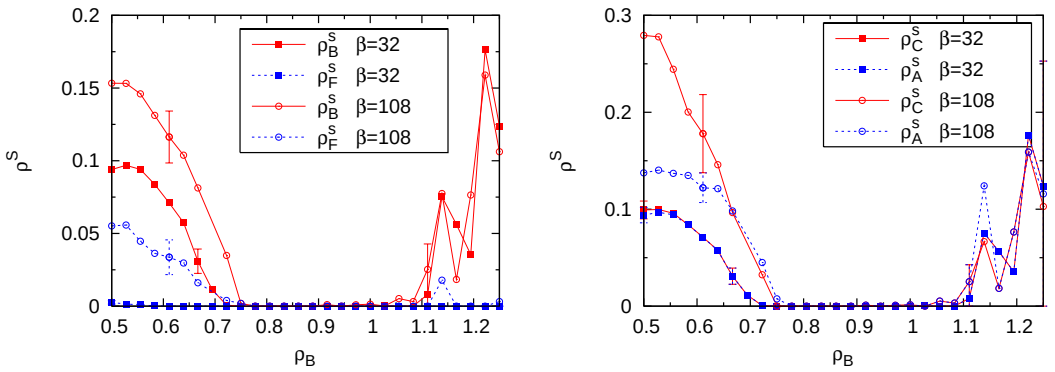

Figure 4.6: "Vertical" sweep across ρ_B at $\rho_F = 1/4$, $U_{BB} = 10$ and $U_{BF} = 24$. Unlike the case for the weaker coupling $U_{BF} = 16$ in Fig. 4.5, both superfluid densities vanish in the insulating region of the Mott lobe at commensurate total filling.

a fermion partner, and being handed off from fermion to fermion in order to wind around the entire lattice. The point is that because $2U_{BB}$ exceeds U_{BF} the bosons doped into the lattice above $\rho_B = 1 - \rho_F = 3/4$ are forced to sit on a fermion. They cannot hop off, but the fermion can move since it has already paid U_{BF} to share a site with a boson. Now, the fermions cannot pass each other once a fermion riding atop bosons runs into a fermion alone on a site. The fermion without a boson cannot move out of the other fermion's way either. However, the boson sharing a site with the mobile fermion can then hop to the immobile fermion at no energy cost. Thus, the boson is passed from one fermion to the other, granting it mobility. Signatures of this phase are the lower value of the temperature at which the superfluid density builds up, that $\rho^{\rm s}_F > \rho^{\rm s}_B$, and more correlated winding than anti-correlated. However, there is nothing preventing lone fermions from acting as in the anti-correlated superfluid phase. Unfortunately this means that potential signals are masked. While we do see some of these signatures (Fig. 4.5) in the specified region, the numbers are not completely conclusive and will require further investigation.

4.7 Momentum distribution functions

To further explore the nature of the phases we turn to the momentum distributions for the bosons, fermions, and anti-correlated pairing - Fig. 4.7 - 4.12. Each plot is made

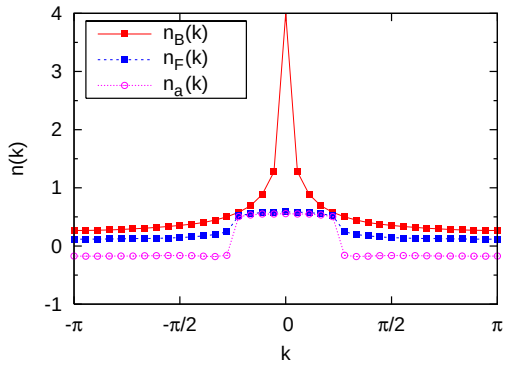

Figure 4.7: **I.** $U_{BF} = 16$, $U_{BB} = 10$, $\beta = 108$ and $N_B = 20$; Momentum distributions for bosons and fermions, and Fourier transform of the anti-correlated pairing ($n_a(k)$) Green function. The sharp peak in bosonic momentum distribution indicates the presence of a quasi-condensate, while fermions have a plateau indicating Luttinger liquid like behavior with a clear Fermi momentum, a property that is also shared by the composite fermions described by the anti-correlated pairing.

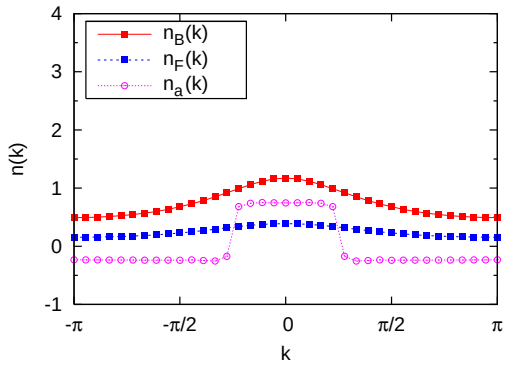

Figure 4.8: **II.** $U_{BF} = 16$, $U_{BB} = 10$, $\beta = 108$ and $N_B = 27$. Bosons do not have a peak at $k = 0$ and the Fermi momentum is washed out, both reflecting the onset of short range one-particle correlations. On the other hand, the plateau in the Fourier transform of the anticorrelated pairing shows that the composite fermions formed by pairing a fermion and a boson have a well defined Fermi momentum [69].

at $\beta = 108$ and correspond to the parameter choices: **I.** $U_{BF} = 16$ and $N_B = 20$; **II.** $U_{BF} = 16$ and $N_B = 27$; **III.** $U_{BF} = 16$ and $N_B = 32$; **IV.** $U_{BF} = 16$ and $N_B = 36$; **V.** $U_{BF} = 30$ and $N_B = 27$; **VI.** $U_{BF} = 28$ and $N_B = 36$. In the superfluid phase (**I.**), there is a peak in the boson distribution and a plateau in the fermion distribution, implying quasi-condensation in the bosonic sector and Luttinger liquid-like behavior in the fermionic one. In the anti-correlated phase (**II.**) there is neither of the former behaviors, but the Fourier

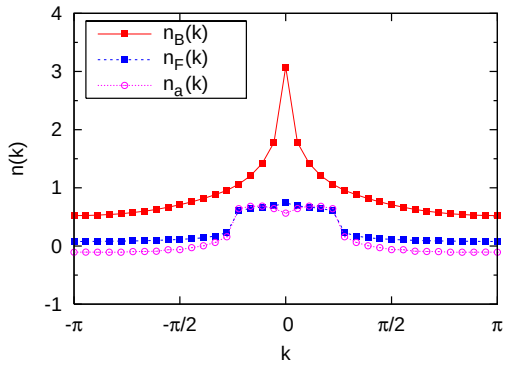

Figure 4.9: **III.** $U_{BF} = 16$, $U_{BB} = 10$, $\beta = 108$ and $N_B = 32$. Qualitatively, this picture is similar to Fig. 4.7 - we have a peak in the bosonic momentum distribution and a plateau in the fermionic and anticorrelated pairing momentum distributions, all indicating power-law decaying correlations of their corresponding real space Green functions.

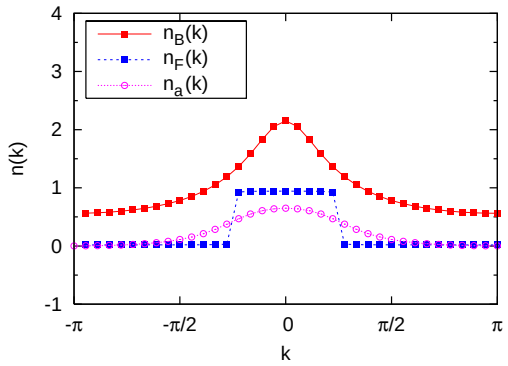

Figure 4.10: **IV.** $U_{BF} = 16$, $U_{BB} = 10$, $\beta = 108$ and $N_B = 36$. There is no sharp peak in $n_B(k)$ and a plateau in $n_F(k)$ is present. This phase is a Mott Insulator for bosons and Luttinger liquid behavior for the fermions. In this case the composite fermions do not exhibit a Fermi momentum.

transform of the anti-correlated pairing Green function has a clear Fermi momentum showing Luttinger-like physics of the composite fermions (formed by pairing a fermions and a boson) [69, 81]. The "relay" superfluid phase (**III.**) displays momentum distributions that are similar to the ones of superfluid phase (**I**). Next, in the Mott insulator / Luttinger liquid phase (**IV.**) one can see a clear Fermi momentum in the bare fermion $n_F(k)$ and a very smooth behavior of $n_B(k)$ and $n_a(k)$, which show that their real space Green function counterparts are decaying exponentially. In the insulating phase (**V.**) all the correlations decay exponentially and their corresponding momentum distribution functions are smooth

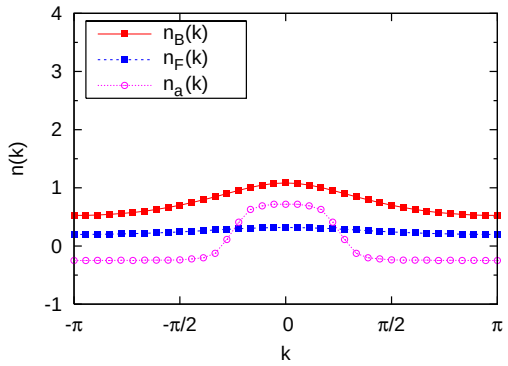

Figure 4.11: **V.** $U_{BF} = 30$, $U_{BB} = 10$, $\beta = 108$ and $N_B = 27$. The momentum distribution functions in this case exhibit the behavior expected from an insulator, i.e., no sharp peak in $n_B(k)$, no plateau in $n_F(k)$, and no Fermi edge in $n_a(k)$.

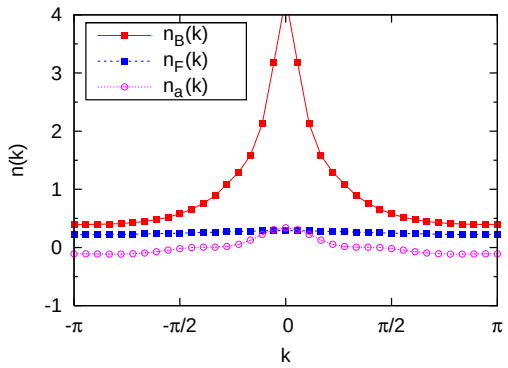

Figure 4.12: **VI.** $U_{BF} = 28$, $U_{BB} = 10$, $\beta = 108$ and $N_B = 36$. Phase separation. The boson momentum distribution function has a peak indicating that there may be a kind of superflow in their separate area. Fermions, on the other hand, behave as an isolator. The $n_a(k)$ curve indicates that the coupling between bosons and fermions is weak, as we would expect in phase separation.

functions of k. In the case of phase separation (**VI.**) the bosonic momentum distribution is similar to the superfluid, while fermionic distribution is insulating.

4.8 Connection to previous theoretical work

As reviewed in the introduction, there is an extensive theoretical literature on Bose-Fermi mixtures. We now make more detailed contact with previous work, first by comparing our results to the strong coupling phase diagram of Lewenstein *et al.* (LSBF) [20]. Fig. 4.13

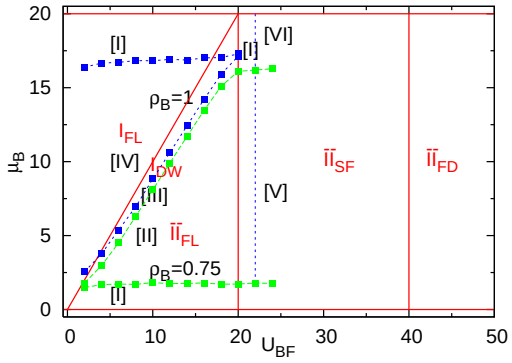

Figure 4.13: A comparison of our phase diagram (Fig. 4.2) with the strong coupling boundaries. Symbols and dashed lines are the results of the present QMC work, while the solid lines are for $t_B = t_F = 0$. Unsubscripted Roman symbols denote our phases while subscripted Roman symbols are the labeling of Lewenstein *et al.* [20].

combines our results and those of LSBF. Besides the quantitative agreement, we note the following correspondences: LSBF's region $0 \leq \bar{\mu} \leq 1$ is analogous to our $0 \leq \mu \leq 20$, and $0 \leq \alpha \leq 1$ to our $0 \leq U_{BF} \leq 20$. Furthermore, our phase II (Anti-Correlated phase) corresponds to LSBF's phase $\bar{I}I_{FL}$ (Fermi liquid of composite fermions formed by one bare fermion and bosonic hole); our phase IV (Mott insulator / Luttinger liquid) to LSBF's phase I_{FL} (Fermi liquid); and finally our phase III (Anti-Correlated phase / Relay superfluid) to LSBF's phase I_{DW} (Density wave phase). These three phases have similar qualities and occur approximately at the same locations at our and LSBF's phase diagrams.

Both calculations suggest the existence of composite particles. Our phase V (Insulator) corresponds to LSBF's phase $\bar{I}I_{FD}$, a region of fermionic domains of composite fermions formed by one bare fermion and bosonic hole. There is one case when the phases do not seem to correspond well, namely LSBF's phase $\bar{I}I_{SF}$ which is a superfluid of composite fermions formed by one bare fermion and bosonic hole. Our results (Fig. 3) instead suggest that in this region of $U_{BF} > 2U_{BB}$, the superfluid densities vanish, or are very small.

4.9 Experimental issues

Albus *et al.* [73] have given the correspondence between Hubbard model parameters U_{BB}, U_{BF}, t_B, t_F and experimentally controlled parameters. U_{BB} and U_{BF} are determined by the optical lattice depth, laser wavelength, and harmonic oscillator lengths, as well as by the scattering lengths a_{BB} and a_{BF} which can be tuned by traversing a Feshbach resonance. Similarly, the hoppings t_B and t_F follow from the lattice depth and atomic masses. It is possible to choose experimentally reasonable values of these parameters to correspond to the energy scales chosen in our paper. For example, following Albus *et al*, for a ^{87}Rb,^{40}K mixture and laser wavelength $600nm$, $a_{BB} = 100a_0$, $a_{BF} = 123.74a_0$, and $V_0 = 0.7614$ in units of boson recoil energy, with $l_B^{\perp} = 17.04nm$, we get in units of t_B: $t_B = 1$, $t_F = 2$, and $U_{BB} = U_{BF} = 10$. In this paper we have used $t_B = t_F = 1$, which would be accessible in mixtures with $m_F \approx m_B$ such as ^{40}K,^{41}K.

4.10 Conclusions

In conclusion, we have mapped out the boson density - interaction strength phase diagram of Bose-Fermi mixtures. The Mott lobe at commensurate total density has nontrivial superfluid properties, where the two components of superflow can be nonzero and anti-correlated, or both vanish. Likewise the Mott lobe at commensurate bosonic density has vanishing boson superflow and nonzero fermion stiffness. ρ_B^s is nonzero upon emerging from this lobe where the balance between boson-boson and boson-fermion repulsions opens a superfluid window, with anti-correlated superflow. The superfluidity between the two Mott regions may be of a novel type where the bosons travel along with the fermions (chosen to have relatively low density in this work). As a consequence, the superfluid onset temperature is significantly reduced. Finally, we have discussed the signatures of the above phases in the momentum distribution function of fermions and bosons, which can be measured in time of flight experiments.

We acknowledge support from the National Science Foundation Grant No. ITR-0313390, Department of Energy Grant No. DOE-BES DE-FG02-06ER46319, and useful conversations with G. G. Batrouni and T. Byrds. This work is part of the research program of the Stichting voor Fundamenteel Onderzoek der materie (FOM), which is financially supported by the Nederlandse Organisatie voor Wetenschappelijk Onderzoek (NWO).

Chapter 5

Determinant Quantum Monte Carlo for the $t - J$ Model

5.1 Introduction

In Chapter 2, I described the basic formulation of Determinant Quantum Monte Carlo. There I emphasized that the central idea was to write a path integral for the partition function by discretizing imaginary time, and then to introduce a Hubbard-Stratonovich (HS) field to eliminate the interaction terms. The fermion degrees of freedom are then traced out analytically, leaving a Monte Carlo problem in the HS field.

In this chapter we describe an attempt to apply Determinant Quantum Monte Carlo [25, 26] to the $t - J$ model. The DQMC method can not be used as is, because of the constraint which forbids double occupancy, so that the identies for the trace of a quadratic Hamiltonian given in Chapter 2 no longer apply. In our approach the Hamiltonian is modified in such a way that it is re-expressed in a form in which DQMC may be used. The main features of this approach are the introduction of a projection operator P, which destroys any doubly occupied state, and a new set of $\tilde{c}$ operators instead of the original

fermion creation and destruction operators, which prevents doubly occupied states from occurring.

The material of this chapter is rather technical, so I would like to begin with a verbal description: A constraint like forbidding double occupancy enters the partition function in two ways. First, the states in the Trace must only be over those in the restricted Hilbert space. This may be achieved by applying a projection operator P which eliminates the forbidden states. So one task in this algorithm is to develop a way to apply P. We show that P can be written and dealt with in much the same way as the U term in DQMC for the Hubbard Hamiltonian.

A second way the constraint enters is that hopping/kinetic energy should not allow forbidden intermediate states in the path integral to arise. So I also need to show how a set of modified hopping operators can be introduced to accomplish this. As in a Hubbard U term or projection operator P, HS fields are needed to treat these modified operators. The final result of our construction is an expression for the partition function which involves multiple HS fields, some for the projection operators and some for the constrained hopping. I now turn to the technical details.

5.2 Fye algorithm

5.2.1 t-J model

The $t-J$ model was described in subsection 1.3.3. The Hamiltonian is

$$\hat{H} = -t \sum_{\langle ij \rangle \sigma} (\hat{c}^{\dagger}_{i\sigma} \hat{c}_{j\sigma} + \hat{c}^{\dagger}_{j\sigma} \hat{c}_{i\sigma}) + J \sum_{ij} \vec{S}_i \cdot \vec{S}_j$$

- together with the constraint that the Hilbert space contain no doubly occupied sites.

Determinant QMC

For DQMC, we need the Hamiltonian in quadratic form in the fermion operators. Our first step is to modify the Hamiltonian so that it incorporates the constraint. This involves quartic terms which we will later need to eliminate. We write

$$H = H_1 + H_2,$$

where

$$H_1 = -t \sum_{\langle ij \rangle \sigma} (\tilde{c}^\dagger_{i,\sigma} \tilde{c}_{j,\sigma} + H.c.) \tag{5.1}$$

$$H_2 = J \sum_{\langle ij \rangle} (\vec{S}_i \cdot \vec{S}_j - \frac{1}{4} n_i n_j) \tag{5.2}$$

$$\tilde{c}_{i,\sigma} = c_{i,\sigma}(1 - n_{i,-\sigma}) \tag{5.3}$$

We introduced operators $\tilde{c}_{i,\sigma}$, $\tilde{c}^\dagger_{i,\sigma}$. The creation operator for spin σ gives a nonzero result when acting on a state only if it has spin $-\sigma$ unoccupied.

5.2.2 Infinite-U approach and Projection operator

Let P_0 be an operator which destroys a state with any doubly occupied site, and acts as an identity otherwise - i.e., it projects out the desired states. We will use an approximation P to P_0,

$$P_0 \approx P = \prod_j e^{-U_P n_{j\uparrow} n_{j\downarrow}} \tag{5.4}$$

P may be formally derived as follows:

$$P_0 = \prod_j P_{0j} = \prod_j (1 - n_{j\uparrow} n_{j\downarrow}) \tag{5.5}$$

$$P_{0j} = \lim_{x \to 1_-} (1 - x n_{j\uparrow} n_{j\downarrow}) \tag{5.6}$$

Solving this equation

$$P_{0j} = e^Y = (1 - x n_{j\uparrow} n_{j\downarrow}) \tag{5.7}$$

with respect to Y:

$$Y = \log(1 - x n_{j\uparrow} n_{j\downarrow}) = -\sum_k \frac{1}{k} (x n_{j\uparrow} n_{j\downarrow})^k = -\sum_k \frac{1}{k} x^k n_{j\uparrow} n_{j\downarrow} = \log(1-x) n_{j\uparrow} n_{j\downarrow} \tag{5.8}$$

where we used the fact that $n_{j\sigma} = 0, 1$ so that $(n_{j\sigma})^k = n_{j\sigma}$. Noting, that $lim_{x \to 1_-} \log(1 - x) = -\infty$, and defining $\log(1 - x) = -U_P$, we have

$$(1 - x n_{j\uparrow} n_{j\downarrow}) = e^{-U_P n_{j\uparrow} n_{j\downarrow}}. \tag{5.9}$$

With U_P large, $x \approx 1$, and

$$(1 - n_{j\uparrow} n_{j\downarrow}) \approx e^{-U_P n_{j\uparrow} n_{j\downarrow}} \tag{5.10}$$

Considering first the H_1 part of the Hamiltonian, we have partition function

$$Z \approx Tr \left\{ e^{-\beta(H_1 - \mu N)} P \right\} \tag{5.11}$$

In subsection 5.3.1 we will describe how P may be decoupled using Hubbard-Stratonovich transformation so that it becomes quadratic in the fermion operators.

5.2.3 $\tilde{c}$ operator

We're continuing to work with the H_1 part (5.1) of the Hamiltonian. As usual in DQMC, we split H_1 into L time slices

$$e^{-\beta H_1} = \left[e^{-(\Delta\tau)H_1}\right]^L, \tag{5.12}$$

where $\Delta\tau = \frac{\beta}{L}$.

Using a non-Hermitian Trotter approximation [50], we can write for one time slice

$$\begin{aligned} e^{-\Delta\tau H_1} &\approx \prod_{\langle ij\rangle}\prod_{\sigma=\pm 1} e^{t\Delta\tau \tilde{c}^\dagger_{i\sigma} c_{j\sigma}} e^{t\Delta\tau \tilde{c}^\dagger_{j\sigma} c_{i\sigma}} \\ &= \prod_{\langle ij\rangle}\prod_{\sigma=\pm 1} e^{t\Delta\tau c^\dagger_{i\sigma} c_{j\sigma}(1-n_{i,-\sigma})} e^{t\Delta\tau c^\dagger_{i\sigma} c_{j\sigma}(1-n_{j,-\sigma})} \end{aligned} \tag{5.13}$$

This may be decoupled using Hubbard-Stratonovich transformation [82], applying the general formula (dropping spin indices for simplicity)

$$e^{\alpha c_1^\dagger c_2 n_3} = \frac{1}{2} e^{-\alpha_2 n_3} Tr_\sigma e^{\sigma(\alpha_4 n_3 + \alpha_3 c_1^\dagger c_2)} \tag{5.14}$$

where

α_4 - arbitrary,

$e^{\alpha_2} = \cosh(\alpha_4)$,

$\alpha_3 = \frac{\alpha}{\tanh(\alpha_4)}$.

A guess for a reasonable α_4 is to have $|\alpha_4| \approx |\alpha_3|$, so for small α, $|\alpha_4| \approx \sqrt{\alpha} = \sqrt{t\Delta\tau}$. This is, in fact, the form for the coupling of a continuous HS field to the density discussed in Chapter 2. Es we have been emphasizing, Eq. 5.14 makes the exponentials quadratic in the fermion operators so that the trace over the fermion degrees of freedom can be performed analytically. The sum over the classical variables σ must be done stochastically (i.e. by Monte Carlo).

5.2.4 Spin part of the Hamiltonian

A detailed discussion of how to handle $\vec{S}\cdot\vec{S}$ interactions in DQMC formalism is given in Appendixes A, B of Fye and Hirsch [83]. See also Sakai, Arita, Aoki [86]. We do not describe it here, because the basic idea of converting a quartic form to quadratic is similar to the preceding subsection 5.2.3.

5.3 Implementation of Fye algorithm

We start with DQMC for the Hubbard model. The code then is modified, first transforming U of the Hubbard model into U_P of a projection operator, and then introducing $\tilde{c}$ operator.

5.3.1 Projection operator

Section 5.2 showed how to deal with $e^{-\beta\hat{H}}$. Now we need to insert a projection operator in the last time slice to ensure the trace is over the reduced Hilbert space of no double occupation. We use a Hubbard-Stratonovich transformation in the same way as for U in Hubbard model:

$$e^{-U_P n_{j\uparrow} n_{j\downarrow}} = e^{-\frac{U_P}{2}(n_{j\uparrow}+n_{j\downarrow})}\frac{1}{2}\sum_{\sigma=\pm 1} e^{-\sigma\lambda(n_{j\uparrow}-n_{j\downarrow})} \tag{5.15}$$

We make separate copy of a $\hat{K}$ matrix for this time slice, and add $-\frac{U_P}{2}$ to its diagonal; the second exponential in the right hand side is included as a diagonal matrix with entries $e^{-\sigma_j\lambda}$.

5.3.2 $\tilde{c}$ operator

We have for one time slice (5.13)

$$e^{-\Delta\tau H_1} = \prod_{\langle ij\rangle}\prod_{\sigma=\pm 1} e^{t\Delta\tau c^\dagger_{i\sigma}c_{j\sigma}(1-n_{i,-\sigma})}e^{t\Delta\tau c^\dagger_{i\sigma}c_{j\sigma}(1-n_{j,-\sigma})}$$

For one pair of nearest neighbor sites and spin up:

$$\begin{aligned} & e^{t\Delta\tau c_{i\uparrow}^{\dagger}c_{j\uparrow}(1-n_{i,\downarrow})}e^{t\Delta\tau c_{i\sigma}^{\dagger}c_{j_\uparrow}(1-n_{j,\downarrow})} \\ &= e^{t\Delta\tau c_{i\uparrow}^{\dagger}c_{j\uparrow}}e^{-\alpha_2 n_{i\downarrow}}\frac{1}{2}\sum_{\sigma_{1\uparrow}}e^{\sigma_{1\uparrow}(\alpha_4 n_{i\downarrow}+\alpha_3 c_{i\uparrow}^{\dagger}c_{j\uparrow})}e^{t\Delta\tau c_{j\uparrow}^{\dagger}c_{i\uparrow}}e^{-\alpha_2 n_{j\downarrow}}\frac{1}{2}\sum_{\sigma_{2\uparrow}}e^{\sigma_{2\uparrow}(\alpha_4 n_{j\downarrow}+\alpha_3 c_{j\uparrow}^{\dagger}c_{i\uparrow})} \end{aligned} \tag{5.16}$$

For the same pair of nearest neighbor sites and spin down:

$$\begin{aligned} & e^{t\Delta\tau c_{i\downarrow}^{\dagger}c_{j\downarrow}(1-n_{i,\uparrow})}e^{t\Delta\tau c_{i\sigma}^{\dagger}c_{j_\downarrow}(1-n_{j,\uparrow})} \\ &= e^{t\Delta\tau c_{i\downarrow}^{\dagger}c_{j\downarrow}}e^{-\alpha_2 n_{i\uparrow}}\frac{1}{2}\sum_{\sigma_{1\downarrow}}e^{\sigma_{1\downarrow}(\alpha_4 n_{i\uparrow}+\alpha_3 c_{i\downarrow}^{\dagger}c_{j\downarrow})}e^{t\Delta\tau c_{j\downarrow}^{\dagger}c_{i\downarrow}}e^{-\alpha_2 n_{j\uparrow}}\frac{1}{2}\sum_{\sigma_{2\downarrow}}e^{\sigma_{2\downarrow}(\alpha_4 n_{j\uparrow}+\alpha_3 c_{j\downarrow}^{\dagger}c_{i\downarrow})} \end{aligned} \tag{5.17}$$

Which may be written as a product of 2×2 matrices, which will be used to construct $M_\uparrow$ and $M_\downarrow$. For $M_\uparrow$:

$$\begin{aligned} \exp(V_\uparrow(i,j)) = & \begin{pmatrix} 1 & -t\Delta\tau \\ 0 & 1 \end{pmatrix}\begin{pmatrix} e^{-\alpha_2} & 0 \\ 0 & 1 \end{pmatrix}\begin{pmatrix} e^{\sigma_{1\downarrow}\alpha_4} & 0 \\ 0 & 1 \end{pmatrix}\begin{pmatrix} 1 & \sigma_{1\uparrow}\alpha_3 \\ 0 & 1 \end{pmatrix} \\ & \times\begin{pmatrix} 1 & 0 \\ -t\Delta\tau & 1 \end{pmatrix}\begin{pmatrix} 1 & 0 \\ 0 & e^{-\alpha_2} \end{pmatrix}\begin{pmatrix} 1 & 0 \\ 0 & e^{\sigma_{2\downarrow}\alpha_4} \end{pmatrix}\begin{pmatrix} 1 & 0 \\ \sigma_{2\uparrow}\alpha_3 & 1 \end{pmatrix} \end{aligned} \tag{5.18}$$

while for $M_\downarrow$:

$$\begin{aligned} \exp(V_\downarrow(i,j)) = & \begin{pmatrix} 1 & -t\Delta\tau \\ 0 & 1 \end{pmatrix}\begin{pmatrix} e^{-\alpha_2} & 0 \\ 0 & 1 \end{pmatrix}\begin{pmatrix} e^{\sigma_{1\uparrow}\alpha_4} & 0 \\ 0 & 1 \end{pmatrix}\begin{pmatrix} 1 & \sigma_{1\downarrow}\alpha_3 \\ 0 & 1 \end{pmatrix} \\ & \times\begin{pmatrix} 1 & 0 \\ -t\Delta\tau & 1 \end{pmatrix}\begin{pmatrix} 1 & 0 \\ 0 & e^{-\alpha_2} \end{pmatrix}\begin{pmatrix} 1 & 0 \\ 0 & e^{\sigma_{2\uparrow}\alpha_4} \end{pmatrix}\begin{pmatrix} 1 & 0 \\ \sigma_{2\downarrow}\alpha_3 & 1 \end{pmatrix}, \end{aligned} \tag{5.19}$$

where $\sigma_{1\uparrow}, \sigma_{2\uparrow}, \sigma_{1\downarrow}, \sigma_{2\downarrow}$ are Hubbard-Stratonovich fields.

The 2×2 $V_\sigma(i,j)$ matrix should be put into $\hat{V}_\sigma$ matrix:

$$\hat{V}_\sigma = \sum_{\langle ij \rangle} V'_\sigma(i,j) \tag{5.20}$$

Here $V'_\sigma(i,j)$ is $N \times N$ matrix with 2×2 matrix $V_\sigma(i,j)$ in i,j rows and columns; the remaining elements are zeroes.

The sum here is written to get an initial picture of the process. Actually we don't have $V_\sigma(i,j)$, but its exponential.

We want to divide $V_\uparrow$ so that

$$V_\uparrow = \sum_i V_{\uparrow i}, \tag{5.21}$$

where each of $V_{\uparrow i}$ is block-diagonal. For this, we divide the lattice into set of nonintersecting nearest neighbors $\langle ij \rangle$ pairs. In 1-D we need to divide the bonds into two classes

$$(-0--1--2--3-) \approx (0--1 \quad 2--3) \times (-0 \quad 1--2 \quad 3-)$$

In 2-D the bonds must be divided into 4 groups, illustrated as black, blue, red, green in the figure below.

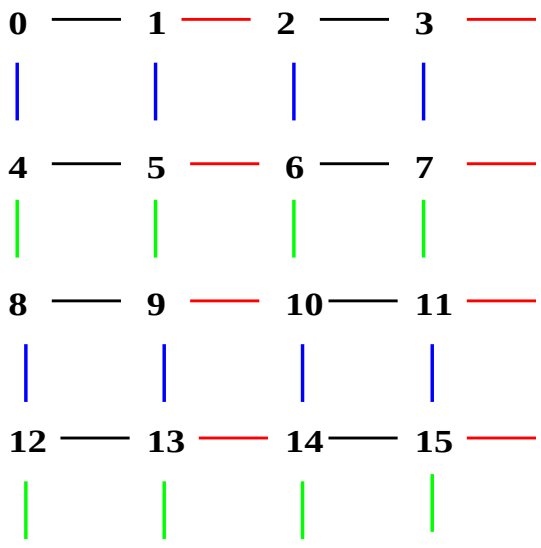

The result is a matrix product

$$e^{-V_\uparrow} = e^{-V_{\uparrow 1}} e^{-V_{\uparrow 2}} e^{-V_{\uparrow 3}} e^{-V_{\uparrow 4}} \tag{5.22}$$

where $e^{-V_{\uparrow i}}$ are block-diagonal matrices

$$e^{-V_{\uparrow 1}} = \begin{pmatrix} e^{-V_\uparrow(i_1,j_1)} & 0 & 0 & ... & 0 \\ 0 & e^{-V_\uparrow(i_2,j_2)} & 0 & ... & 0 \\ ... & ... & ... & ... & ... \\ ... & ... & ... & ... & ... \\ ... & ... & ... & ... & ... \end{pmatrix} \tag{5.23}$$

Blocks in different $V_{\uparrow i}$ are matrices of type 5.18 in different places of matrix 5.23 (corresponding to the illustration of splitting of the lattice into nearest-neighbors pairs above). E.g. for 4-site 1-D lattice with periodic boundary conditions

$$V_{\uparrow 1}: \ (i,j) = \ (0\ 1)\ (2\ 3) \qquad e^{-V_{\uparrow 1}} = \begin{pmatrix} \bullet & \bullet & 0 & 0 \\ \bullet & \bullet & 0 & 0 \\ 0 & 0 & \bullet & \bullet \\ 0 & 0 & \bullet & \bullet \end{pmatrix}$$

$$V_{\uparrow 2}: \ (i,j) = \ (1\ 2)\ (3\ 0) \qquad e^{-V_{\uparrow 1}} = \begin{pmatrix} \bullet & 0 & 0 & \bullet \\ 0 & \bullet & \bullet & 0 \\ 0 & \bullet & \bullet & 0 \\ \bullet & 0 & 0 & \bullet \end{pmatrix}$$

For 2-D lattice, we have 4 $V_{\uparrow i}$ matrices (see figure). For 4×4 lattice:

$V_{\uparrow 1}: \ (i,j) = \ (0\ 1)\ (2\ 3)\ (4\ 5)\ (6\ 7)\ (8\ 9)\ (10\ 11)\ (12\ 13)\ (14\ 15)$

$V_{\uparrow 2}: \ (i,j) = \ (1\ 2)\ (3\ 4)\ (5\ 6)\ (7\ 8)\ (9\ 10)\ (11\ 12)\ (13\ 14)\ (15\ 0)$

$V_{\uparrow 3}: \ (i,j) = \ (0\ 4)\ (1\ 5)\ (2\ 6)\ (3\ 7)\ (8\ 12)\ (9\ 13)\ (10\ 14)\ (11\ 15)$

$V_{\uparrow 4}:\ (i,j) =\ (4\ 8)\ (5\ 9)\ (6\ 10)\ (7\ 11)\ (12\ 0)\ (13\ 1)\ (14\ 2)\ (15\ 3)$

Applying a suggestion of Richard Fye, I symmetrize the product:

$$e^{-V_\uparrow} = e^{-\frac{1}{2}V_{\uparrow 1}} e^{-\frac{1}{2}V_{\uparrow 2}} e^{-\frac{1}{2}V_{\uparrow 3}} e^{-\frac{1}{2}V_{\uparrow 4}} e^{-\frac{1}{2}V_{\uparrow 4}} e^{-\frac{1}{2}V_{\uparrow 3}} e^{-\frac{1}{2}V_{\uparrow 2}} e^{-\frac{1}{2}V_{\uparrow 1}}$$

NOTE. Possibly such division of $\hat{V}_\sigma$ is not the best choice. While it seems that we have to use "building blocks" - 2×2 matrices $\exp(V_\sigma(i,j))$ as parts of $\exp(\hat{V}_\sigma)$ matrix in corresponding (i,j) rows and columns, the dividing of matrix into parts can be done in different ways.

One possibility: Take

$$V_\sigma(i,j) \ = \ \ln(\exp(V_\sigma(i,j)))$$

and sum

$$V_\sigma \ = \sum_{\langle i,j \rangle} V'_\sigma(i,j)$$

This may make fast update impossible - since we have to take $\exp V_\sigma$ after each update, and V_σ now not being block-diagonal (though not fully filled) matrix. This may be worth trying - if it improves the sign problem.

On further consideration: it should have worked in present code with 2×1 and 2×2 lattices: the way I split sites: for 1-D it is

$V_{\uparrow 1}:\ (i,j) =\ (0\ 1)$

$V_{\uparrow 2}:\ (i,j) =\ (1\ 0)$

- which is the same block. So seems this idea doesn't work for 2×1 matrix, and probably won't work for larger matrices.

5.3.3 Spin part of the Hamiltonian

The spin part of the Hamiltonian (5.2)

$$H_2 = J \sum_{\langle ij \rangle} (\vec{S}_i \cdot \vec{S}_j - \frac{1}{4} n_i n_j)$$

is decomposed by another Hubbard-Stratonovich transformation.

Using identities

$$S_{iz} \cdot S_{jz} = \frac{1}{4}(n_{i\uparrow} - n_{i\downarrow})(n_{j\uparrow} - n_{j\downarrow}) \tag{5.24}$$

$$S_{ix} \cdot S_{jx} = \frac{1}{4}(c^\dagger_{i\uparrow} c_{i\downarrow} + c^\dagger_{i\downarrow} c_{i\uparrow})(c^\dagger_{j\uparrow} c_{j\downarrow} + c^\dagger_{j\downarrow} c_{j\uparrow}) \tag{5.25}$$

$$S_{iy} \cdot S_{jy} = -\frac{1}{4}(c^\dagger_{i\uparrow} c_{i\downarrow} - c^\dagger_{i\downarrow} c_{i\uparrow})(c^\dagger_{j\uparrow} c_{j\downarrow} - c^\dagger_{j\downarrow} c_{j\uparrow}) \tag{5.26}$$

$S_{iz}S_{jz}$ and $n_i n_j$ part

$$\begin{aligned} J\left[S_{iz} \cdot S_{jz} - \frac{1}{4} n_i n_j\right] &= \frac{1}{4} J\left[(n_{i\uparrow} - n_{i\downarrow})(n_{j\uparrow} - n_{j\downarrow}) - (n_{i\uparrow} + n_{i\downarrow})(n_{j\uparrow} + n_{j\downarrow})\right] \\ &= -\frac{1}{2} J\left[n_{i\uparrow} n_{j\downarrow} + n_{i\downarrow} n_{j\uparrow}\right] \end{aligned} \tag{5.27}$$

for which we apply the standard Hirsch-Fye transformation with negative $U = (-J)$, which results in a diagonal V-matrix, with Hubbard-Stratonovich fields.

$S_{ix}S_{jx}$ and $S_{iy}S_{jy}$ part

$$\begin{aligned} & J\left[S_{ix}\cdot S_{jx}+S_{iy}\cdot S_{jy}\right] \\ =& J\frac{1}{4}(c_{i\uparrow}^{\dagger}c_{i\downarrow}+c_{i\downarrow}^{\dagger}c_{i\uparrow})(c_{j\uparrow}^{\dagger}c_{j\downarrow}+c_{j\downarrow}^{\dagger}c_{j\uparrow})-J\frac{1}{4}(c_{i\uparrow}^{\dagger}c_{i\downarrow}-c_{i\downarrow}^{\dagger}c_{i\uparrow})(c_{j\uparrow}^{\dagger}c_{j\downarrow}-c_{j\downarrow}^{\dagger}c_{j\uparrow}) \\ =& \frac{1}{2}J(c_{i\uparrow}^{\dagger}c_{i\downarrow}c_{j\downarrow}^{\dagger}c_{j\uparrow}+c_{i\downarrow}^{\dagger}c_{i\uparrow}c_{j\uparrow}^{\dagger}c_{j\downarrow}) \end{aligned} \tag{5.28}$$

And Hubbard-Stratonovich transformations

$$\begin{aligned} e^{-\frac{1}{2}J\Delta\tau(c_{i\uparrow}^{\dagger}c_{i\downarrow}c_{j\downarrow}^{\dagger}c_{j\uparrow})} &= \sum_{\sigma_2=\pm1} e^{\lambda_1\sigma_1(c_{i\uparrow}^{\dagger}c_{j\uparrow}+c_{j\downarrow}^{\dagger}c_{i\downarrow})} \\ e^{-\frac{1}{2}J\Delta\tau(c_{i\downarrow}^{\dagger}c_{i\uparrow}c_{j\uparrow}^{\dagger}c_{j\downarrow})} &= \sum_{\sigma_2=\pm1} e^{\lambda_1\sigma_2(c_{i\downarrow}^{\dagger}c_{j\downarrow}+c_{j\uparrow}^{\dagger}c_{i\uparrow})} \end{aligned} \tag{5.29}$$

where $\lambda_1 = (J(\Delta\tau)/2)^{1/2}$.

5.4 Checks of code

It is evident that the above procedure is fairly complicated. To make sure we had no errors in the derivation or in writing the code from the equations, we will verify it works in certain limits.

5.4.1 Check of code for Hubbard model

First we check the code for the Hubbard model.

I wrote a code for exact diagonalization of Hubbard model, with option of no double occupations. Checking the exact diagonalization against DQMC of the Hubbard model for cases of $U = 0$ and $t = 0$ (Fig. 5.1), the plots match: Both the dependence of occupation n on chemical potential and double occupation on U agree.

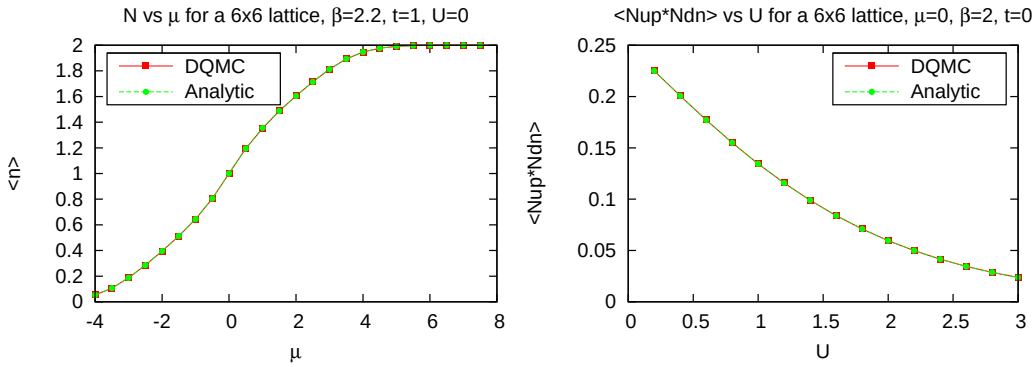

Figure 5.1: Checks of ED against DQMC for the 2-D Hubbard model.

5.4.2 Check of code for the $t-J$ model

Next we modify the Hubbard model code for the $t-J$ model. To check if projector operator works, we do simulations starting with $U_P = 0$, which should give incorrect result, and gradually increasing U_P, we must approach the correct result - the same as exact diagonalization. Figure 5.2 shows this.

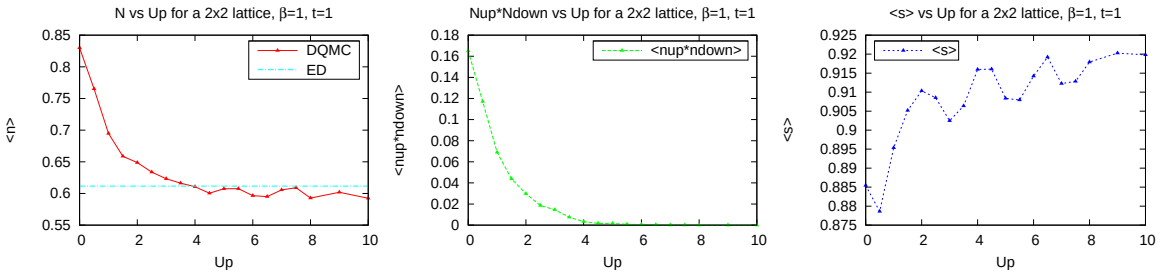

Figure 5.2: Varying strength of projection operator U_P, $\beta = 1$. Plots show dependence of occupation, double occupation and sign on strength of projection operator. As U_P increases from 0 to ≈ 4, the correspondence with ED improves.

The Fig. 5.3 shows checks of the code for 2-D 2×2 lattice.

5.4.3 Sign Problem

The central obstacle to Quantum Monte Carlo for fermions is the "sign problem." Since this is what prevented my t-J algorithm from being useful, I will give a little bit of background.

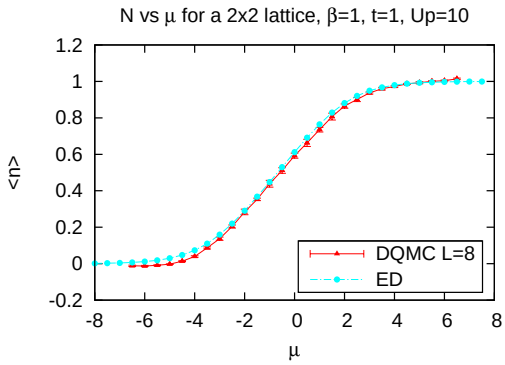

Figure 5.3: Checks of DQMC against ED for small 2×2 lattice.

In Monte Carlo we evaluate expressions like,

$$\langle A \rangle = \int dx W(x) A(x) / \int dx W(x) \ . \tag{5.30}$$

$p(x) = W(x)/\int dx W(x)$ is the probability of the configuration x and $A(x)$ is the value of the observable A in that configuration. As discussed in Chapter 2, the Metropolis algorithm provides a way to generate x with probability $p(x)$.

In writing the path integral for a quantum problem, the resulting $W(x)$ can be negative. This is the "sign problem", and it prevents implemetation of the Monte Carlo method since it involves negative probabilities to move from one state to another. The average sign

$$\langle s \rangle = \int dx W(x) / \int dx |W(x)| \ . \tag{5.31}$$

measures the severity of the sign problem. If $W(x)$ is always positive, $\langle s \rangle = 1$. Usually $\langle s \rangle$ goes to zero exponentially fast as the temperature is lowered in a quantum simulation, thereby preventing the evaluation of observables with reasonably sized error bars.

Fig. 5.4 shows dependence of the average sign $\langle s \rangle$ on β. As can be seen, $\langle s \rangle$ falls too soon with increasing of β. Possible ways to improve:

1. There are quite a few controlled parameters which affect precision and sign problem:

   $\Delta\tau$

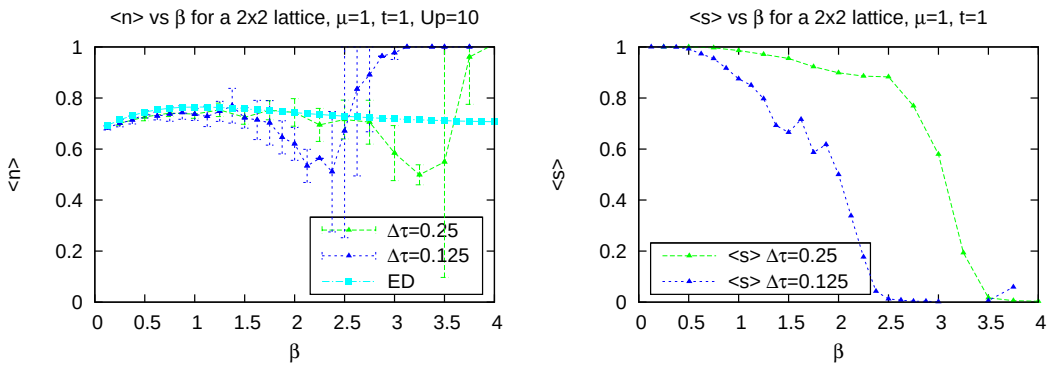

Figure 5.4: Left: Plot of $\langle n \rangle$ vs β. Right: Plot of $\langle s \rangle$ vs β.

U_P

How many projector operators to use;

α_4, which is used for decoupling of $\tilde{c}$ term (5.16, 5.17).

All need investigation.

Right now, I'm using $\Delta\tau = 0.125$, $U_P = 4$ at every time slice, $\alpha_4 = 4\sqrt{t\Delta\tau}$.

2. Check of the code for bugs.

3. Possible some methodological errors. Eg, projector operator: I put constant part $U_P/2$ into K-matrix. May be better to leave it stand-alone.

For acceptable simulations, we need $\langle s \rangle \geq 1/3$, for at least $\beta \leq 4$.

5.5 Summary

We presented work on applying Determinant Quantum Monte Carlo method to the $t-J$ model. We described the Fye algorithm for this purpose and detailed work on its implementation. The results so far were not satisfactory because of a severe sign problem.

While the results presented in the other chapters of this thesis represent published, or soon to be submitted, work, this chapter is much more preliminary. It represents an attempt to develop a new algorithm for doing Quantum Monte Carlo for Hamiltonians with constraints. I have reported results for a first code which I wrote and debugged, but, as was described, the project is far from complete. The reason is that the formulation has quite a

few variations, and I have explored only one of them (with a result that the sign problem was too bad to make the approach useable in practice). It would be interesting to test whether different Trotter discretizations, different choices of the Hubbard-Stratonovich parameters, or different placements of the projection operators might improve the sign problem enough to make the algorithm effective.

There are a number of other works on applying different Quantum Monte Carlo methods to the $t - J$ model For example, Sorella *et al* [84] study superconductivity in two-dimensional $t - J$ model using Variational Monte Carlo. White and Scalapino [85] use Green's Function Monte Carlo. There are many other works.

Chapter 6

Isentropic curves of the square lattice Hubbard model in Mean Field theory

The results described in this chapter will be submitted to Physical Review B [87].

6.1 Introduction

6.1.1 Motivation

In systems of interacting degrees of freedom, decreasing the thermal fluctuations often leads to the formation of ordered states. The traditional, and natural, measure of these fluctuations is the temperature T itself, which then forms one axis of the associated phase diagrams. However entropy S can also be used to quantify the amount of disorder. Indeed, a phase diagram using S as an axis naturally provides a somewhat different perspective on the topology of the ordered and disordered regions- since the entropy changes more rapidly where transitions occur, it magnifies these interesting portions of the phase diagram.

Recent experiments[38, 61, 14, 88] on trapped ultracold atoms in optical lattices have

provided a further motivation for employing the entropy as one of the variables in describing phase diagrams.[89, 90] In these systems, the temperature and entropy of the atomic cloud are known prior to the adiabatic ramp-up of the optical lattice, but the precise change in temperature during this process is uncertain. Thus the determination of the entropy values at which various phenomena occur, like local moment formation, magnetic ordering, and so forth, is important, supplementing the more typical discussion of the temperatures at which these phenomena occur. Furthermore, since attaining low temperatures is crucial for the emulation of many-body ordering effects seen in solid state systems, a central question is whether T rises or falls (adiabatic heating or cooling) as the optical lattice is established.

Quantum Monte Carlo (QMC) simulations have addressed some of the issues involved, but, for fermions, are limited by the sign problem as discussed in Chapter 5. In this Chapter, we present results for the isentropic curves of the square lattice fermion Hubbard model in mean field theory (MFT). The topology of these curves on the phase diagram is explored, and compared to what is found in QMC when the latter is available.

6.1.2 The Notion of Entropy

The notion of entropy was introduced into physics in the 19th century, but there is still a lot of discussion about it. One reason is the existence of several possible definitions as discussed below. The other reason is disagreement among some scientists about how basic a notion it is. For instance, Arieh Ben-Naim in his book [91] "A farewell to entropy: statistical thermodynamics based on information" advocates to abolish entropy and use information instead. Here I will begin by describing the widely different formulations for the entropy. Surprisingly, when used properly, they all converge to the same values. Let's begin with some of the alternate definitions.

Entropy as a Second Law of Thermodynamics

A thermodynamic definition of the entropy uses the idea of a (reversible) heat transfer:

$$\Delta S = \int \frac{\delta Q}{T} \tag{6.1}$$

Boltzmann-Gibbs Entropy

The entropy can also be written as a function of the total set of possible microstates of the system:

$$S = k_B \ln \Omega, \tag{6.2}$$

where Ω is number of available microstates.

Gibbs Entropy

The entropy is a function of possible microstates and their probabilities:

$$S = -k_B \sum_i p_i \ln p_i, \tag{6.3}$$

where p_i is probability of microstate i.

Von Neumann Entropy

In Quantum Mechanics, we need to go from numbers to matrices, which represent operators. The entropy is given by a modified Gibbs formula:

$$S = -k_B \mathrm{Tr}(\rho \ln \rho), \tag{6.4}$$

where ρ is the density matrix.

Shannon Entropy

The entropy in information theory is very much like the Gibbs formula:

$$H(X) = -\sum_x p_x \log_2 p_x, \tag{6.5}$$

where p_x is probability of microstate x.

Entropy as a measure of order and disorder

Qualitatively speaking, entropy is a measure of disorder of a system: higher disorder corresponds to the higher entropy. For instance, and related to the current problem, if we compare a system in a paramagnetic state, with one in a magnetic (ferromagnetic or antiferromagnetic) state, we can say that the system in the paramagnetic state is disordered, while the system in magnetic state is ordered, and therefore the system in paramagnetic state has higher entropy than the system in magnetic state.

6.2 Algorithm and Realization

6.2.1 Introduction

We discussed MFT in general and its application to the Hubbard model in section 2.4. The formula for the free energy F is given in Eq. 2.77. The entropy is calculated as

$$S = -\frac{\partial F}{\partial T} = \beta \sum_{k\sigma} \frac{(E_{k\sigma} - \mu)}{1 + e^{\beta(E_k - \mu)}} + \sum_{k\sigma} \ln(1 + e^{-\beta(E_{k\sigma} - \mu)}). \tag{6.6}$$

Now we will discuss details of the realization.

6.2.2 Real space

MFT Hamiltonians for 1-D Hubbard model are tri-diagonal matrices

$$H_\uparrow = \begin{pmatrix} U(n-m_f+m_{af})-\mu & -t & 0 & ... \\ -t & U(n-m_f-m_{af})-\mu & -t & ... \\ 0 & -t & U(n-m_f+m_{af})-\mu & ... \\ 0 & 0 & -t & ... \\ ... & ... & ... & ... \end{pmatrix}$$

For 2-D it is very similar, but matrix is "5-diagonal".

6.2.3 Momentum space

The Hamiltonian is considerably simpler in k-space. The matrix is block-diagonal with blocks like

$$\begin{pmatrix} U(n+m_f)-\mu-2t(\cos(k_x)+\cos(k_y)) & Um_{af} \\ Um_{af} & U(n+m_f)-\mu+2t(\cos(k_x)+\cos(k_y)) \end{pmatrix}$$

The eigenvalues are

$$\begin{aligned} E_{k\uparrow} &= U(n-m_f)-\mu \pm \sqrt{(-2t\cos k_x - 2t\cos k_y)^2 + (Um_{af})^2} \\ E_{k\downarrow} &= U(n+m_f)-\mu \pm \sqrt{(-2t\cos k_x - 2t\cos k_y)^2 + (Um_{af})^2} \end{aligned} \tag{6.7}$$

and eigenvectors (unnormalized) correspondingly

$$\psi_{k\uparrow} = \begin{pmatrix} \frac{-2t(\cos k_x - 2t\cos k_y) \mp \sqrt{(-2t\cos k_x - 2t\cos k_y)^2 + (Um_{af})^2}}{Um_{af}} \\ 1 \end{pmatrix}$$
$$\psi_{k\downarrow} = \begin{pmatrix} \frac{-2t(\cos k_x - 2t\cos k_y) \mp \sqrt{(-2t\cos k_x - 2t\cos k_y)^2 + (Um_{af})^2}}{Um_{af}} \\ 1 \end{pmatrix} \tag{6.8}$$

The ferromagnetic order parameter m_f is easily calculated by counting.

$$m_f = \frac{1}{2N}\sum_k (f_{k\uparrow} - f_{k\downarrow}) \tag{6.9}$$

To calculate the antiferromagnetic order parameter m_{af} we Fourier Transform back into real space, and after some algebra, we get simple formula

$$m_{af} = \frac{1}{N}\sum_{\sigma=\uparrow,\downarrow}\sum_k a_{k1}a_{k2}f_k \tag{6.10}$$

where eigenfunctions

$$\psi_k = a_{k1}c_k^\dagger + a_{k2}c_{k+\pi}^\dagger, \tag{6.11}$$

and a_{k1},a_{k2} are components of normalized ψ_k in 6.8.

6.2.4 Thermodynamic limit: Integral

The formulas in the previous section are some simple analytical functions, and sums over all k_x, k_y in momentum space, which are converted into integrals. Integrals are done numerically. This part is realized partially - with numerical integration of a smooth function. It however doesn't work well for $T = 0$, where the density is a discontinuous function of k_x, k_y. In this work the method of finite momentum space of the previous subsection is

used for the calculations.

6.3 Results

6.3.1 Reproduction of Hirsch phase diagram

Hirsch in [26] gives a phase diagram in $n - U$ plane. That is, he locates the FM, AFM and N phases as a function of density and interaction strength.

At $T = 0$ in thermodynamic limit, these phases are defined by:

FM: $m_f \neq 0$, $m_{af} = 0$

AFM: $m_f = 0$, $m_{af} \neq 0$

PM: $m_f = 0$, $m_{af} = 0$

To confirm that our code works correctly, we first reproduce the Hirsch diagram. Fig. 6.1 shows both Hirsch and our plots, which reasonably match.

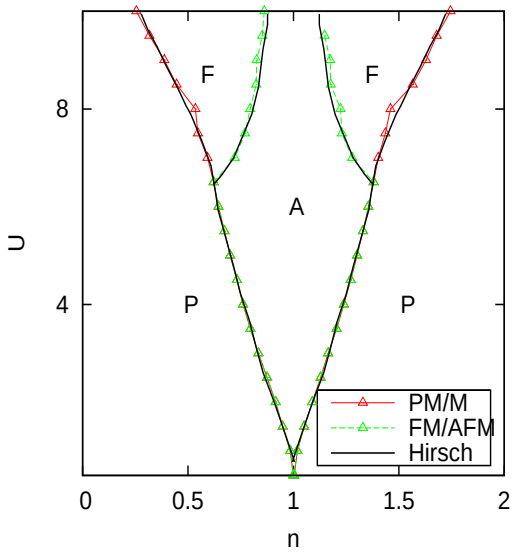

Figure 6.1: MFT phase diagram of square lattice Hubbard model at $T = 0$ showing AFM / FM / PM regions. Our result is overlaid on Hirsch's.

6.3.2 Entropy

After verifying the code, we turn now to finite temperature. The isentropic curves are the main objective of this work. In this part we present the results, discuss interesting points and compare with other models.

Fig. 6.2 shows plots of entropy S and antiferromagnetic order parameter m_{af} vs temperature at half-filling. The vanishing of AF order at T_{Neel} coincides with a kink in S(T).

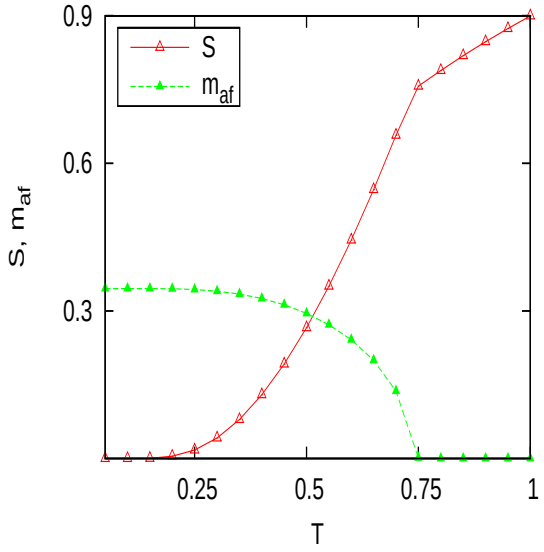

Figure 6.2: Plot of S and m_{af} vs T, n=1, U=4, 64×64 lattice. Notice that the vanishing of AF order at T_{Neel} coincides with a kink in $S(T)$.

6.3.3 Isentropic lines in $T-U$ plane at half-filling

Fig. 6.3 shows isentropic lines in the T-U plane at $n = 1$ (half-filling). This is probably the most interesting result. In the PM phase the isentropic lines are vertical, i.e. at constant temperature and density, the entropy doesn't depend on U. An argument, explaining this behavior, arises from entropy as a measure of disorder: In paramagnetic state, the system is in the same disordered state, independent of U. If we move vertically from U=0 upward, entropy remains the same until the phase boundary. Once we cross the phase boundary and enter the ordered phase, the entropy starts rising, and isentropic lines change direction. In

terms of experiment on cold atomic gases, when we turn on the optical lattice adiabatically, U/t rises, and the temperature T increases. We comment on a (well-known) weakness of MFT for the Hubbard model seen in 6.3: MFT predicts $T_N \sim U$ at large U, whereas we know instead $T_N \sim J \sim 1/U$. In fact, in 2D quantum fluctuations drive T_N to zero for all U.

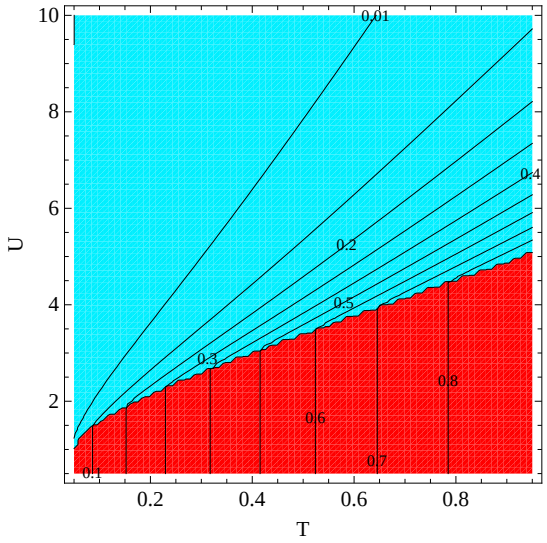

Figure 6.3: Plot of isentropic lines of the square lattice Hubbard model in T-U plane, n=1. The red region is the paramagnetic phase. The blue region is the AF phase.

6.3.4 Comparison with Quantum Monte Carlo

Paiva *et al* [92] have obtained the entropy using QMC. MFT and QMC give qualitatively similar results:

- Vertical Isentropes at small U
- Bend to right (increasing U/t) as antiferromagnetic phase entered.

The details are different:

- No finite temperature phase transition in 2D in QMC, as expected by Mermin-Wagner theorem.
- Dotted line: $\Delta_{\rm ch}$ is magnitude of charge gap (plateau in n vs. μ).

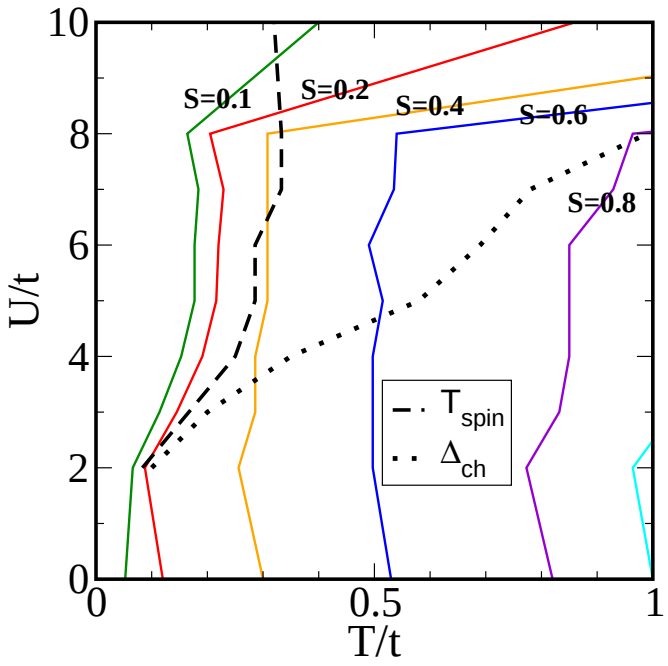

Figure 6.4: Isentropic curves obtained by QMC in T-U plane.

- Dashed line: T_{spin} temperature where robust local spin correlations develop.

The last two bullet points emphasize QMC can distinguish spin and charge energy scales, whereas MFT cannot.

6.3.5 Isentropic lines in $T-U$ plane at different fillings

We now turn to fillings different from $n = 1$. Here QMC cannot obtain results because of the sign problem. First we try filling $n = 0.8$. Note that at this filling, if we draw a line $n = 0.8$ on Hirsch diagram (Fig. 6.1), then it will go over all 3 states - PM, AFM, and FM, and will cross 2 phase boundaries - PM / AFM and AFM / FM, possibly leading to an interesting structure in the isentropes.

Fig. 6.5 shows phases and isentropic lines in plane T-U at $n = 0.8$. Somewhat surprising is the behavior of the PM / AFM phase boundary: As we increase temperature

from $T = 0$, at first U_{crit} decreases with increasing temperature. This is counterintuitive, as increasing temperature means increasing disorder, which acts against U. To counteract the effect of increasing temperature and sustain ordered AFM state, U should increase. We however observe the opposite effect, at the phase boundary U decreases when T increases from $T = 0$ to $T \approx 0.2$. However, independent calculations using the random phase approximation (RPA) agree with this surprising result. Fig. 6.6 shows plots of PM / AFM boundary both by MFT and RPA calculations, and they match. For $T > 0.2$, U_{crit} increases with T, which is conventional. We'll call the temperature at which U_{crit} is minimal, T_m. The behavior of the AFM / FM phase boundary isn't surprising. U_{crit} increases with T for all T.

We will now consider the behavior of the isentropes. In the PM phase, the isentropes behave the same way as at $n = 1$ filling - they are vertical, i.e. at constant temperature the entropy doesn't depend on U. After crossing the PM / AFM boundary, the isentropes change direction. In contrast to $n = 1$, this change of direction is not always to the right (increasing temperature). For $T < T_m$, the isentropes change direction to the left (decreasing temperature). The isentropes at the AFM / FM phase boundary are discontinuous. This indicates a first order phase transition. This is not surprising. At AFM / FM phase boundary, on both sides of the boundary, we have 2 different non-zero order parameters. That they are non-zero, would mean that thermodynamic properties are different on both sides of the boundary (except free energy, which must be the same at the boundary). This difference includes the energy, and a jump in energy means a first order transition. This is qualitatively different from PM / AFM phase boundary, where AFM order parameter must be zero at the boundary, and increasing gradually, as we go further from the border into AFM region. Fig. 6.7 illustrates the reasoning.

Next we try filling $n = 0.5$. Again drawing line $n = 0.5$ on Hirsch diagram, we conclude that at this filling, we'll cross only the PM / FM phase boundary at $T = 0$. Fig. 6.8 shows the phases and isentropic lines in plane T-U at $n = 0.5$. The behavior of PM / FM and PM

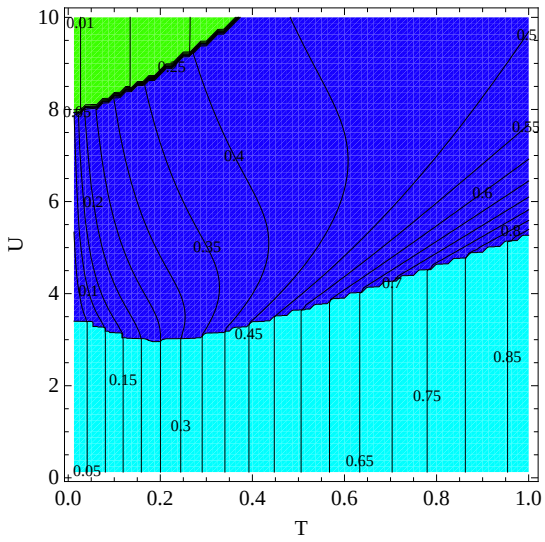

Figure 6.5: Plot of isentropic lines in T-U plane, n=0.8. The light blue (lowest) region is PM, dark blue is AFM, and green is FM.

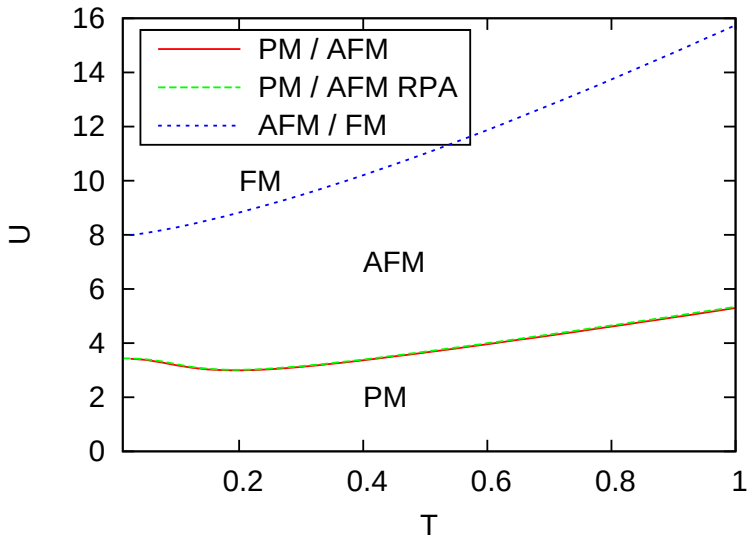

Figure 6.6: Plots of PM / AFM boundary by MFT and RPA calculations in T-U plane, n=0.8.

/ AFM phase boundary is qualitatively similar to PM / AFM phase boundary at $n = 0.8$: We have U_{crit} decreasing for $T < T_m$, and increasing for $T > T_m$. Here T_m correspond to PM / AFM boundaries.

The isentropes also behave similarly to the ones at $n = 0.8$. In the PM phase, they are

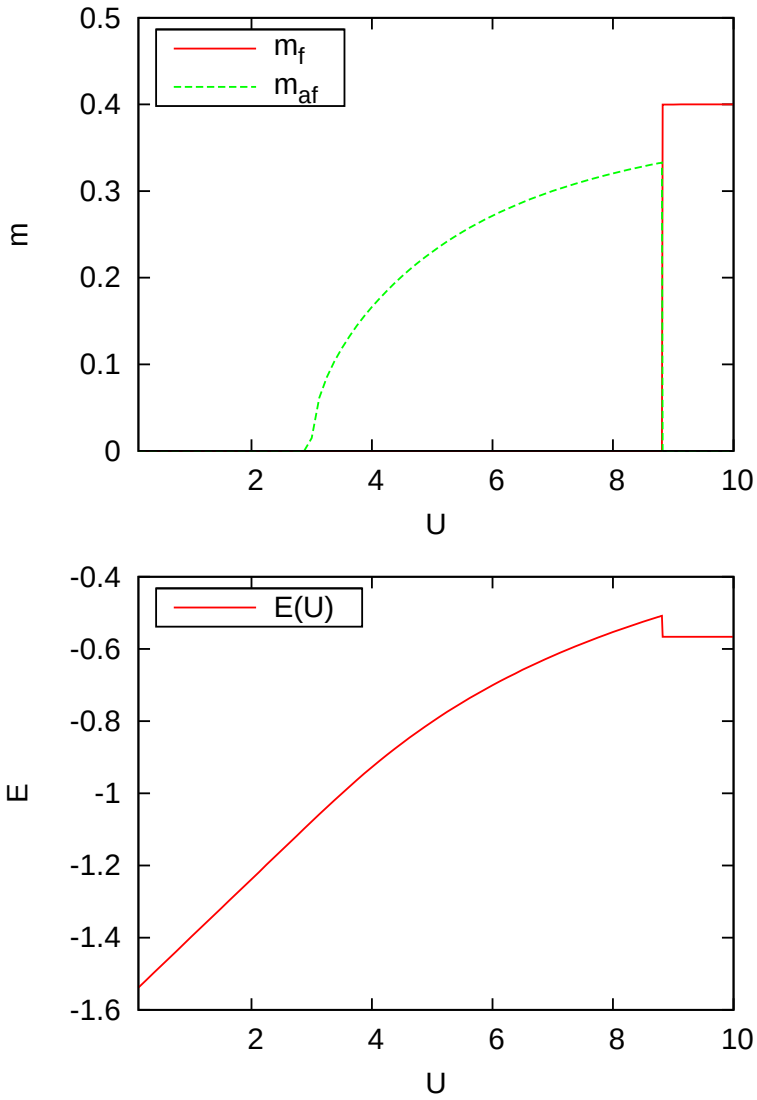

Figure 6.7: Upper panel: Plot of m_f and m_{af} at n=0.8, $T = 0.2$. Note that the change from PM to AFM phase is gradual (antiferromagnetic order parameter m_{af} grows gradually from zero), but the change from AFM to FM phase is abrupt (m_{af} jumps from finite value to zero, and m_f jumps from zero to finite value), signifying a first order transition.
Lower panel: Plot of energy E vs U. Note jump in energy at the AFM / FM boundary.

vertical, i.e. at constant temperature entropy doesn't depend on U. After crossing the PM / FM or PM / AFM boundary, the isentropes change direction: to the left for $T < T_m$, and to the right for $T > T_m$. Following the reasoning for $n = 0.8$ filling, we should have discontinuous isentropes at AFM / FM boundary, and first order phase transition. In the

figure, close to tri-critical point, it is not very clear if isentropes are discontinuous. This is because at the tri-critical point, both order parameters must be zero. Going right along the AFM / FM phase boundary, the order parameters are increasing, and the transition becomes more pronounced first order.

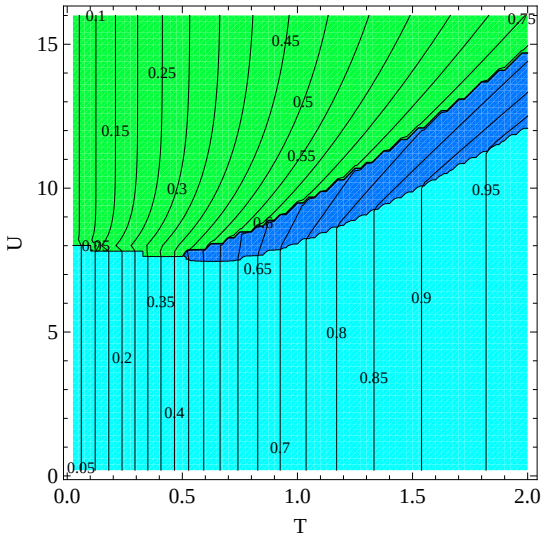

Figure 6.8: Plot of isentropic lines in T-U plane, n=0.5. The light blue (lowest) region is PM, dark blue is AFM, and green is FM.

Fig. 6.9 shows the phase diagram and isentropic lines in plane n-U at T=0.5. Basically, the phase diagram is similar to Fig. 6.1 (Hirsch phase diagram). The difference induced by higher temperature is that the ordered phases partially recede, replaced by paramagnetic phase. Finally, Fig. 6.10 shows the phase diagram in the S-U plane at n=0.5.

6.4 Summary

We presented results for the isentropic curves of the square lattice fermion Hubbard model in mean field theory (MFT). The topology of these curves on the phase diagram was explored and compared to QMC calculations. We found regions of both adiabatic heating and cooling as U/t increases for density $n = 0.8$. Our plan is to combine these MFT with calculations of isentropes for a classical model of magnetic ordering and submit a paper on the entropy and its behavior at magnetic transitions.

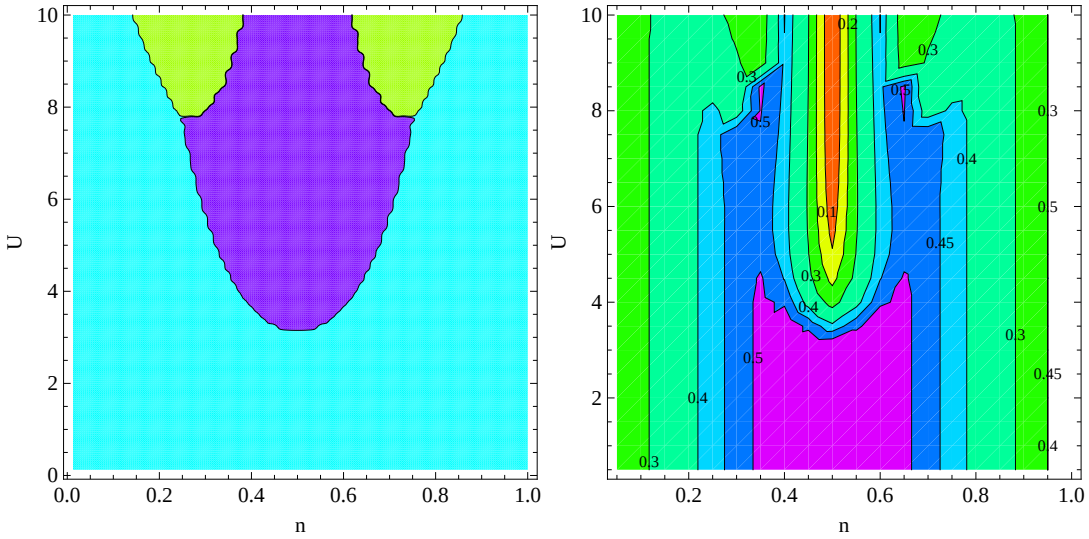

Figure 6.9: n-U plane, $T = 0.5$. Left: Phase diagram PM (blue) / AFM (magenta) / FM (green). Right: Plot of isentropic lines.

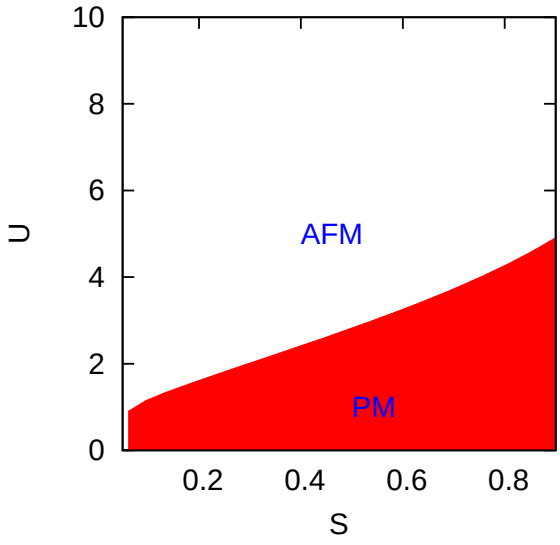

Figure 6.10: Phase diagram in S-U plane, n=1.

Chapter 7

Conclusions

In this work, a few lattice models of interacting quantum systems were explored, using various computational techniques. Now we'll summarize the results and outline possible extensions of the work.

Chapter 3 described a generalization of the Feynman and Kikuchi model of superfluidity which allows for density fluctuations. The goal was to look at the interplay of diagonal and off-diagonal long range order and the possibility of "super-solid" phases in which they coexist. A further problem of interest in the extended FK is to consider "quenched" vacancies in which the locations of the empty sites are frozen throughout the simulation. How would this affect superfluidity? Another avenue of research may be adding ring-exchange interaction.

In Chapter 4 we examined a mixture of bosons and fermions and how the insulating and superfluid behavior of the two species is affected by the interactions between them. Our focus was on explaining kinks in the visibility seen in experiments. An interesting subject is further investigation of the "super-Mott" phase of Bose-Fermi mixtures or other two(or more)-component mixtures.

Chapter 5 described the work on implementing the Hirsch-Fye algorithm for Determinant Quantum Monte Carlo to the $t - J$ model. We have encountered a serious sign problem, so the method needs further exploration.

Chapter 6 deals with computing the isentropic curves of the square lattice fermion Hubbard model in mean field theory. We have found several characteristic features of isentropic curves as they cross phase boundaries. Our motivation is that optical lattice experiments typically involve a better knowledge of the entropy than the temperature. An interesting extension of the work will be introducing disorder in the system.

Bibliography

[1] D.R. Tilley and J. Tilley, Superfluidity and Superconductivity, IOP Publishing Ltd., Bristol (1990).

[2] Antony M. Guénault, Basic superfluids, Taylor & Francis, London (2003).

[3] James F. Annett, Superconductivity, superfluids, and condensates, Oxford Univ. Press, Oxford (2005).

[4] Buckingham, M. J. and Fairbank, W. M., "The Nature of the Lambda Transition", in Progress in Low Temperature Physics III, (1961).

[5] P. Anderson, Rev. Mod. Phys. 38, 298 (1966).

[6] È Varoquaux, C. R. Physique 7 (2006) 11011120.

[7] E. L. Andronikashvili, JETP 10, 201 (1946).

[8] D.M. Ceperley and E.L. Pollock, Phys. Rev. **B39**, 2084 (1989).

[9] Han-Ching Chu and Gary A. Williams, Physica B, Volumes 284-288, Part 1, July 2000, Pages 115-116.

[10] R. Zandi, A. Shackell, J. Rudnick, M. Kardar, and L. P. Chayes, Phys. Rev. E 76, 030601 (2007).

[11] R.P. Feynman, Phys. Rev. **90**, 1116 (1953); Phys. Rev. **91**, 1291 (1953); Phys. Rev. **91**, 1301 (1953); Phys. Rev. **94**, 262 (1954).

[12] D.M. Ceperley and E.L. Pollock, Phys. Rev. **B30**, 2555 (1984); D.M. Ceperley and E.L. Pollock, Phys. Rev. Lett. **56**, 351 (1986); and E.L. Pollock and D.M. Ceperley, Phys. Rev. **B36**, 8343 (1987).

[13] C. J. Pethick and H. Smith, Bose-Einstein Condensation in Dilute Gases, Cambridge University Press (2008).

[14] I. Bloch, "Quantum gases in optical lattices", Physicsworld.com (April 10, 2004).

[15] *The Hubbard Model- Recent Results*, M. Rasetti, World Scientific, 1991.

[16] "*The Hubbard Model*," Arianna Montorsi (ed), World Scientific, 1992.

[17] *The Mott Metal-Insulator Transition, Models and Methods*, F. Gebhard, Springer 1997.

[18] P. Fazekas, Lecture Notes on Electron Correlation and Magnetism, World Scientific (1999), p. 207.

[19] A. Altland and B. Simons, Condensed Matter Field Theory, Cambridge University Press (2006), p. 58.

[20] M. Lewenstein, L. Santos, M. A. Baranov, and H. Fehrmann, Phys. Rev. Lett. **92**, 050401 (2004).

[21] O. Dutta, M. Lewenstein, arXiv:1003.0329.

[22] Jacob Linder and Asle Sudbø, Phys. Rev. A **81**, 013622 (2010).

[23] J. Spalek, t-J model then and now: A personal perspective from the pioneering times, Acta Physica Polonica A **111**, 409-24 (2007), or arXiv:0706.4236.

[24] N. Metropolis, "The Beginning of the Monte Carlo Method", Los Alamos Science, No. 15, p. 125 (1987).

[25] R. Blankenbecler, D. J. Scalapino and R. L. Sugar, Phys. Rev. D **24**, 22782286 (1981).

[26] J. E. Hirsch, Phys.Rev.B 31, 4403 (1985).

[27] Z. Bai, W. Chen, R. Scalettar, I. Yamazaki, Numerical Methods for Quantum Monte Carlo Simulations of the Hubbard Model, Technical Report CSE-2007-2007-36, Department of Computer Science, UC Davis.

[28] J.E. Hirsch, R.L. Sugar, D.J. Scalapino and R. Blankenbecler, Phys. Rev. **B26**, 5033 (1982).

[29] N. V. Prokof'ev, B. V. Svistunov, I. S. Tupitsyn, Phys. Lett. A **238**, 253 (1998); N. V. Prokof'ev, B. V. Svistunov, arXiv:0910.1393; M. Boninsengi, N. V. Prokof'ev, B. V. Svistunov, Phys. Rev. E **74**, 036701 (2006).

[30] D. M. Ceperley, Rev. Mod. Phys. **67**, 279 (1995).

[31] R. K. Pathria, Statistical Mechanics, Second edition, Elsevier (1996).

[32] A. Zujev and R. T. Scalettar, Phys. Rev. B 76, 174524 (2007).

[33] D. M. Ceperley and B. Bernu, Phys. Rev. Lett. **93**, 155303 (2004); M. Boninsegni, A. B. Kuklov, L. Pollet, N. V. Prokofev, B. V. Svistunov, and M. Troyer, Phys. Rev. Lett. **97**, 080401 (2006); Bryan K. Clark and D. M. Ceperley, Phys. Rev. Lett. **96**, 105302 (2006).

[34] E. Kim and M. H. Chan, Science **305**, 1941 (2004); E. Kim and M. H. Chan, Nature **427**, 225 (2004).

[35] J. Day, T. Herman, and J. Beamish, Phys. Rev. Lett. **95**, 035301 (2005); E. Kim and M. H. Chan, Phys. Rev. Lett. **97**, 115302 (2006); I. A. Todoshchenko, H. Alles, J. Bueno, H. J. Junes, A. Ya. Parshin, and V. Tsepelin, Phys. Rev. Lett. **97**, 165302 (2006); Ann Sophie Rittner and John D. Reppy, Phys. Rev. Lett. **97**, 165301 (2006); M. A. Adams, J. Mayers, O. Kirichek, and R. B. Down, Phys. Rev. Lett. **98**, 085301 (2007); Ann Sophie Rittner and John D. Reppy, Phys. Rev. Lett. **98**, 175302 (2007).

[36] G. Chester, Phys. Rev. **A2**, 256 (1970); A.F. Andreev, "Quantum Crystals," in *Progress in Low Temperature Physics*, Vol. VIII, D.G. Brewer (Ed.), North Holland, Amsterdam, (1982); and A.J. Leggett, Phys. Rev. Lett. **25**, 1543 (1970).

[37] M.P.A. Fisher, P.B. Weichman, G. Grinstein and D.S. Fisher, Phys. Rev. **B40**, 546 (1989).

[38] D. Jaksch, C. Bruder, J.I. Cirac, C.W. Gardiner, and P. Zoller, Phys. Rev. Lett. **81**, 3108 (1998).

[39] M. Cha, M.P.A. Fisher, S.M. Girvin, M. Wallin, and A.P. Young, Phys. Rev. **B44**, 6883 (1991); E.S. Sorensen, M. Wallin, S.M. Girvin, and A.P. Young, Phys. Rev. Lett. **69**, 828 (1992); G.G. Batrouni, B. Larson, R.T. Scalettar, J. Tobochnik, and J. Wang, Phys. Rev. **B48**, 9628 (1993); and K.J. Runge, Phys. Rev. **B45**, 13136 (1992).

[40] R. Kikuchi, Phys. Rev. **96**, 563 (1954).

[41] R. Kikuchi, H. Denman, and C.L. Schreiber, Phys. Rev. **119**, 1823 (1960).

[42] G.V. Chester, Phys. Rev. **93**, 1412 (1954).

[43] O.K. Rice, Phys. Rev. **93**, 1161 (1954).

[44] T. Matsubara, Busseiron Kenkyu **72**, 78 (1954).

[45] D. ter Haar, Phys. Rev. **95**, 895 (1954).

[46] C. Dasgupta and B.I. Halperin, Phys. Rev. Lett. **47**, 1556 (1981).

[47] As far as we know, the only Monte Carlo simulations of the Feynman Kikuchi model are contained in V. Elser, Ph.D. thesis, unpublished. These studies are in $d = 3$, and consider a local exchange restricted model.

[48] *Quantum Mechanics and Path Integrals*, R.P. Feynman and A.R. Hibbs, McGraw-Hill, New York (1965).

[49] M. Creutz and J. Freedman, Annals of Phys. **132**, 427 (1981).

[50] H.F. Trotter, Proc. Am. Math. Soc. **10**, 545 (1959).

[51] M. Suzuki, Phys. Lett. **113A**, 299 (1985).

[52] R.M. Fye, Phys. Rev. **B33**, 6271 (1986); and R.M. Fye and R.T. Scalettar, Phys. Rev. **B36**, 3833 (1987).

[53] *Monte Carlo Simulation in Statistical Physics*, K. Binder and D.W. Heermann, Springer, 1980.

[54] *Finite Size Scaling*, J. Cardy, ed. Elsevier, 1988.

[55] *Many-Particle Physics*, Gerald D. Mahan, 3rd ed., Kluwer Academic / Plenum Publishers, p. 687, 2000.

[56] G.G. Batrouni and R.T. Scalettar, Phys. Rev. Lett. **84**, 1599 (2000).

[57] F. Hébert, G.G. Batrouni, R.T. Scalettar, G. Schmid, M. Troyer and A. Dorneich, Phys. Rev. **B65** 014513 (2002).

[58] V. Rousseau, G. G. Batrouni, and R.T. Scalettar, Phys. Rev. Lett. **93**, 110404 (2004).

[59] V.G. Rousseau, R.T. Scalettar, and G.G. Batrouni, Phys. Rev. **B72**, 054524 (2005).

[60] A. Zujev, A. Baldwin, R. T. Scalettar, V. G. Rousseau, P. J. Denteneer, and M. Rigol, Phys. Rev. A 78, 033619 (2008).

[61] M. Greiner, O. Mandel, T. Esslinger, T. W. Hänsch, and I. Bloch, Nature (London) **415**, 39 (2002).

[62] H. Ott, E. de Mirandes, F. Ferlaino, G. Roati, G. Modugno, and M. Inguscio, Phys. Rev. Lett. **92**, 160601 (2004).

[63] K. Günter, T. Stöferle, H. Moritz, M. Köhl, and T. Esslinger, Phys. Rev. Lett. **96**, 180402 (2006).

[64] S. Ospelkaus, C. Ospelkaus, L. Humbert, K. Sengstock, and K. Bongs, Phys. Rev. Lett. **97**, 120403 (2006).

[65] M. Zaccanti, C. D'Errico, F. Ferlaino, G. Roati, M. Inguscio, and G. Modugno, Phys. Rev. A **74**, 041605(R) (2006).

[66] M. A. Cazalilla and A. F. Ho, Phys. Rev. Lett. **91**, 150403 (2003).

[67] L. Mathey, D.-W. Wang, W. Hofstetter, M. D. Lukin, and E. Demler, Phys. Rev. Lett. **93**, 120404 (2004); L. Mathey and D.-W. Wang, Phys. Rev. A **75**, 013612 (2007).

[68] A. Imambekov and E. Demler, Phys. Rev. A **73**, 021602(R) (2006).

[69] L. Pollet, M. Troyer, K. Van Houcke, and S. M. A. Rombouts, Phys. Rev. Lett. **96**, 190402 (2006).

[70] P. Sengupta and L. P. Pryadko, Phys. Rev. B **75**, 132507 (2007).

[71] F. Hébert, F. Haudin, L. Pollet, and G. G. Batrouni, Phys. Rev. A **76**, 043619 (2007).

[72] A. Mering and M. Fleischhauer, Phys. Rev. A **77**, 023601 (2008).

[73] A. Albus, F. Illuminati, and J. Eisert, Phys. Rev. A **68**, 023606 (2003).

[74] M. Cramer, J. Eisert, and F. Illuminati, Phys. Rev. Lett. **93**, 190405 (2004).

[75] L. Pollet, C. Kollath, U. Schollwöck, and M. Troyer, Phys. Rev. A **77**, 023608 (2008).

[76] V. G. Rousseau and P. J. H. Denteneer, Phys. Rev. A **77**, 013609 (2008).

[77] K. Van Houcke, S. M. A. Rombouts, and L. Pollet, Phys. Rev. E **73**, 056703 (2006).

[78] S. M. A. Rombouts, K. Van Houcke, and L. Pollet, Phys. Rev. Lett. **96**, 180603 (2006).

[79] G. G. Batrouni, R. T. Scalettar, and G. T. Zimanyi, Phys. Rev. Lett. **65**, 1765 (1990).

[80] N. V. Prokof'ev, B. V. Svistunov, and I. S. Tupitsyn, JETP **87**, 310 (1998).

[81] Unlike $n_B(k) = \langle\psi_0|b^\dagger(k)b(k)|\psi_0\rangle$, which is the length of a vector and hence must be positive, there is no such constraint on $n_a(k)$, which is the Fourier transform of $G^a_{ij} = \langle b^\dagger_i b_j f^\dagger_j f_i \rangle$. We have verified that the same small negative values of $n_a(k)$ in the figures are also obtained in exact diagonalization on small clusters.

[82] R. L. Stratonovich, Soviet Physics Doklady 2, 416 (1958); J. Hubbard, J. (1959) Phys. Rev. Lett. 3, 77 (1959).

[83] R. M. Fye, J. E. Hirsch, Phys. Rev. B **40**, 4780 (1989).

[84] S. Sorella, G. B. Martins, F. Becca, C. Gazza, L. Capriotti, A. Parola, and E. Dagotto, Phys. Rev. Lett. **88**, 117002 (2002).

[85] Steven R. White, D. J. Scalapino, Phys. Rev. B **61**, 6320 (2000)

[86] S. Sakai, R. Arita, H. Aoki, Phys. Rev. B **70**, 172504 (2004).

[87] D. A. Cone, A. Zujev and R. T. Scalettar, Phys. Rev. B (forthcoming).

[88] M. Lewenstein, A. Sanpera, V. Ahufinger, B. Damski, A. Sen, and U. Sen, Advances in Physics **56**, 243 (2007).

[89] See, for example, P. B. Blakie and J. V. Porto Phys. Rev. **A69**, 013603 (2004); and E. Sørensen, Ehud Altman, Michael Gullans, J. V. Porto, Mikhail D. Lukin, and Eugene Demler Phys. Rev. **A81**, 061603 (2010).

[90] R. Jördens, L. Tarruell, D. Greif, T. Uehlinger, N. Strohmaier, H. Moritz, T. Esslinger, L. De Leo, C. Kollath, A. Georges, V. Scarola, L. Pollet, E. Burovski, E. Kozik, and M. Troyer Phys. Rev. Lett. 104, 180401 (2010).

[91] A. Ben-Naim, Arieh, A farewell to entropy: statistical thermodynamics based on information : S=logW, Hackensack, N.J., World Scientific (2008).

[92] T. Paiva, R. Scalettar, M. Randeria, and N. Trivedi, Phys. Rev. Lett. **104**, 066406 (2010).